Beam model of Doppler backscattering: theory and experiment

Valerian Hongjie Hall-Chen

Merton College

University of Oxford

A thesis submitted for the degree of

Doctor of Philosophy in Theoretical Physics

Trinity 2021

For Singapore, for humankind.

Beam model of Doppler backscattering: theory and experiment

Valerian Hongjie Hall-Chen

Merton College, University of Oxford

Submitted for the degree of Doctor of Philosophy in Theoretical Physics

Trinity 2021

We use beam tracing — implemented with a newly-written code, Scotty — in combination with the reciprocity theorem to derive a model for the linear backscattered power of the Doppler Backscattering (DBS) diagnostic. Our model works for both the O-mode and X-mode in tokamak geometry (and certain regimes of stellarators). We present the analytical derivation of our model and its implications on the DBS signal localisation and the wavenumber resolution. To determine these two quantities, we find that it is the curvature of the field lines and the magnetic shear that are important, rather than the curvature of the cut-off surface. We proceed to shed light on the hitherto poorly-understood quantitative effect of the mismatch angle. Armed with this knowledge, we analyse MAST DBS data for various frequency channels and at various times, demonstrating that the beam model can indeed properly account for the mismatch attenuation. Interestingly, we show that mismatch attenuation can have a significant effect on localisation, shifting it away from the cut-off. Consequently, one can use this model to correct for the attenuation due to mismatch and its effect on localisation, avoiding the need for empirical optimisation. This is especially important in spherical tokamaks, since the magnetic pitch angle is large and varies both spatially and temporally.

Acknowledgements

After being accepted to Oxford for this DPhil, I asked Alessandro Geraldini for his thoughts on Felix Parra, my then-prospective supervisor. Alessandro's email was as long as it was effusive in praise. I thought Alessandro simply had a penchant for the dramatic, but Felix has lived up to everything he raved about and more. My other academic parent, Jon Hillesheim, proved to be an intellectual powerhouse in his own right. In addition to training me well in the ways of physics, Felix and Jon have always looked out for me; I had always wanted a father and in them I found two.

As starters to the main course that was my DPhil, I am thankful to all my research supervisors over various internships: Nikolai Yakovlev, Kwaku Eason, Siying Peng, Harry Atwater, Jason Png, and Joel Yang.

I am grateful to have been taken in by the grace of A*STAR, which provided me with scholarships for both this DPhil and for my undergraduate studies. The A*STAR community has been a surrogate family to me, giving me a sense of belonging over the past decade. Non-exhaustively and in no particular order: Samantha Seah, Stacey-Ann Lee, Ong Jun Rong, Cedric Troadec, Anjan Soumyanarayanan, Tommy Tai, Kong Jian Feng, Justin Song, Lee Ching Hua, Wu Lin, Koh Wee Shing, Alfred Huan, Alexis Low, Ian Foo, Taylor Do, Yee Wearn Xin, Yang Jingyi, Aniq Ahsan, Samantha Kwok, Xie Mingrou, Claudia Lee, Tian Junfu, Lee Jia Jun, Soh Jian Rui, Jacqueline Tan, Toh Jia Ying, and Roy Ang. I would also like to thank my scholarship sureties: Liow Cheng Boon, Liow Cheng Ling, Cheng Kah Eng, and Ho Ming Yuek.

I am indebted to Steve Cowley for proselytising fusion research at the Cambridge University Physics Society and to Alex Schekochihin for introducing me to the group at Oxford.

I would like to thank my friends and fellow fusioneers from the Oxford Plasma Theory group, the Culham Centre for Fusion Energy, the TDoTP collaboration, and the wider UK and US fusion communities. It has been an honour to fight for a better tomorrow, a fusion future, alongside such stalwart scientists: Nicolas Christen, Jason Parisi, Plamen Ivanov, Javier Mauriño, Alessandro Geraldini, Justin Ball, Michael Hardman, Juan Ruiz Ruiz, Mantas Abazorius, Ollie Beeke, Yohei Kawazura, Toby Adkins, Neal Crocker, Terry Rhodes, Tony Peebles, Roddy Vann, Kevin Ronald, David Speirs, Howard Wilson, Denis St-Onge, Adnane Osmane, Rich Cooper, Michael Fox, Michael Barnes, Paul Dellar, Quinn Pratt, Stephen Storment, Alex Creely, Dave Woodward, Joe Allen, Sam Gibson, Lucy Kogan, Simon Freethy, Shi Peng, Tom Farley, Dave Ryan, Charlie Vincent, Siobhan Smith, Michail Anastopoulos, Lucy Holland, Michael Nastac, Adwiteey Mauriya, and Filomena Nave.

I am appreciative of the companionship of friends old and new over the past five years: Edwin Lock, Divya Sridhar, Jakob Jonnerby, Vyoma Shukla, Aravinth Kulanthaivelu, Laura Hankins, Liisa Veerus, Louis Lu, Tomáš Nechleba, Rachel Waterman, Ellie Powell, Seb Fagan, Chia Horng Sheng, Quan Yijun, Tsoi Kam Ting, Kaman Lok, and Nicholas Chen.

I am beholden to my aunts, Cheng Kah Kee and Cheng Kah Boey, whose unwavering support throughout my life has been instrumental in all that I have achieved. Without them, I would have long since faltered.

None of this would have happened without my partner, Alex Hall-Chen, who gently encouraged me to consider PhD opportunities in the UK. Together, we will take on this turbulent world.

Contents

Chapter 1

Introduction

'Need brooks no delay, yet late is better than never'

— J.R.R. Tolkien, *The Lord of the Rings*

Climate change is upon us, threatening the continued survival of humanity. Now, more than ever, we need to put aside our differences, stand together shoulder-to-shoulder, and hold back the tide. Fusion energy has great promise; if we were to wield it correctly, it would be an invaluable boon for our cause.

1.1 Fusion energy

Fusion energy is carbon-free, high energy density, able to provide the baseload, produces no high-level nuclear waste, and has no risk of catastrophic failure. As such, alongside fission power and other renewables, it is an important part of humankind's struggle to mitigate the ongoing climate crisis [1].

To generate energy from fusion, ions from two light elements have to get sufficiently close together. For this to happen, the fusion fuel has to be hot and dense enough for a sufficiently long period of time. There are various methods that can be used to achieve this. In this thesis, we concern ourselves with one of these methods: magnetic confinement fusion. Large magnetic fields are applied, causing the hot charged plasma particles to gyrate tightly perpendicular to field lines, but streaming quickly parallel to them. Hence, the plasma is confined perpendicular to the field lines. To achieve confinement in the parallel direction, one loops the field lines back onto themselves, ostensibly preventing the particles from escaping.

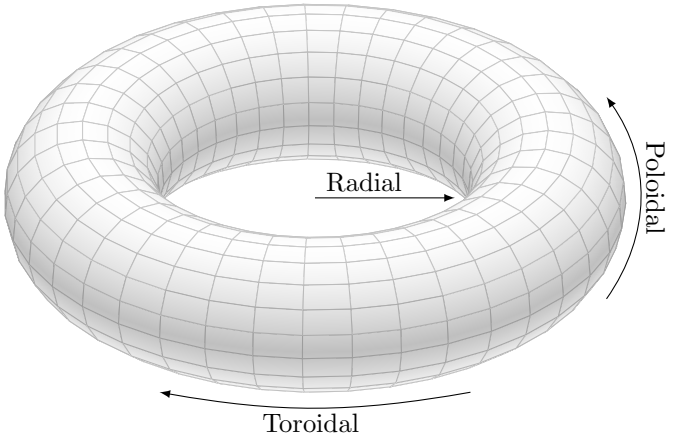

Figure 1.1: A schematic showing the radial, poloidal, and toroidal directions of a torus.

Unfortunately, there are a few subtleties with which to contend. The particles do not always exactly follow field lines. This deviation is known as drift. Drifts happen for a variety of reasons, which include curvature of the magnetic field lines, having an inhomogeneous magnetic field strength, and having an electric field that is perpendicular to the magnetic field. Most obviously, when we loop a field line back on itself, it has some finite curvature, which causes electrons and ions to drift perpendicular to the field loop, losing confinement and burning the walls of the vessel. In order to avoid this, one needs a helical magnetic field. Such a field can be generated by one of two ways: with currents or with external magnets. There are thus two main classes of magnetic-confinment machines: tokamaks and stellarators. Tokamaks are torus-shaped, and a convenient coordinate system for such devices and their plasmas is shown in Figure 1.1; their toroidal field is generated by external magnets while their poloidal field is generated by a toroidal current in the plasma. Stellarators have more complex shapes, since the entirety of the magnetic field is generated by external magnets, with no currents involved, of which we do not go into more detail in this thesis.

Unfortunately, despite our best efforts, a commercially-viable fusion power plant has yet to be actualised. One of the challenges facing fusion energy is turbulent transport [2]. Turbulence causes energy to prematurely escape the plasma. As such, it

is important to understand turbulence, and being able to measure it is crucial. Due to the high temperatures in the core, it is difficult to measure turbulence there with physical probes. Consequently, one has to resort to indirect methods such as Doppler backscattering.

1.2 Doppler backscattering diagnostic

Turbulent fluctuations in tokamaks are responsible for cross-field transport. The Doppler Backscattering (DBS) microwave diagnostic enables the non-perturbative characterisation of turbulent density fluctuations ($1 \lesssim k_\perp \rho_i \lesssim 10$) [3, 4] and flows [5–9] with high spatial and temporal resolution, both at the edge and the core of the plasma. Here, $k_\perp$ is the wavenumber of turbulent fluctuations perpendicular to the magnetic field, and ρ_i is the ion gyroradius. Consequently, it is a widely used diagnostic for both tokamaks and stellarators [10–20]. Moreover, since DBS is a microwave diagnostic, it is one of the few diagnostics that can be used in burning plasma because they are resilient to high neutron fluxes [21, 22].

The DBS works as follows. A microwave probe beam is launched into the plasma. The emitting antenna also acts as the receiver, hence only the backscattered signal is measured. In order for detectable backscattering to occur, the wavevector of the turbulent fluctuations at a particular point has to be twice in magnitude and opposite in direction to the wavevector of the probe beam at that point, see Figure 1.2. This Bragg condition determines the dominant turbulent wavenumber probed by DBS. In the linear regime, the backscattered signal's amplitude is proportional to the amplitude of the turbulence fluctuations responsible for backscattering.

Unfortunately, interpreting the backscattered signal is not entirely straightforward. There is a series of problems we seek to address: mismatch attenuation, wavenumber resolution, and localisation of the signal. We sought a model that can account for all of them in realistic geometries and realistic turbulence spectra. The model that we have developed is an extension of the already extensive work on reciprocity done by Gusakov and collaborators [23–27]. We have introduced more geometry, not assumed a particular turbulence spectrum, and used beam tracing to make the problem more

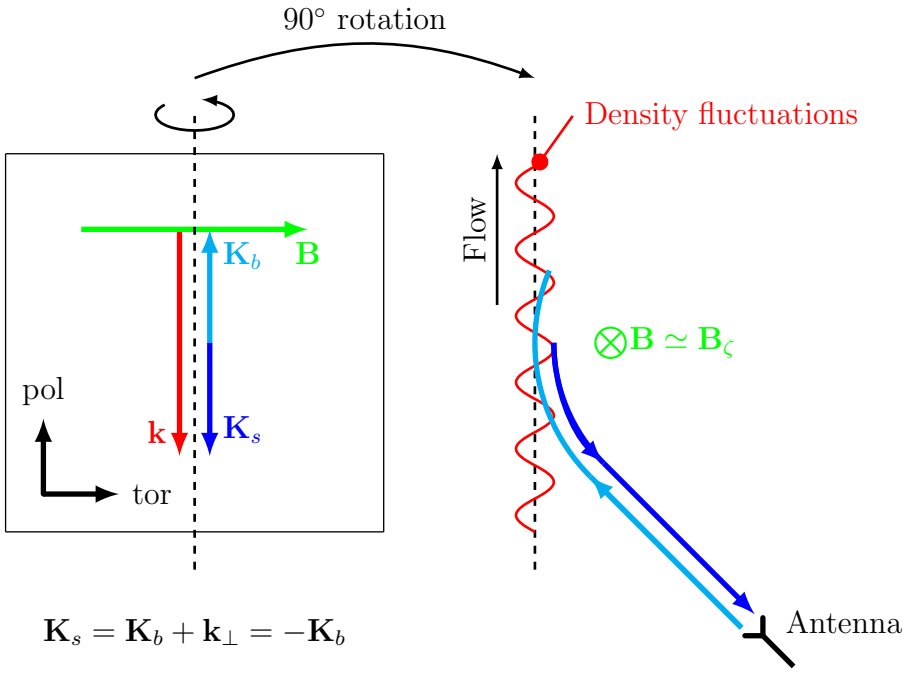

Figure 1.2: A microwave probe beam is launched into the plasma. The emitting antenna also acts as the receiver, hence only the backscattered signal is measured. In conventional tokamaks, the magnetic field is mostly in the toroidal direction. The Bragg condition determines how the wavevectors of the turbulence $\mathbf{k}$ (red), the probe beam $\mathbf{K}_b$ (light blue), and the scattered beam $\mathbf{K}_s$ (dark blue) must relate to one another for backscattering to occur. The right side of the figure represents a poloidal cut. The left side of the figure is in the plane perpendicular to the page, through the dotted line on the right side; that is, in both cases, the poloidal direction is pointing up, but on the left, the toroidal direction is in the plane of the page, while on the right, the toroidal direction is into the page. In this figure, we depict the density fluctuations at the cut-off for illustrative purposes only. Our model accounts for backscattering at every point along the ray, and we later show the extent to which different points contribute to the signal.

tractable. Since wavenumber resolution and localisation are already widely studied [3, 24, 25], we present our insight on them later in the thesis with only a brief introduction here. The rest of this section will focus on the mismatch attenuation.

As explained earlier, the dominant backscattered wavenumber is given by the Bragg condition. The extent to which other wavenumbers are also backscattered into the detector is given by the wavenumber resolution, while the contribution of various points along the ray to the backscattered signal is known as the localisation or spatial resolution.

We now introduce mismatch and the associated attenuation of the backscattered signal. The spatial scale of turbulence perpendicular to the field lines is much shorter than the characteristic length parallel to the field lines [28, 29]. Hence, one has to launch the probe beam into the plasma such that the beam reaches the scattering location perpendicular to the magnetic field, allowing the Bragg condition for backscattering to be met. When the poloidal field is much smaller than the toroidal field, as in conventional tokamaks, this is achieved by sending a beam that does not propagate toroidally.

In spherical tokamaks, the magnetic pitch angle is large (up to 35°, compared to 15° in standard tokamaks like JET) and it varies both spatially and temporally. Consequently, the DBS probe beam and the magnetic field are not normal to each other in general. This misalignment decreases the backscattered signal, making interpretation of the signal complicated (Figure 1.3): a decrease in the signal's magnitude could be due to a decrease in the fluctuations or an increase in the mismatch angle, defined to be $\sin\theta_m = \hat{\mathbf{K}} \cdot \hat{\mathbf{b}}$. Here $\hat{\mathbf{b}}$ and $\hat{\mathbf{K}}$ are the unit vectors of the external magnetic field B and the probe beam's wavevector, respectively.

The misalignment can be empirically optimised with 2D beam steering [30]. However, such empirical optimisation is ungainly and expensive, requiring several repeated shots for every measurement. Consequently, a quantitative understanding of the effect of the mismatch angle on the DBS signal would make practical the characterisation with DBS of plasmas in spherical tokamaks.

We seek to develop a quantitative understanding of what affects the backscattered signal and how. We write the electric field due to the microwaves as $\mathbf{E}\mathrm{e}^{-\mathrm{i}\Omega t}$, where Ω is the angular frequency of the microwave beam. Hence, the electric field of the probe beam (which is launched into the plasma) and the scattered microwaves satisfy

$$\frac{c^2}{\Omega^2}\nabla \times (\nabla \times \mathbf{E}) = \boldsymbol{\epsilon} \cdot \mathbf{E}. \tag{1.1}$$

Here we have already divided away the factor of $\mathrm{e}^{-\mathrm{i}\Omega t}$, and $\boldsymbol{\epsilon}$ is the cold plasma dielectric tensor, given by

$$\boldsymbol{\epsilon} = \mathbf{1} - \frac{\Omega_{pe}^2}{\Omega^2 - \Omega_{ce}^2}(\mathbf{1} - \hat{\mathbf{b}}\hat{\mathbf{b}}) - \frac{\Omega_{pe}^2}{\Omega^2}\hat{\mathbf{b}}\hat{\mathbf{b}} + \frac{\mathrm{i}\Omega_{pe}^2\Omega_{ce}}{\Omega(\Omega^2 - \Omega_{ce}^2)}(\hat{\mathbf{b}} \times \mathbf{1}), \tag{1.2}$$

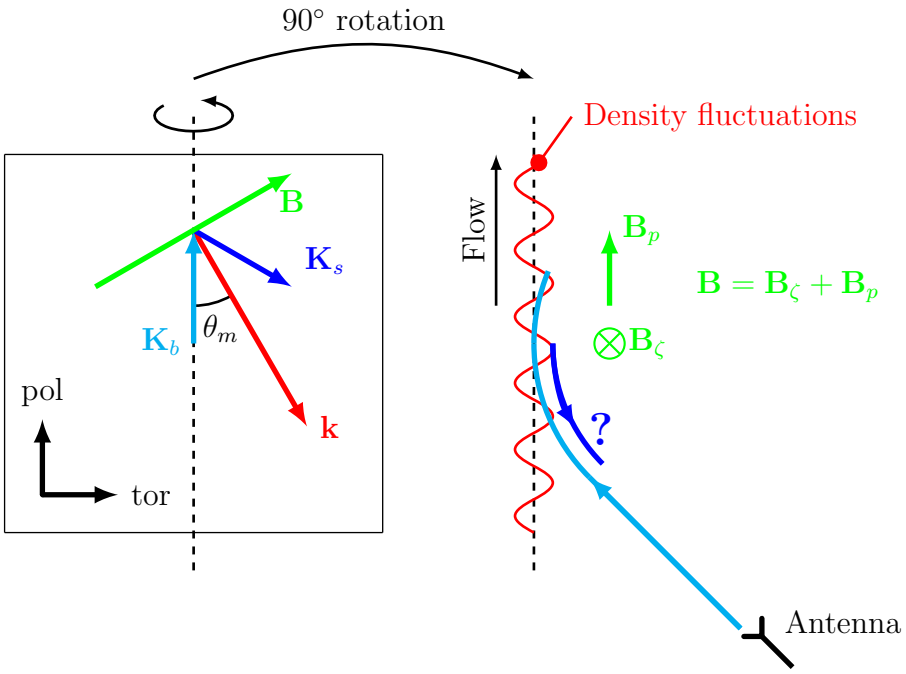

Figure 1.3: The mismatch angle reduces the backscattered signal. The variables are defined in the caption of Figure 1.2, except for the poloidal magnetic field $\mathbf{B}_p$, associated with the plasma current and the mismatch angle, which is defined to be $\sin\theta_m = \hat{\mathbf{K}} \cdot \hat{\mathbf{b}}$. Here $\hat{\mathbf{b}}$ and $\hat{\mathbf{K}}$ are the unit vectors of the magnetic field and the probe beam's wavevector respectively. Having a significant poloidal field means that a ray propagating entirely in the poloidal plane can no longer meet the Bragg condition.

where $\mathbf{1}$ is the 3×3 identity matrix, $\Omega_{pe} = (n_e e^2/m_e\epsilon_0)^{1/2}$ is the electron plasma frequency, $\Omega_{ce} = eB/m_e$ is the electron cyclotron frequency, n_e is the electron density, m_e is the electron mass, e is the absolute value of the electron charge, and ϵ_0 is the permitivity of free space. We split the dielectric tensor into equilibrium and turbulent parts, $\boldsymbol{\epsilon} = \boldsymbol{\epsilon}_{eq} + \boldsymbol{\epsilon}_{tb}$. Here we neglect the contribution of magnetic field fluctuations to $\boldsymbol{\epsilon}_{tb}$; these fluctuations are small because $\beta \ll 1$ in tokamaks and stellarators, where β is the ratio of magnetic pressure to plasma pressure. Assuming the electron density has an equilibrium piece n_e a small fluctuating part $\delta n_e \ll n_e$, we find that

$$\boldsymbol{\epsilon}_{tb} = \frac{\delta n_e}{n_e}(\boldsymbol{\epsilon}_{eq} - \mathbf{1}). \tag{1.3}$$

The inhomogeneity length associated with the equilibrium part of $\boldsymbol{\epsilon}$ is long, while the turbulence has a much shorter spatial scale. For $\delta n_e/n_e \ll 1$, we can split the electric field into a large component due to the beam and a small additive term due to the scattered microwaves, $\mathbf{E} \simeq \mathbf{E}_b + \mathbf{E}_s$. The equilibrium part of $\boldsymbol{\epsilon}$ is responsible for propagation, refraction, and diffraction of the probe beam,

$$\frac{c^2}{\Omega^2}\nabla \times (\nabla \times \mathbf{E}_b) - \boldsymbol{\epsilon}_{eq} \cdot \mathbf{E}_b = 0. \tag{1.4}$$

The scattered electric field $\mathbf{E}_s$, which is much smaller than the probe beam electric field $\mathbf{E}_b$, is associated with the fluctuating part of the dielectric constant, which has a much smaller associated spatial scale,

$$\frac{c^2}{\Omega^2}\nabla \times (\nabla \times \mathbf{E}_s) - \boldsymbol{\epsilon}_{eq} \cdot \mathbf{E}_s = \boldsymbol{\epsilon}_{tb} \cdot \mathbf{E}_b. \tag{1.5}$$

1.3 Outline

We use beam tracing in Chapter 2 to determine the electric field $\mathbf{E}_b$ due to the probe beam. We obtain an integral that determines the backscattered signal using the reciprocity theorem in Chapter 3. The main thrust of this thesis is the simplifications that we apply to this integral to obtain a manageable result, as presented in Chapters 4–5. With the form of the backscattered power, we proceed to discuss localisation in Chapter 6, wavenumber resolution in Chapter 7, and the effect of the mismatch angle in Chapter 8. We finish with a field test: meticulously comparing the model with experiment, Chapter 9.

Chapter 2

Beam tracing

To determine the electric field of the probe beam, one could perform full-wave simulations [13, 27, 31–34]. However, this method requires the turbulent dielectric tensor to high resolution, which is precisely what we do not know and are trying to determine. Compared to the size of fusion machines, the DBS wavelength is short, which requires many grid points and thus extremely computationally-intensive simulations, which is particularly challenging if one wishes to simulate backscattering from turbulence deep in the core.

A seemingly more quick and sensible approach, especially considering that there are many ray tracing codes in the fusion community [35–38], would be to trace a bundle of rays to reconstruct the microwave electric field. Unfortunately, near the cut-off, rays cross one another; these intersections are known as caustics, where the electric field is divergent. Since DBS depends on physics near the cut-off [3, 24], ray tracing is not suitable [39]. Resolving caustics is possible but involved [40–42], and its application to fusion plasmas, while promising, is still in its infancy.

One established way around the caustics problem is to trace only one ray and perform an expansion around that ray. This method, known as beam tracing, corresponds to tracing the path of a Gaussian beam, where this central ray gives the location of the peak of the Gaussian envelope. The theory of evolving Gaussian beams in isotropic inhomogeneous media is well-studied [43–45]. Beam tracing in anisotropic inhomogeneous media, which is relevant for magnetic confinement fusion, was covered briefly by Peeters [46] and more extensively by Pereverzev [47, 48] and Poli [49, 50]. Beam tracing has also been implemented numerically [51]; it has so far been used to model electron

cyclotron resonance heating (ECRH) [37], electron cyclotron current drive (ECCD) [37, 52, 53], synthetic-aperture microwave imaging (SAMI) [54], and conventional reflectometry [55, 56]. Importantly, it has been shown that the beam tracing method can be applied near the cut-off [57]; in slab geometry, the electric field from beam tracing approximates the exact solution, even in the cut-off region.

As this thesis argues, beam tracing's appeal is twofold: the sophisticated physical insight it enkindles and the nimble ease of its implementation, which swiftly gives quantitative results. Moreover, unlike in full-wave simulations, one does not need to know in advance the specific realisation of turbulent fluctuations to use beam tracing. The beam model also gives specific contributions to localisation (Chapter 6), a unique strength.

The rest of this chapter is divided into two parts. Section 2.1 lays out our beam tracing derivation, with a summary of the results in Section 2.1.5. The second part, Section 2.2, describes our new beam tracing code, Scotty.

2.1 Derivation of beam tracing

2.1.1 Ordering and ansatz

In beam tracing, we seek to find the electric field of the Gaussian probe beam as it propagates through the plasma. We do this by assuming that the length scale associated with the inhomogeneity of the density L is long compared to both the width W and wavelength λ of the beam, and that the wavelength λ is much smaller than the width of the beam W, $\lambda \ll W \ll L$. We choose the specific ordering [47, 48]

$$\frac{W}{L} \sim \frac{\lambda}{W} \ll 1. \tag{2.1}$$

Ordering the width as an intermediate length scale follows from classical optics by taking the Rayleigh length to be the same order as the inhomogeneity length. We then consider a region of space close to the trajectory of the central ray, $\mathbf{r} = \mathbf{q}(\tau)$, where τ is a parameter that gives the position along the ray. We will find the equations for $\mathbf{q}(\tau)$ as part of our beam tracing derivation.

To define a convenient coordinate system, we introduce the effective group velocity (this is not the true group velocity since it is a derivative with respect to the parameter τ, not with respect to time)

$$\mathbf{g} = g\hat{\mathbf{g}} = \frac{\mathrm{d}\mathbf{q}}{\mathrm{d}\tau}, \tag{2.2}$$

where $g = |\mathbf{g}|$ is the magnitude of $\mathbf{g}$, and $\hat{\mathbf{g}}$ its direction. The group velocity $\mathbf{g}$ is parallel to the central ray. We will describe any arbitrary position as being composed of the position along $\mathbf{q}(\tau)$ and across the ray,

$$\mathbf{r} = \mathbf{q}(\tau) + \mathbf{w} = \mathbf{q}(\tau) + w_x\hat{\mathbf{x}}(\tau) + w_y\hat{\mathbf{y}}(\tau). \tag{2.3}$$

Here $\hat{\mathbf{x}}(\tau)$ and $\hat{\mathbf{y}}(\tau)$ are two mutually perpendicular unit vectors which are also perpendicular to $\mathbf{g}$. In the orthogonal basis ($\hat{\mathbf{x}}$, $\hat{\mathbf{y}}$, $\hat{\mathbf{g}}$), the vector $\mathbf{w}$ is given by

$$\mathbf{w} = \begin{pmatrix} w_x \\ w_y \\ 0 \end{pmatrix}. \tag{2.4}$$

We write the electric field as

$$\mathbf{E}(\mathbf{r}) = \mathbf{A}(\mathbf{r}) \exp\left[\mathrm{i}\psi(\mathbf{r})\right]. \tag{2.5}$$

Using the beam tracing coordinate system, equation (2.3), we propose the following ansatz for ψ:

$$\psi(\mathbf{r}) = s(\tau) + \mathbf{K}_w(\tau) \cdot \mathbf{w} + \frac{1}{2}\mathbf{w} \cdot \boldsymbol{\Psi}_w(\tau) \cdot \mathbf{w} + \ldots, \tag{2.6}$$

where

$$s = \int_0^\tau K_g(\tau') g(\tau') \, \mathrm{d}\tau' \sim \frac{L}{\lambda}, \tag{2.7}$$

with $K_g(\tau) = \mathbf{K}(\tau) \cdot \hat{\mathbf{g}}(\tau)$ being the projection of the wavevector along the ray, while

$$\mathbf{K}_w \sim \frac{1}{\lambda}, \tag{2.8}$$

is the projection of the wavevector perpendicular to the ray. The 2D symmetric matrix $\boldsymbol{\Psi}_w(\tau)$ is complex, and

$$\boldsymbol{\Psi}_w \sim \frac{1}{W^2}. \tag{2.9}$$

The real part of $\boldsymbol{\Psi}_w$ is responsible for the curvature of the Gaussian beam, while its imaginary part gives the characteristic decay width of the Gaussian envelope. In

general, the real and imaginary parts are not simultaneously diagonalisable. The eigenvalues of the real part are

$$[\mathrm{Re}\,(\boldsymbol{\Psi}_w)]_{\alpha\alpha} = \frac{K^3}{K_g^2}\frac{1}{R_{b,\alpha}}, \tag{2.10}$$

where $R_{b,\alpha}$ are the radii of curvature of the beam front, while the eigenvalues of the imaginary part are

$$[\mathrm{Im}\,(\boldsymbol{\Psi}_w)]_{\alpha\alpha} = \frac{2}{W_\alpha^2}, \tag{2.11}$$

where W_α are the beam widths. From here on, we use the subscripts $_g$ and $_w$ to indicate projection parallel and perpendicular to the central ray respectively, and we use bold roman and bold italics to denote vectors and matrices respectively. In the basis $(\hat{\mathbf{x}}, \hat{\mathbf{y}}, \hat{\mathbf{g}})$, $\mathbf{K}_w$ and $\boldsymbol{\Psi}_w$ are

$$\mathbf{K}_w = \begin{pmatrix} K_x \\ K_y \\ 0 \end{pmatrix}, \tag{2.12}$$

and

$$\boldsymbol{\Psi}_w = \begin{pmatrix} \Psi_{xx} & \Psi_{xy} & 0 \\ \Psi_{yx} & \Psi_{yy} & 0 \\ 0 & 0 & 0 \end{pmatrix}, \tag{2.13}$$

such that $\mathbf{K}_w \cdot \hat{\mathbf{g}} = 0$ and $\boldsymbol{\Psi}_w \cdot \hat{\mathbf{g}} = 0$.

We expand the amplitude $\mathbf{A}$, given in equation (2.5), in W/L to obtain

$$\mathbf{A} = \mathbf{A}^{(0)}(\tau) + \mathbf{A}^{(1)}(\tau, \mathbf{w}) + \mathbf{A}^{(2)}(\tau, \mathbf{w}) + \ldots, \tag{2.14}$$

where $A^{(n)} \sim (W/L)^n A^{(0)}$. We take $\mathbf{A}^{(1)}$ and $\mathbf{A}^{(2)}$, the higher order amplitudes, to be linear and bilinear in $\mathbf{w}$, that is

$$\mathbf{A}^{(1)}(\tau, \mathbf{w}) = \mathbf{w} \cdot \nabla_w \mathbf{A}^{(1)}(\tau), \tag{2.15}$$

and

$$\mathbf{A}^{(2)}(\tau, \mathbf{w}) = \frac{1}{2}\mathbf{w}\mathbf{w} : \nabla_w \nabla_w \mathbf{A}^{(2)}(\tau) + \mathbf{A}^{(2)}(\tau, \mathbf{w} = 0). \tag{2.16}$$

This simplified dependence on the intermediate length scale $\mathbf{w}$ allows us to neglect $\nabla\nabla\mathbf{A}^{(1)}$ and $\nabla\nabla\nabla\mathbf{A}^{(2)}$ compared to $\nabla\nabla\mathbf{A}^{(0)}(\tau)$ and $\nabla\nabla\nabla\mathbf{A}^{(0)}(\tau)$, respectively. By

using the ansatz for the probe beam's electric field, equation (2.5), and the expansion of its amplitude in equation (2.14), we get

$$\mathbf{E} = \left[\mathbf{A}^{(0)}(\tau) + \mathbf{A}^{(1)}(\tau, \mathbf{w}) + \mathbf{A}^{(2)}(\tau, \mathbf{w})\right] \exp\left(\mathrm{i}\psi\right). \tag{2.17}$$

Since we are looking for a solution to equation (1.4), we need to evaluate the derivatives of $\mathbf{E}$,

$$\frac{\partial^2 \mathbf{E}}{\partial r_\mu \partial r_\nu} = \Bigg[\underbrace{-\frac{\partial \psi}{\partial r_\mu}\frac{\partial \psi}{\partial r_\nu}\mathbf{A}}_{\sim\lambda^{-2}\mathbf{A}} + \underbrace{\mathrm{i}\frac{\partial \psi}{\partial r_\mu}\frac{\partial \mathbf{A}}{\partial r_\nu} + \mathrm{i}\frac{\partial^2 \psi}{\partial r_\mu \partial r_\nu}\mathbf{A} + \mathrm{i}\frac{\partial \mathbf{A}}{\partial r_\mu}\frac{\partial \psi}{\partial r_\nu}}_{\sim\lambda^{-1}L^{-1}\mathbf{A}} + \underbrace{\frac{\partial^2 \mathbf{A}}{\partial r_\mu \partial r_\nu}}_{\sim L^{-2}\mathbf{A}} \Bigg] \exp(\mathrm{i}\psi). \tag{2.18}$$

The first order derivatives of ψ, where ψ is given in equation (2.6), are

$$\nabla\psi = \frac{\mathrm{d}s}{\mathrm{d}\tau}\nabla\tau + \mathbf{K}_w + \frac{\mathrm{d}\mathbf{K}_w}{\mathrm{d}\tau}\cdot\mathbf{w}\nabla\tau + \boldsymbol{\Psi}_w\cdot\mathbf{w} + \frac{1}{2}\mathbf{w}\cdot\frac{\mathrm{d}\boldsymbol{\Psi}_w}{\mathrm{d}\tau}\cdot\mathbf{w}\nabla\tau. \tag{2.19}$$

Here we have used $\mathbf{w} = [\mathbf{r} - \mathbf{q}(\tau)]_w$, and noted that since $\mathrm{d}\mathbf{q}/\mathrm{d}\tau = \mathbf{g}$, we get $\mathbf{K}_w \cdot \mathrm{d}\mathbf{q}/\mathrm{d}\tau = 0$ and $\mathrm{d}\mathbf{q}/\mathrm{d}\tau \cdot \boldsymbol{\Psi}_w \cdot \mathbf{w} = 0$. In order to proceed, we need to know the form of $\nabla\tau$. We do this by using the reciprocal vector

$$\nabla\tau = \left(\frac{\partial \mathbf{r}}{\partial w_x} \times \frac{\partial \mathbf{r}}{\partial w_y}\right)\left[\frac{\partial \mathbf{r}}{\partial \tau}\cdot\left(\frac{\partial \mathbf{r}}{\partial w_x} \times \frac{\partial \mathbf{r}}{\partial w_y}\right)\right]^{-1}. \tag{2.20}$$

Using $\mathrm{d}\hat{\mathbf{x}}/\mathrm{d}\tau \cdot \hat{\mathbf{g}} = -\hat{\mathbf{x}} \cdot \mathrm{d}\hat{\mathbf{g}}/\mathrm{d}\tau$ and $\mathrm{d}\hat{\mathbf{y}}/\mathrm{d}\tau \cdot \hat{\mathbf{g}} = -\hat{\mathbf{y}} \cdot \mathrm{d}\hat{\mathbf{g}}/\mathrm{d}\tau$, we find that

$$\nabla\tau = \hat{\mathbf{g}}\left[g - \mathbf{w}\cdot\frac{\mathrm{d}\hat{\mathbf{g}}}{\mathrm{d}\tau}\right]^{-1}. \tag{2.21}$$

Note that $g^{-1}\mathrm{d}\hat{\mathbf{g}}/\mathrm{d}\tau = \mathrm{d}\hat{\mathbf{g}}/\mathrm{d}l = \boldsymbol{\kappa}$, where $\boldsymbol{\kappa} \sim L^{-1}$ is the curvature of the central ray and l is arc length along the ray. This ray curvature should not be confused with the wavefront curvature. Using the ray curvature $\boldsymbol{\kappa}$ and equation (2.21),

$$\nabla\tau = \frac{\hat{\mathbf{g}}}{g(1 - \boldsymbol{\kappa}\cdot\mathbf{w})}. \tag{2.22}$$

We note that $\boldsymbol{\kappa}\cdot\mathbf{w} \sim W/L \ll 1$ and that we can re-express $\nabla\tau$ as

$$\nabla\tau = \frac{\hat{\mathbf{g}}}{g}[1 + \boldsymbol{\kappa}\cdot\mathbf{w} + (\boldsymbol{\kappa}\cdot\mathbf{w})^2 + \ldots]. \tag{2.23}$$

Substituting equation (2.23) into the equation for $\nabla\psi$, equation (2.19), and separating the terms by order, we get

$$\nabla\psi = \underbrace{(\nabla\psi)^{(0)}}_{\sim 1/\lambda} + \underbrace{(\nabla\psi)^{(1)}}_{\sim 1/W} + \underbrace{(\nabla\psi)^{(2)}}_{\sim 1/L} + \ldots, \tag{2.24}$$

where

$$\begin{aligned}(\nabla\psi)^{(0)} &= K_g\hat{\mathbf{g}} + \mathbf{K}_w = \mathbf{K},\\ (\nabla\psi)^{(1)} &= K_g\hat{\mathbf{g}}(\boldsymbol{\kappa}\cdot\mathbf{w}) + \frac{\hat{\mathbf{g}}}{g}\frac{\mathrm{d}\mathbf{K}_w}{\mathrm{d}\tau}\cdot\mathbf{w} + \boldsymbol{\Psi}_w\cdot\mathbf{w},\end{aligned}$$

and

$$(\nabla\psi)^{(2)} = K_g\hat{\mathbf{g}}(\boldsymbol{\kappa}\cdot\mathbf{w})^2 + \frac{\hat{\mathbf{g}}}{g}(\boldsymbol{\kappa}\cdot\mathbf{w})\frac{\mathrm{d}\mathbf{K}_w}{\mathrm{d}\tau}\cdot\mathbf{w} + \frac{1}{2}\frac{\hat{\mathbf{g}}}{g}\mathbf{w}\cdot\frac{\mathrm{d}\boldsymbol{\Psi}_w}{\mathrm{d}\tau}\cdot\mathbf{w}. \tag{2.25}$$

Here we have defined the wavenumber parallel to the central ray to be $K_g = g^{-1}\mathrm{d}s/\mathrm{d}\tau = \mathrm{d}s/\mathrm{d}l$, and the total wavevector to be $\mathbf{K} = K_g\hat{\mathbf{g}} + \mathbf{K}_w$.

We will need $\nabla\nabla\psi$ only to lowest order. Note that the gradient of ψ can only have two possible length scales, W and L. Consequently, to evaluate $\nabla\nabla\psi$ to leading order, we need to find the gradients of both $(\nabla\psi)^{(0)}$ and $(\nabla\psi)^{(1)}$, but not $(\nabla\psi)^{(2)}$. Hence, we have

$$\begin{aligned}\nabla\nabla\psi &\simeq \nabla\left[\mathbf{K} + K_g\hat{\mathbf{g}}(\boldsymbol{\kappa}\cdot\mathbf{w}) + \frac{\hat{\mathbf{g}}}{g}\frac{\mathrm{d}\mathbf{K}_w}{\mathrm{d}\tau}\cdot\mathbf{w} + \boldsymbol{\Psi}_w\cdot\mathbf{w}\right]\\ &\simeq \boldsymbol{\Psi}_w + \frac{\hat{\mathbf{g}}}{g}\frac{\mathrm{d}\mathbf{K}}{\mathrm{d}\tau} + K_g\boldsymbol{\kappa}\hat{\mathbf{g}} + \left(\frac{\mathrm{d}\mathbf{K}_w}{\mathrm{d}\tau}\right)_w\frac{\hat{\mathbf{g}}}{g},\end{aligned} \tag{2.26}$$

where all the terms are of order $(\lambda L)^{-1} \sim W^{-2}$.

We substitute equation (2.5) into equation (1.4), and remember the sizes of various terms as shown in equation (2.18). We perform a Taylor expansion of the dielectric tensor,

$$\boldsymbol{\epsilon}(\mathbf{r}) = \boldsymbol{\epsilon}(\mathbf{q}+\mathbf{w}) \simeq \boldsymbol{\epsilon}(\mathbf{q}) + \mathbf{w}\cdot\nabla\boldsymbol{\epsilon}(\mathbf{q}) + \frac{1}{2}\mathbf{w}\mathbf{w} : \nabla\nabla\boldsymbol{\epsilon}(\mathbf{q}). \tag{2.27}$$

2.1.2 Zeroth order

To lowest order $\nabla\psi \simeq K_g\hat{\mathbf{g}} + \mathbf{K}_w = \mathbf{K} \sim \lambda^{-1}$ and $\mathbf{A} \simeq \mathbf{A}^{(0)}$, giving

$$\left[\frac{c^2}{\Omega^2}(\mathbf{KK} - K^2\mathbf{1}) + \boldsymbol{\epsilon}\right] \cdot \mathbf{A}^{(0)} = 0. \tag{2.28}$$

We do not need to keep higher order terms because $(c^2/\Omega^2)\mathbf{K}\times(\mathbf{K}\times\mathbf{E}) \sim (c^2K^2/\Omega^2)E \sim N^2E$ and $\boldsymbol{\epsilon}\cdot\mathbf{E} \sim N^2E$, where N is the refractive index. For convenience, we use the notation

$$\boldsymbol{D}(\mathbf{q},\mathbf{K}) = \frac{c^2}{\Omega^2}(\mathbf{KK} - K^2\mathbf{1}) + \boldsymbol{\epsilon}(\mathbf{q}), \tag{2.29}$$

leading to

$$\boldsymbol{D}\cdot\mathbf{A}^{(0)} = 0. \tag{2.30}$$

Since $\boldsymbol{D}$ is Hermitian, it can be diagonalised — there exist three vectors $\hat{\mathbf{e}}(\mathbf{r},\mathbf{K})$ such that $\boldsymbol{D}\cdot\hat{\mathbf{e}} = H\hat{\mathbf{e}}$. To solve equation (2.29), $K_g(\tau)$ must be such that one of the three eigenvalues $H(\mathbf{q}(\tau),\mathbf{K}(\tau))$ vanishes, that is, $H = 0$ will give $K_g(\tau)$ once $\mathbf{K}_w(\tau)$ and $\mathbf{q}(\tau)$ are known. To obtain the equations for $\mathbf{K}_w(\tau)$ and $\mathbf{q}(\tau)$, we need to go to first order in the expansion $\lambda/W \sim W/L$.

In general, only one of the eigenvalues H goes to zero. The vector $\mathbf{A}^{(0)}$ has to be parallel to the $\hat{\mathbf{e}}$ that corresponds to $H = 0$, $\mathbf{A}^{(0)} = A^{(0)}\hat{\mathbf{e}}$. We split the zeroth order term into an amplitude $A^{(0)}$ and a polarisation $\hat{\mathbf{e}}$,

$$\mathbf{A}^{(0)}(\tau) = A^{(0)}(\tau)\ \hat{\mathbf{e}}\left(\mathbf{q}(\tau), K_g(\tau), \mathbf{K}_w(\tau)\right). \tag{2.31}$$

We will show that the polarisation depends on $\mathbf{q}(\tau)$, $K_g(\tau)$, $\mathbf{K}_w(\tau)$, and satisfies

$$\hat{\mathbf{e}}\cdot\hat{\mathbf{e}}^* = 1. \tag{2.32}$$

2.1.3 First order

In this subsection, we get contributions to equation (1.4) that are of first order in $\lambda/W \sim W/L \ll 1$. The terms come from $\nabla\psi$ in equation (2.19), the next order correction to the amplitude $\mathbf{A}^{(1)}$, and the expansion of $\boldsymbol{\epsilon}$ in equation (2.27),

$$(\nabla\psi)^{(1)}\cdot\nabla_K\boldsymbol{D}\cdot\hat{\mathbf{e}}A^{(0)} + \boldsymbol{D}\cdot\mathbf{A}^{(1)} + \mathbf{w}\cdot\nabla\boldsymbol{\epsilon}(\mathbf{q})\cdot\hat{\mathbf{e}}A^{(0)} = 0. \tag{2.33}$$

Here we have used

$$\frac{\partial D_{\alpha\beta}}{\partial K_\mu} = \frac{c^2}{\Omega^2}\frac{\partial}{\partial K_\mu}(K_\alpha K_\beta - K^2\delta_{\alpha\beta})$$
$$= \frac{c^2}{\Omega^2}\left[(\nabla\psi)^{(0)}_\beta\delta_{\alpha\mu} + (\nabla\psi)^{(0)}_\alpha\delta_{\beta\mu} - 2(\nabla\psi)^{(0)}_\mu\delta_{\alpha\beta}\right], \tag{2.34}$$

where $\delta_{..}$ are Kronecker deltas. Substituting the expression for $(\nabla\psi)^{(1)}$ given in equation (2.25) and realising that $\nabla\boldsymbol{\epsilon} = \nabla\boldsymbol{D}$, we get

$$\left(K_g\hat{\mathbf{g}}(\boldsymbol{\kappa}\cdot\mathbf{w}) + \frac{\hat{\mathbf{g}}}{g}\frac{d\mathbf{K}_w}{d\tau}\cdot\mathbf{w} + \boldsymbol{\Psi}_w\cdot\mathbf{w}\right)\cdot\nabla_K\boldsymbol{D}\cdot\hat{\mathbf{e}}A^{(0)}$$
$$+ \boldsymbol{D}\cdot\mathbf{A}^{(1)} + \mathbf{w}\cdot\nabla\boldsymbol{D}\cdot\hat{\mathbf{e}}A^{(0)} = 0. \tag{2.35}$$

Since $\boldsymbol{D}$ is Hermitian, $\hat{\mathbf{e}}^*\cdot\boldsymbol{D} = 0$. Thus, we multiply equation (2.35) by $\hat{\mathbf{e}}^*$ to eliminate $\boldsymbol{D}\cdot\mathbf{A}^{(1)}$,

$$\hat{\mathbf{e}}^*\cdot\left[\left(K_g\hat{\mathbf{g}}(\boldsymbol{\kappa}\cdot\mathbf{w}) + \frac{\hat{\mathbf{g}}}{g}\frac{\mathrm{d}\mathbf{K}_w}{\mathrm{d}\tau}\cdot\mathbf{w} + \boldsymbol{\Psi}_w\cdot\mathbf{w}\right)\cdot\nabla_K\boldsymbol{D} + \mathbf{w}\cdot\nabla\boldsymbol{\epsilon}(\mathbf{q})\right]\cdot\hat{\mathbf{e}} = 0. \tag{2.36}$$

This equation can be simplified by using derivatives of the dispersion relation $H = \hat{\mathbf{e}}^*\cdot\boldsymbol{D}\cdot\hat{\mathbf{e}}$. Since $\boldsymbol{D}\cdot\hat{\mathbf{e}} = 0 = \hat{\mathbf{e}}^*\cdot\boldsymbol{D}$, we find that $\partial_\mu H = \hat{\mathbf{e}}^*\cdot\partial_\mu\boldsymbol{D}\cdot\hat{\mathbf{e}}$, where ∂_μ is shorthand for either $\partial/\partial K_\mu$ or $\partial/\partial r_\mu$. Hence, equation (2.35) can be rewritten as

$$\left(K_g\hat{\mathbf{g}}(\boldsymbol{\kappa}\cdot\mathbf{w}) + \frac{\hat{\mathbf{g}}}{g}\frac{\mathrm{d}\mathbf{K}_w}{\mathrm{d}\tau}\cdot\mathbf{w} + \boldsymbol{\Psi}_w\cdot\mathbf{w}\right)\cdot\nabla_K H + \mathbf{w}\cdot\nabla H = 0. \tag{2.37}$$

We note that the curvature $\boldsymbol{\kappa}$ is always in the same plane as $\mathbf{w}$ (since it is always normal to the group velocity), and so is the matrix $\boldsymbol{\Psi}_w$ (since we have chosen it to be so). Since equation (2.36) is satisfied for all possible values of $\mathbf{w}$, we obtain

$$\left[K_g\boldsymbol{\kappa} + \frac{1}{g}\left(\frac{\mathrm{d}\mathbf{K}_w}{\mathrm{d}\tau}\right)_w\right]\hat{\mathbf{g}}\cdot\nabla_K H + \boldsymbol{\Psi}_w\cdot\nabla_K H + \nabla_w H = 0. \tag{2.38}$$

Note that H is real and $\boldsymbol{\Psi}_w$ is complex. There are four equations at play here; there are two directions associated with $(\mathrm{d}\mathbf{K}_w/\mathrm{d}\tau)_w$, and since $\boldsymbol{\Psi}_w$ is complex, both the real and imaginary parts in either of these directions must also be satisfied. Two of these equations are used to determine $\mathrm{d}\mathbf{K}_w/\mathrm{d}\tau$, and the other two are used to determine $\hat{\mathbf{g}}$, the direction of $\mathbf{g} = \mathrm{d}\mathbf{q}/\mathrm{d}\tau$. The magnitude of $\mathbf{g}$ is not determined by these equations, since we do not have enough of them; instead we choose it shortly. Since we want $\mathbf{K}$ to be real, we have to enforce $\mathrm{Im}(\boldsymbol{\Psi}_w)\cdot\nabla_K H = 0$, which will lead to $\nabla_K H \propto \hat{\mathbf{g}}$, since

$\boldsymbol{\Psi}_w$ is perpendicular to the group velocity. This is the key step — we select the group velocity such that it is in the direction of the central ray, the only direction in which there is no decay of the electric field. Since $\hat{\mathbf{g}}$ is now a unit vector in the direction of $\nabla_K H$, we get

$$\left[K_g \boldsymbol{\kappa} + \frac{1}{g}\left(\frac{\mathrm{d}\mathbf{K}_w}{\mathrm{d}\tau}\right)_w\right] |\nabla_K H| = -\nabla_w H = -\nabla H + \hat{\mathbf{g}}\hat{\mathbf{g}} \cdot \nabla H. \tag{2.39}$$

We obtain $\hat{\mathbf{g}} \cdot \nabla H$ from taking the derivative of the equation for K_g, $H = 0$, with respect to τ. Since $\mathrm{d}H/\mathrm{d}\tau = 0$, we obtain

$$\frac{\mathrm{d}\mathbf{K}}{\mathrm{d}\tau} \cdot \nabla_K H + \frac{\mathrm{d}\mathbf{q}}{\mathrm{d}\tau} \cdot \nabla H = 0, \tag{2.40}$$

which can be rewritten as

$$\frac{1}{g}\frac{\mathrm{d}\mathbf{K}}{\mathrm{d}\tau} \cdot \nabla_K H = -\hat{\mathbf{g}} \cdot \nabla H. \tag{2.41}$$

Substituting equation (2.41) into equation (2.39), we get

$$\left[K_g \boldsymbol{\kappa} + \frac{1}{g}\left(\frac{d\mathbf{K}_w}{d\tau}\right)_w\right] |\nabla_K H| + \frac{\hat{\mathbf{g}}}{g}\frac{d\mathbf{K}}{d\tau} \cdot \hat{\mathbf{g}} |\nabla_K H| = -\nabla H. \tag{2.42}$$

We then note that

$$\left(\frac{\mathrm{d}\mathbf{K}}{\mathrm{d}\tau}\right)_w = \left(\frac{\mathrm{d}\mathbf{K}_w}{\mathrm{d}\tau}\right)_w + K_g \left(\frac{\mathrm{d}\hat{\mathbf{g}}}{\mathrm{d}\tau}\right)_w = \left(\frac{\mathrm{d}\mathbf{K}_w}{\mathrm{d}\tau}\right)_w + K_g g \boldsymbol{\kappa}. \tag{2.43}$$

Consequently, we get

$$\frac{|\nabla_K H|}{g}\frac{\mathrm{d}\mathbf{K}}{\mathrm{d}\tau} = -\nabla H. \tag{2.44}$$

We then choose $g = |\nabla_K H|$. This gives us

$$\frac{\mathrm{d}\mathbf{q}}{\mathrm{d}\tau} = g\hat{\mathbf{g}} = |\nabla_K H|\hat{\mathbf{g}} = \nabla_K H. \tag{2.45}$$

Hence, we have

$$\frac{\mathrm{d}\mathbf{K}}{\mathrm{d}\tau} = -\nabla H. \tag{2.46}$$

Note that we could have chosen any other prescription for g, and it would only have modified the definition of the free parameter τ. The choice $g = |\nabla_K H|$ emphasises the Hamiltonian character of the equations.

Finally, we can use equations (2.35) and (2.39) to solve for $\mathbf{A}^{(1)}$,

$$\boldsymbol{D}\cdot\mathbf{A}^{(1)} = -\left[\left(-\frac{\hat{\mathbf{g}}\mathbf{w}\cdot\nabla H}{g} + \mathbf{w}\cdot\boldsymbol{\Psi}_w\right)\cdot\nabla_K\boldsymbol{D}\cdot\hat{\mathbf{e}} + \mathbf{w}\cdot\nabla\boldsymbol{D}\cdot\hat{\mathbf{e}}\right]A^{(0)}. \tag{2.47}$$

We can write the solution to equation (2.47) in terms of the derivatives of $\hat{\mathbf{e}}(\mathbf{r},\mathbf{K})$ Taking any derivative of $\boldsymbol{D}\cdot\hat{\mathbf{e}}=0$, we get

$$\partial_\mu\boldsymbol{D}\cdot\hat{\mathbf{e}} + \boldsymbol{D}\cdot\partial_\mu\hat{\mathbf{e}} = (\partial_\mu H)\hat{\mathbf{e}}, \tag{2.48}$$

where we have used $H=0$. The projection of equation (2.48) on $\hat{\mathbf{e}}^*$ gives

$$\partial_\mu H = \hat{\mathbf{e}}^*\cdot\partial_\mu\boldsymbol{D}\cdot\hat{\mathbf{e}}. \tag{2.49}$$

The projection perpendicular to $\hat{\mathbf{e}}^*$ gives

$$(\mathbf{1}-\hat{\mathbf{e}}\hat{\mathbf{e}}^*)\cdot\partial_\mu\boldsymbol{D}\cdot\hat{\mathbf{e}} = -\boldsymbol{D}\cdot\partial_\mu\hat{\mathbf{e}}. \tag{2.50}$$

This equation only gives the component of $\partial_\mu\hat{\mathbf{e}}$ perpendicular to $\hat{\mathbf{e}}$. The component of $\partial_\mu\hat{\mathbf{e}}$ parallel to $\hat{\mathbf{e}}$ is a free choice that is partially constrained by the condition $\hat{\mathbf{e}}\cdot\hat{\mathbf{e}}^*=1$, equation (2.32). Indeed, even with this condition, $\hat{\mathbf{e}}$ is defined only up to a phase factor α,

$$\hat{\mathbf{e}}\to\hat{\mathbf{e}}\exp(\mathrm{i}\alpha). \tag{2.51}$$

Hence, one can always add a vector parallel to $\hat{\mathbf{e}}$ to $\partial_\mu\hat{\mathbf{e}}$,

$$\partial_\mu\hat{\mathbf{e}}\to\partial_\mu\hat{\mathbf{e}} + \mathrm{i}\hat{\mathbf{e}}\partial_\mu\alpha. \tag{2.52}$$

This result shows that the condition $\hat{\mathbf{e}}\cdot\hat{\mathbf{e}}^*=1$ constrains the component of $\partial_\mu\hat{\mathbf{e}}$ along $\hat{\mathbf{e}}$ to be purely imaginary. To summarise, while $\partial_\mu\hat{\mathbf{e}}\cdot(\mathbf{1}-\hat{\mathbf{e}}^*\hat{\mathbf{e}})$ is uniquely determined by the beam tracing equations and is thus physical, $\partial_\mu\hat{\mathbf{e}}\cdot\hat{\mathbf{e}}^*\hat{\mathbf{e}}$ can be chosen at will and is not physical. Using the result in equation (2.47), and noticing that equation (2.47) is perpendicular to $\hat{\mathbf{e}}^*$ when equations (2.45) and (2.46) are satisfied, we find

$$\mathbf{A}^{(1)} = \left[\left(-\mathbf{w}\cdot\nabla_w H\frac{\hat{\mathbf{g}}}{g} + \mathbf{w}\cdot\boldsymbol{\Psi}_w\right)\cdot\nabla_K\hat{\mathbf{e}} + \mathbf{w}\cdot\nabla\hat{\mathbf{e}}\right]A^{(0)}. \tag{2.53}$$

2.1.4 Second order

To get the contributions to equation (1.4) that are second order in $\lambda/W \sim W/L \ll 1$, we need to evaluate $\nabla\mathbf{A}$,

$$\nabla\mathbf{A} \simeq \frac{d}{d\tau}(A^{(0)}\hat{\mathbf{e}})\nabla\tau + \nabla_w\mathbf{A}^{(1)}, \tag{2.54}$$

where we have noted that $\nabla_w\mathbf{A}^{(1)} \sim \nabla(A^{(0)}\hat{\mathbf{e}})$. To lowest order, $\nabla\tau \simeq \hat{\mathbf{g}}/g$. To find $\nabla_w\mathbf{A}^{(1)}$, we take the derivative of equation (2.53),

$$\nabla_w\mathbf{A}^{(1)} = \left[-\nabla_w H\frac{\hat{\mathbf{g}}}{g}\cdot\nabla_K\hat{\mathbf{e}} + \boldsymbol{\Psi}_w\cdot\nabla_K\hat{\mathbf{e}} + \nabla_w\hat{\mathbf{e}}\right]A^{(0)}. \tag{2.55}$$

It is convenient to define a new tensor $\boldsymbol{\Psi}$ that contains $\boldsymbol{\Psi}_w$. The tensor $\boldsymbol{\Psi}$ is the lowest order result for $\nabla\nabla\psi$, given in equation (2.26),

$$\boldsymbol{\Psi} = \nabla\nabla\psi. \tag{2.56}$$

With this definition of $\boldsymbol{\Psi}$, we find

$$\boldsymbol{\Psi}\cdot\nabla_K H = \frac{\mathrm{d}\mathbf{K}}{\mathrm{d}\tau} = -\nabla H, \tag{2.57}$$

$$\nabla_w\mathbf{A}^{(1)} = A^{(0)}(\boldsymbol{\Psi}\cdot\nabla_K + \nabla)_w\hat{\mathbf{e}}, \tag{2.58}$$

and

$$(\nabla\psi)^{(1)} = \boldsymbol{\Psi}\cdot\mathbf{w}. \tag{2.59}$$

Using equations (2.18), (2.24), (2.27), (2.54), and (2.56), we find the second order contribution to (1.4),

$$\begin{aligned}
&\boldsymbol{D}\cdot\mathbf{A}^{(2)} + (\nabla\psi)^{(1)}\cdot\nabla_K\boldsymbol{D}\cdot\mathbf{A}^{(1)}\\
&\quad + (\nabla\psi)^{(2)}\cdot\nabla_K\boldsymbol{D}\cdot\hat{\mathbf{e}}A^{(0)} + \frac{1}{2}(\nabla\psi)^{(1)}(\nabla\psi)^{(1)} : \nabla_K\nabla_K\boldsymbol{D}\cdot\hat{\mathbf{e}}A^{(0)}\\
&\quad + \mathbf{w}\cdot\nabla\boldsymbol{\epsilon}\cdot\mathbf{A}^{(1)} + \frac{1}{2}\mathbf{w}\mathbf{w} : \nabla\nabla\boldsymbol{\epsilon}\cdot\hat{\mathbf{e}}A^{(0)}\\
&\quad - \mathrm{i}\frac{c^2}{\Omega^2}\left[\frac{\hat{\mathbf{g}}}{g}\frac{\mathrm{d}}{\mathrm{d}\tau}\left(A^{(0)}\hat{\mathbf{e}}\right) + \nabla_w\mathbf{A}^{(1)}\right]\cdot(\nabla\psi)^{(0)}\\
&\quad + 2\mathrm{i}\frac{c^2}{\Omega^2}(\nabla\psi)^{(0)}\cdot\left[\frac{\hat{\mathbf{g}}}{g}\frac{\mathrm{d}}{\mathrm{d}\tau}\left(A^{(0)}\hat{\mathbf{e}}\right) + \nabla_w\mathbf{A}^{(1)}\right]\\
&\quad - \mathrm{i}\frac{c^2}{\Omega^2}(\nabla\psi)^{(0)}\left[\frac{\hat{\mathbf{g}}}{g}\cdot\frac{\mathrm{d}}{\mathrm{d}\tau}\left(A^{(0)}\hat{\mathbf{e}}\right) + \nabla_w\cdot\mathbf{A}^{(1)}\right]\\
&\quad - \mathrm{i}\frac{c^2}{\Omega^2}A^{(0)}\boldsymbol{\Psi}\cdot\hat{\mathbf{e}} + \mathrm{i}\frac{c^2}{\Omega^2}A^{(0)}\hat{\mathbf{e}}\boldsymbol{\Psi} : \mathbf{1} = 0.
\end{aligned} \tag{2.60}$$

To eliminate $\boldsymbol{D}\cdot\mathbf{A}^{(2)}$ from the equation, we contract the free index with $\hat{\mathbf{e}}^*$. We remark that some of the terms depend on $\mathbf{w}$ while the others do not. Since the equation must be valid regardless of the particular value of $\mathbf{w}$, we can separate it into two separate independent equations, one of which depends on $\mathbf{w}$, and the other having no $\mathbf{w}$ dependence. The equations that we derive from the piece of equation (2.60) that depends on $\mathbf{w}$ will determine the evolution of $\boldsymbol{\Psi}_w$, whereas the piece independent of $\mathbf{w}$ gives the equation for $A^{(0)}$. Note that the components of $\boldsymbol{\Psi}$ that are not in $\boldsymbol{\Psi}_w$ are determined by equation (2.57).

2.1.4.1 Pieces proportional to ww

Using equations (2.25), (2.53), (2.58), and (2.59), the terms proportional to $\mathbf{ww}$ in equation (2.60) give

$$\begin{aligned}
&\frac{1}{2g}\left[\mathbf{w}\cdot\frac{\mathrm{d}\boldsymbol{\Psi}_w}{\mathrm{d}\tau}\cdot\mathbf{w}+2gK_g(\boldsymbol{\kappa}\cdot\mathbf{w})^2+2(\boldsymbol{\kappa}\cdot\mathbf{w})\frac{\mathrm{d}\mathbf{K}_w}{\mathrm{d}\tau}\cdot\mathbf{w}\right]\left(\hat{g}_\mu\hat{\mathbf{e}}^*\cdot\frac{\partial\boldsymbol{D}}{\partial K_\mu}\cdot\hat{\mathbf{e}}\right)\\
&\quad+\mathrm{w}_\mu\Psi_{\mu\nu}\hat{\mathbf{e}}^*\cdot\frac{\partial\boldsymbol{D}}{\partial K_\nu}\cdot\left(\mathrm{w}_\alpha\Psi_{\alpha\beta}\frac{\partial\hat{\mathbf{e}}}{\partial K_\beta}+\mathrm{w}_\beta\frac{\partial\hat{\mathbf{e}}}{\partial r_\beta}\right)\\
&\quad+\frac{1}{2}(\mathrm{w}_\mu\Psi_{\mu\nu})(\mathrm{w}_\alpha\Psi_{\alpha\beta})\hat{\mathbf{e}}^*\cdot\frac{\partial^2\boldsymbol{D}}{\partial K_\nu K_\beta}\cdot\hat{\mathbf{e}}\\
&\quad+\mathrm{w}_\nu\hat{\mathbf{e}}^*\cdot\frac{\partial\boldsymbol{D}}{\partial r_\nu}\cdot\left(\mathrm{w}_\alpha\Psi_{\alpha\beta}\frac{\partial\hat{\mathbf{e}}}{\partial K_\beta}+\mathrm{w}_\beta\frac{\partial\hat{\mathbf{e}}}{\partial r_\beta}\right)\\
&\quad+\frac{1}{2}\mathrm{w}_\nu\mathrm{w}_\beta\hat{\mathbf{e}}^*\cdot\frac{\partial^2\boldsymbol{D}}{\partial r_\nu r_\beta}\cdot\hat{\mathbf{e}}=0.
\end{aligned}\tag{2.61}$$

We now use equations (2.43), (2.56), and (2.26) to write

$$\mathbf{w}\cdot\frac{\mathrm{d}\boldsymbol{\Psi}_w}{\mathrm{d}\tau}\cdot\mathbf{w}=\mathbf{w}\cdot\frac{\mathrm{d}\boldsymbol{\Psi}}{\mathrm{d}\tau}\cdot\mathbf{w}-2gK_g(\boldsymbol{\kappa}\cdot\mathbf{w})^2-2(\boldsymbol{\kappa}\cdot\mathbf{w})\frac{\mathrm{d}\mathbf{K}_w}{\mathrm{d}\tau}\cdot\mathbf{w}.\tag{2.62}$$

We then substitute equation (2.62) into equation (2.61) and use

$$\hat{g}_\mu\hat{\mathbf{e}}^*\cdot\frac{\partial\boldsymbol{D}}{\partial K_\mu}\cdot\hat{\mathbf{e}}=\hat{\mathbf{g}}\cdot\nabla_K H=g\tag{2.63}$$

to get

$$\begin{aligned}
&\mathbf{w}\cdot\frac{\mathrm{d}\boldsymbol{\Psi}}{\mathrm{d}\tau}\cdot\mathbf{w}+2\mathrm{w}_\mu\Psi_{\mu\nu}\hat{\mathbf{e}}^*\cdot\frac{\partial\boldsymbol{D}}{\partial K_\nu}\cdot\left(\mathrm{w}_\alpha\Psi_{\alpha\beta}\frac{\partial\hat{\mathbf{e}}}{\partial K_\beta}\right)\\
&+\mathrm{w}_\beta\frac{\partial\hat{\mathbf{e}}}{\partial r_\beta}+(\mathrm{w}_\mu\Psi_{\mu\nu})(\mathrm{w}_\alpha\Psi_{\alpha\beta})\hat{\mathbf{e}}^*\cdot\frac{\partial^2\boldsymbol{D}}{\partial K_\nu K_\beta}\cdot\hat{\mathbf{e}}\\
&+2\mathrm{w}_\nu\hat{\mathbf{e}}^*\cdot\frac{\partial\boldsymbol{D}}{\partial r_\nu}\cdot\left(\mathrm{w}_\alpha\Psi_{\alpha\beta}\frac{\partial\hat{\mathbf{e}}}{\partial K_\beta}+\mathrm{w}_\beta\frac{\partial\hat{\mathbf{e}}}{\partial r_\beta}\right)+\mathrm{w}_\nu\mathrm{w}_\beta\hat{\mathbf{e}}^*\cdot\frac{\partial^2\boldsymbol{D}}{\partial r_\nu\partial r_\beta}\cdot\hat{\mathbf{e}}=0.
\end{aligned}\tag{2.64}$$

This expression can be rewritten in terms of derivatives of the dispersion relation H. Differentiating $\boldsymbol{D}\cdot\hat{\mathbf{e}} = H\hat{\mathbf{e}}$, we find

$$\begin{aligned}&\partial_\mu\partial_\nu\boldsymbol{D}\cdot\hat{\mathbf{e}} + \partial_\nu\boldsymbol{D}\cdot\partial_\mu\hat{\mathbf{e}} + \partial_\mu\boldsymbol{D}\cdot\partial_\nu\hat{\mathbf{e}} + \boldsymbol{D}\cdot\partial_\mu\partial_\nu\hat{\mathbf{e}}\\ &\quad= (\partial_\mu\partial_\nu H)\hat{\mathbf{e}} + (\partial_\nu H)\partial_\mu\hat{\mathbf{e}} + (\partial_\mu H)\partial_\nu\hat{\mathbf{e}} + H\partial_\mu\partial_\nu\hat{\mathbf{e}}.\end{aligned} \tag{2.65}$$

Contracting the free index in this equation with $\hat{\mathbf{e}}^*$, we get

$$\begin{aligned}&\hat{\mathbf{e}}^*\cdot\partial_\mu\partial_\nu\boldsymbol{D}\cdot\hat{\mathbf{e}} + \hat{\mathbf{e}}^*\cdot\partial_\nu\boldsymbol{D}\cdot\partial_\mu\hat{\mathbf{e}} + \hat{\mathbf{e}}^*\cdot\partial_\mu\boldsymbol{D}\cdot\partial_\nu\hat{\mathbf{e}}\\ &\quad= \partial_\mu\partial_\nu H + (\partial_\nu H)\partial_\mu\hat{\mathbf{e}}\cdot\hat{\mathbf{e}}^* + (\partial_\mu H)\partial_\nu\hat{\mathbf{e}}\cdot\hat{\mathbf{e}}^*,\end{aligned} \tag{2.66}$$

where we have used $H = 0$ and $\hat{\mathbf{e}}^*\cdot\boldsymbol{D} = 0$. Using these results, employing the fact that the equation must hold true for arbitrary $\mathbf{w}$, and remembering that $\boldsymbol{\Psi}$ is symmetric, we find that

$$\begin{aligned}&\left(\frac{\mathrm{d}\boldsymbol{\Psi}}{\mathrm{d}\tau} + \nabla\nabla H + \boldsymbol{\Psi}\cdot\nabla_K\nabla H + \nabla\nabla_K H\cdot\boldsymbol{\Psi} + \boldsymbol{\Psi}\cdot\nabla_K\nabla_K H\cdot\boldsymbol{\Psi}\right)_w\\ &\quad+ \left[(\boldsymbol{\Psi}\cdot\nabla_K H)\,(\boldsymbol{\Psi}\cdot\nabla_K\hat{\mathbf{e}}\cdot\hat{\mathbf{e}}^*) + (\boldsymbol{\Psi}\cdot\nabla_K\hat{\mathbf{e}}\cdot\hat{\mathbf{e}}^*)\,(\boldsymbol{\Psi}\cdot\nabla_K H)\right]_w\\ &\quad+ \left[\nabla H(\nabla\hat{\mathbf{e}}\cdot\hat{\mathbf{e}}^*) + (\nabla\hat{\mathbf{e}}\cdot\hat{\mathbf{e}}^*)\nabla H\right]_w\\ &\quad+ \left[\boldsymbol{\Psi}\cdot\nabla_K H(\nabla\hat{\mathbf{e}}\cdot\hat{\mathbf{e}}^*) + (\boldsymbol{\Psi}\cdot\nabla_K\hat{\mathbf{e}}\cdot\hat{\mathbf{e}}^*)\nabla H\right]_w\\ &\quad+ \left[\nabla H(\boldsymbol{\Psi}\cdot\nabla_K\hat{\mathbf{e}}\cdot\hat{\mathbf{e}}^*) + (\nabla\hat{\mathbf{e}}\cdot\hat{\mathbf{e}}^*)\boldsymbol{\Psi}\cdot\nabla_K H\right]_w = 0.\end{aligned} \tag{2.67}$$

Here we use the notation $\boldsymbol{C}_w = (\mathbf{1} - \hat{\mathbf{g}}\hat{\mathbf{g}})\cdot\boldsymbol{C}\cdot(\mathbf{1} - \hat{\mathbf{g}}\hat{\mathbf{g}})$, where $\boldsymbol{C}$ is an arbitrary 3D matrix. We use equation (2.57) to get

$$\left(\frac{\mathrm{d}\boldsymbol{\Psi}}{\mathrm{d}\tau} + \boldsymbol{\Psi}\cdot\nabla_K\nabla_K H\cdot\boldsymbol{\Psi} + \boldsymbol{\Psi}\cdot\nabla_K\nabla H + \nabla\nabla_K H\cdot\boldsymbol{\Psi} + \nabla\nabla H\right)_w = 0, \tag{2.68}$$

which gives the components of $\mathrm{d}\boldsymbol{\Psi}/\mathrm{d}\tau$ perpendicular to the beam. To obtain the components parallel to the beam, $\mathrm{d}\boldsymbol{\Psi}/\mathrm{d}\tau\cdot\hat{\mathbf{g}}$, we differentiate equation (2.57) with respect to τ,

$$\frac{\mathrm{d}\boldsymbol{\Psi}}{\mathrm{d}\tau}\cdot\hat{\mathbf{g}} + (\boldsymbol{\Psi}\cdot\nabla_K\nabla_K H\cdot\boldsymbol{\Psi} + \boldsymbol{\Psi}\cdot\nabla_K\nabla H + \nabla\nabla_K H\cdot\boldsymbol{\Psi} + \nabla\nabla H)\cdot\hat{\mathbf{g}} = 0, \tag{2.69}$$

where we have used $\mathrm{d}(\partial_\mu H)/\mathrm{d}\tau = \mathbf{g}\cdot\nabla(\partial_\mu H) + \mathrm{d}\mathbf{K}/\mathrm{d}\tau\cdot\nabla_K(\partial_\mu H)$, equations (2.45), (2.46), and (2.57), as well as the symmetry of $\boldsymbol{\Psi}$. Recalling that $(\mathrm{d}\boldsymbol{\Psi}/\mathrm{d}\tau)_w = (\mathbf{1} - \hat{\mathbf{g}}\hat{\mathbf{g}})\cdot(\mathrm{d}\boldsymbol{\Psi}/\mathrm{d}\tau)\cdot(\mathbf{1} - \hat{\mathbf{g}}\hat{\mathbf{g}})$, equations (2.68) and (2.69) give

$$\frac{\mathrm{d}\boldsymbol{\Psi}}{\mathrm{d}\tau} + \boldsymbol{\Psi}\cdot\nabla_K\nabla_K H\cdot\boldsymbol{\Psi} + \boldsymbol{\Psi}\cdot\nabla_K\nabla H + \nabla\nabla_K H\cdot\boldsymbol{\Psi} + \nabla\nabla H = 0. \tag{2.70}$$

2.1.4.2 Pieces independent of w

Using equations (2.25) and (2.58), the terms independent of $\mathbf{w}$ in equation (2.60) give

$$\begin{aligned}
&\frac{1}{gA^{(0)}}\left[(\mathbf{K}\cdot\hat{\mathbf{e}})\hat{\mathbf{e}}^* + (\mathbf{K}\cdot\hat{\mathbf{e}}^*)\hat{\mathbf{e}} - 2\mathbf{K}\right]\cdot\hat{\mathbf{g}}\frac{\mathrm{d}A^{(0)}}{\mathrm{d}\tau} \\
&\quad + \boldsymbol{\Psi} : (\hat{\mathbf{e}}^*\hat{\mathbf{e}} - \mathbf{1}) + \frac{1}{g}\left[(\hat{\mathbf{e}}^*\cdot\hat{\mathbf{g}})\frac{\mathrm{d}\hat{\mathbf{e}}}{\mathrm{d}\tau}\cdot\mathbf{K} + (\mathbf{K}\cdot\hat{\mathbf{e}}^*)\hat{\mathbf{g}}\cdot\frac{\mathrm{d}\hat{\mathbf{e}}}{\mathrm{d}\tau} - 2(\mathbf{K}\cdot\hat{\mathbf{g}})\frac{\mathrm{d}\hat{\mathbf{e}}}{\mathrm{d}\tau}\cdot\hat{\mathbf{e}}^*\right] \\
&\quad + \hat{\mathbf{e}}^*\cdot(\mathbf{1} - \hat{\mathbf{g}}\hat{\mathbf{g}})\cdot(\boldsymbol{\Psi}\cdot\nabla_K\hat{\mathbf{e}} + \nabla\hat{\mathbf{e}})\cdot\mathbf{K} \\
&\quad + (\mathbf{K}\cdot\hat{\mathbf{e}}^*)(\mathbf{1} - \hat{\mathbf{g}}\hat{\mathbf{g}}) : (\boldsymbol{\Psi}\cdot\nabla_K\hat{\mathbf{e}} + \nabla\hat{\mathbf{e}}) \\
&\quad - 2\mathbf{K}\cdot(\mathbf{1} - \hat{\mathbf{g}}\hat{\mathbf{g}})\cdot(\boldsymbol{\Psi}\cdot\nabla_K\hat{\mathbf{e}} + \nabla\hat{\mathbf{e}})\cdot\hat{\mathbf{e}}^* = 0.
\end{aligned} \tag{2.71}$$

Noting that equation (2.57) can be used to write

$$g\hat{\mathbf{g}}\cdot(\boldsymbol{\Psi}\cdot\nabla_K\hat{\mathbf{e}} + \nabla\hat{\mathbf{e}}) = \frac{\mathrm{d}\mathbf{K}}{\mathrm{d}\tau}\cdot\nabla_K\hat{\mathbf{e}} + \frac{\mathrm{d}\mathbf{q}}{\mathrm{d}\tau}\cdot\nabla\hat{\mathbf{e}} = \frac{\mathrm{d}\hat{\mathbf{e}}}{\mathrm{d}\tau}, \tag{2.72}$$

we find that

$$\begin{aligned}
&\frac{1}{g}\left[(\hat{\mathbf{e}}^*\cdot\hat{\mathbf{g}})\frac{\mathrm{d}\hat{\mathbf{e}}}{\mathrm{d}\tau}\cdot\mathbf{K} + (\mathbf{K}\cdot\hat{\mathbf{e}}^*)\hat{\mathbf{g}}\cdot\frac{\mathrm{d}\hat{\mathbf{e}}}{\mathrm{d}\tau} - 2(\mathbf{K}\cdot\hat{\mathbf{g}})\frac{\mathrm{d}\hat{\mathbf{e}}}{\mathrm{d}\tau}\cdot\hat{\mathbf{e}}^*\right] \\
&\qquad = (\hat{\mathbf{e}}^*\cdot\hat{\mathbf{g}})\hat{\mathbf{g}}\cdot(\boldsymbol{\Psi}\cdot\nabla_K\hat{\mathbf{e}} + \nabla\hat{\mathbf{e}})\cdot\mathbf{K} + (\mathbf{K}\cdot\hat{\mathbf{e}}^*)\hat{\mathbf{g}}\hat{\mathbf{g}} : (\boldsymbol{\Psi}\cdot\nabla_K\hat{\mathbf{e}} + \nabla\hat{\mathbf{e}}) \\
&\qquad - 2(\mathbf{K}\cdot\hat{\mathbf{g}})\hat{\mathbf{g}}\cdot(\boldsymbol{\Psi}\cdot\nabla_K\hat{\mathbf{e}} + \nabla\hat{\mathbf{e}})\cdot\hat{\mathbf{e}}^*.
\end{aligned} \tag{2.73}$$

Using equations (2.34), (2.45), and (2.73), equation (2.71) becomes

$$\begin{aligned}
&\frac{\Omega^2}{c^2}\frac{\mathrm{d}\ln A^{(0)}}{\mathrm{d}\tau} + \boldsymbol{\Psi} : (\hat{\mathbf{e}}^*\hat{\mathbf{e}} - \mathbf{1}) + \hat{\mathbf{e}}^*\cdot(\boldsymbol{\Psi}\cdot\nabla_K\hat{\mathbf{e}} + \nabla\hat{\mathbf{e}})\cdot\mathbf{K} \\
&\qquad + (\mathbf{K}\cdot\hat{\mathbf{e}}^*)(\boldsymbol{\Psi} : \nabla_K\hat{\mathbf{e}} + \nabla\cdot\hat{\mathbf{e}}) - 2\mathbf{K}\cdot(\boldsymbol{\Psi}\cdot\nabla_K\hat{\mathbf{e}} + \nabla\hat{\mathbf{e}})\cdot\hat{\mathbf{e}}^* = 0.
\end{aligned} \tag{2.74}$$

Noting that

$$\hat{\mathbf{e}}^*\cdot\frac{\partial\boldsymbol{D}}{\partial K_\mu}\cdot\partial_\nu\hat{\mathbf{e}} = \frac{c^2}{\Omega^2}(\mathbf{K}\cdot\hat{\mathbf{e}}^*)\partial_\nu\hat{e}_\mu + \frac{c^2}{\Omega^2}(\mathbf{K}\cdot\partial_\nu\hat{\mathbf{e}})\hat{e}^*_\mu - 2\frac{c^2}{\Omega^2}(\hat{\mathbf{e}}^*\cdot\partial_\nu\hat{\mathbf{e}})K_\mu, \tag{2.75}$$

$$\hat{\mathbf{e}}^*\cdot\frac{\partial^2\boldsymbol{D}}{\partial K_\mu\partial K_\nu}\cdot\hat{\mathbf{e}} = \frac{c^2}{\Omega^2}\hat{e}^*_\mu\hat{e}_\nu + \frac{c^2}{\Omega^2}\hat{e}_\mu\hat{e}^*_\nu - \frac{c^2}{\Omega^2}2\delta_{\mu\nu}, \tag{2.76}$$

and that $\boldsymbol{\Psi}$ is symmetric, we can simplify equation (2.74) further, getting

$$\begin{aligned}
&\frac{\mathrm{d}\ln A^{(0)}}{\mathrm{d}\tau} + \Psi_{\mu\nu}\left(\frac{1}{2}\hat{\mathbf{e}}^*\cdot\frac{\partial^2\boldsymbol{D}}{\partial K_\mu\partial K_\nu}\cdot\hat{\mathbf{e}} + \hat{\mathbf{e}}^*\cdot\frac{\partial\boldsymbol{D}}{\partial K_\mu}\cdot\frac{\partial\hat{\mathbf{e}}}{\partial K_\nu}\right) \\
&\qquad + \hat{\mathbf{e}}^*\cdot\frac{\partial\boldsymbol{D}}{\partial K_\mu}\cdot\frac{\partial\hat{\mathbf{e}}}{\partial r_\mu} = 0.
\end{aligned} \tag{2.77}$$

Using equation (2.66), equation (2.77) simplifies to

$$\frac{\mathrm{d}\ln A^{(0)}}{\mathrm{d}\tau} + \frac{1}{2}\boldsymbol{\Psi} : \nabla_K\nabla_K H + \nabla_K H \cdot \boldsymbol{\Psi} \cdot \nabla_K \hat{\mathbf{e}} \cdot \hat{\mathbf{e}}^* + \hat{\mathbf{e}}^* \cdot \frac{\partial \boldsymbol{D}}{\partial K_\mu} \cdot \frac{\partial \hat{\mathbf{e}}}{\partial r_\mu} = 0. \tag{2.78}$$

We then use equation (2.57), getting

$$\frac{\mathrm{d}\ln A^{(0)}}{\mathrm{d}\tau} + \frac{1}{2}\boldsymbol{\Psi} : \nabla_K\nabla_K H + \frac{\mathrm{d}\mathbf{K}}{\mathrm{d}\tau} \cdot \nabla_K \hat{\mathbf{e}} \cdot \hat{\mathbf{e}}^* + \hat{\mathbf{e}}^* \cdot \frac{\partial \boldsymbol{D}}{\partial K_\mu} \cdot \frac{\partial \hat{\mathbf{e}}}{\partial r_\mu} = 0. \tag{2.79}$$

To solve for $A^{(0)}$ using equation (2.79), we write $A^{(0)}$ as $A^{(0)} = |A^{(0)}|\exp(\mathrm{i}\phi^{(0)})$. The real part of equation (2.79) gives the equation for $|A^{(0)}|$, and its imaginary part the equation for $\phi^{(0)}$. The real part of equation (2.79) is

$$\frac{\mathrm{d}\ln|A^{(0)}|}{\mathrm{d}\tau} + \frac{1}{2}\mathrm{Re}(\boldsymbol{\Psi}) : \nabla_K\nabla_K H + \frac{1}{2}\left(\hat{\mathbf{e}}^* \cdot \frac{\partial \boldsymbol{D}}{\partial K_\mu} \cdot \frac{\partial \hat{\mathbf{e}}}{\partial r_\mu} + \frac{\partial \hat{\mathbf{e}}^*}{\partial r_\mu} \cdot \frac{\partial \boldsymbol{D}}{\partial K_\mu} \cdot \hat{\mathbf{e}}\right) = 0, \tag{2.80}$$

where we have used $\hat{\mathbf{e}} \cdot \partial\hat{\mathbf{e}}^*/\partial K_\mu + \hat{\mathbf{e}}^* \cdot \partial\hat{\mathbf{e}}/\partial K_\mu = \partial(\hat{\mathbf{e}}^* \cdot \hat{\mathbf{e}})/\partial K_\mu = 0$, the fact that $\partial\boldsymbol{D}/\partial K_\mu$ is Hermitian, and that only $\boldsymbol{\Psi}$ and $\hat{\mathbf{e}}$ are complex. We then differentiate $H = \hat{\mathbf{e}}^* \cdot \boldsymbol{D} \cdot \hat{\mathbf{e}}$ and use $\partial^2\boldsymbol{D}/\partial K_\mu \partial r_\nu = 0$ and equation (2.48) to obtain

$$\frac{\partial^2 H}{\partial K_\mu \partial r_\mu} = \frac{\partial \hat{\mathbf{e}}^*}{\partial r_\mu} \cdot \frac{\partial \boldsymbol{D}}{\partial K_\mu} \cdot \hat{\mathbf{e}} + \hat{\mathbf{e}}^* \cdot \frac{\partial \boldsymbol{D}}{\partial K_\mu} \cdot \frac{\partial \hat{\mathbf{e}}}{\partial r_\mu}, \tag{2.81}$$

to get

$$\frac{\mathrm{d}\ln|A^{(0)}|}{\mathrm{d}\tau} + \frac{1}{2}\mathrm{Re}(\boldsymbol{\Psi}) : \nabla_K\nabla_K H + \frac{1}{2}\nabla \cdot \nabla_K H = 0. \tag{2.82}$$

The magnitude $|A^{(0)}|$ is related to $\det[\mathrm{Im}(\boldsymbol{\Psi}_w)]$, where we have defined the determinant to be

$$\det(\boldsymbol{\Psi}_w) = \begin{vmatrix} \Psi_{xx} & \Psi_{xy} \\ \Psi_{yx} & \Psi_{yy} \end{vmatrix}. \tag{2.83}$$

To prove that $|A^{(0)}|$ is related to $\det[\mathrm{Im}(\boldsymbol{\Psi}_w)]$, we evaluate

$$\frac{\mathrm{d}}{\mathrm{d}\tau}\det[\mathrm{Im}(\boldsymbol{\Psi}_w)] = \det[\mathrm{Im}(\boldsymbol{\Psi}_w)][\mathrm{Im}(\boldsymbol{\Psi}_w)]^{-1} : \frac{\mathrm{d}\ \mathrm{Im}(\boldsymbol{\Psi}_w)}{\mathrm{d}\tau}, \tag{2.84}$$

where we define

$$\boldsymbol{\Psi}_w^{-1} = \begin{pmatrix} \begin{pmatrix} \Psi_{xx} & \Psi_{xy} \\ \Psi_{yx} & \Psi_{yy} \end{pmatrix}^{-1} & \begin{matrix} 0 \\ 0 \end{matrix} \\ \begin{matrix} 0 & 0 \end{matrix} & 0 \end{pmatrix}. \tag{2.85}$$

We use equation (2.70) to find d $\mathrm{Im}(\boldsymbol{\Psi})/\mathrm{d}\tau$, which is

$$\begin{aligned}\frac{\mathrm{d}\ \mathrm{Im}(\boldsymbol{\Psi})}{\mathrm{d}\tau} =& -\mathrm{Im}(\boldsymbol{\Psi})\cdot\nabla_K\nabla_K H\cdot\mathrm{Re}(\boldsymbol{\Psi}) - \mathrm{Re}(\boldsymbol{\Psi})\cdot\nabla_K\nabla_K H\cdot\mathrm{Im}(\boldsymbol{\Psi})\\ &-\mathrm{Im}(\boldsymbol{\Psi})\cdot\nabla_K\nabla H - \nabla\nabla_K H\cdot\mathrm{Im}(\boldsymbol{\Psi}).\end{aligned} \tag{2.86}$$

Substituting equation (2.86) into equation (2.84), and using $\mathrm{Im}(\boldsymbol{\Psi}_w)\cdot[\mathrm{Im}(\boldsymbol{\Psi}_w)]^{-1} = \mathbf{1}-\hat{\mathbf{g}}\hat{\mathbf{g}}$, we get

$$\frac{\mathrm{d}}{\mathrm{d}\tau}\ln(\det[\mathrm{Im}(\boldsymbol{\Psi}_w)]) = -2(\mathbf{1}-\hat{\mathbf{g}}\hat{\mathbf{g}}) : [\mathrm{Re}(\boldsymbol{\Psi})\cdot\nabla_K\nabla_K H + \nabla_K\cdot\nabla H]. \tag{2.87}$$

Using this result and equation (2.82), we find

$$\frac{\mathrm{d}\ln|A^{(0)}|}{\mathrm{d}\tau} = \frac{1}{4}\frac{\mathrm{d}}{\mathrm{d}\tau}\ln(\det[\mathrm{Im}(\boldsymbol{\Psi}_w)]) - \frac{1}{2}\hat{\mathbf{g}}\cdot\mathrm{Re}(\boldsymbol{\Psi})\cdot\nabla_K\nabla_K H\cdot\hat{\mathbf{g}} - \frac{1}{2}\hat{\mathbf{g}}\cdot\nabla_K\nabla H\cdot\hat{\mathbf{g}}. \tag{2.88}$$

Using the fact that $\hat{\mathbf{g}}$ is purely real and taking the real part of equation (2.57), we find that

$$\hat{\mathbf{g}}\cdot\mathrm{Re}(\boldsymbol{\Psi}) = \frac{1}{g}\frac{\mathrm{d}\mathbf{K}}{\mathrm{d}\tau}. \tag{2.89}$$

Hence,

$$\begin{aligned}&\hat{\mathbf{g}}\cdot\mathrm{Re}(\boldsymbol{\Psi})\cdot\nabla_K\nabla_K H\cdot\hat{\mathbf{g}} + \hat{\mathbf{g}}\cdot\nabla_K\nabla H\cdot\hat{\mathbf{g}}\\ &\quad= \frac{\hat{\mathbf{g}}}{g}\cdot\nabla_K\nabla_K H\cdot\frac{\mathrm{d}\mathbf{K}}{\mathrm{d}\tau} + \frac{\hat{\mathbf{g}}}{g}\cdot\nabla\nabla_K H\cdot\frac{\mathrm{d}\mathbf{q}}{\mathrm{d}\tau},\end{aligned} \tag{2.90}$$

where we have used the definition of group velocity in equation (2.45). Substituting this result into equation (2.88), and noting that

$$\frac{\mathrm{d}\mathbf{g}}{\mathrm{d}\tau} = \frac{\mathrm{d}}{\mathrm{d}\tau}(\nabla_K H) = \frac{\mathrm{d}\mathbf{K}}{\mathrm{d}\tau}\cdot\nabla_K\nabla_K H + \frac{\mathrm{d}\mathbf{q}}{\mathrm{d}\tau}\cdot\nabla\nabla_K H, \tag{2.91}$$

we find

$$\frac{\mathrm{d}\ln|A^{(0)}|}{\mathrm{d}\tau} = \frac{1}{4}\frac{\mathrm{d}}{\mathrm{d}\tau}\ln(\det[\mathrm{Im}(\boldsymbol{\Psi}_w)]) - \frac{1}{2}\frac{\hat{\mathbf{g}}}{g}\cdot\frac{\mathrm{d}\mathbf{g}}{\mathrm{d}\tau}. \tag{2.92}$$

Using $g^{-1}\hat{\mathbf{g}}\cdot\mathrm{d}\mathbf{g}/\mathrm{d}\tau = \mathrm{d}\ln g/\mathrm{d}\tau$ and simplifying, we get

$$|A^{(0)}| = C\frac{[\det(\mathrm{Im}(\boldsymbol{\Psi}_w))]^{\frac{1}{4}}}{g^{\frac{1}{2}}}, \tag{2.93}$$

where C is a constant of integration.

The imaginary part of equation (2.79) gives us

$$\frac{\mathrm{d}\phi^{(0)}}{\mathrm{d}\tau} = \mathrm{Im}(\boldsymbol{\Psi}) : \nabla_K \nabla_K H \\ - \mathrm{i}\frac{\mathrm{d}K_\mu}{\mathrm{d}\tau} \cdot \nabla_K \hat{\mathbf{e}} \cdot \hat{\mathbf{e}}^* + \frac{1}{2\mathrm{i}} \left(\hat{\mathbf{e}}^* \cdot \frac{\partial \boldsymbol{D}}{\partial K_\mu} \cdot \frac{\partial \hat{\mathbf{e}}}{\partial r_\mu} - \frac{\partial \hat{\mathbf{e}}^*}{\partial r_\mu} \cdot \frac{\partial \boldsymbol{D}}{\partial K_\mu} \cdot \hat{\mathbf{e}} \right), \tag{2.94}$$

where we have once again used $\hat{\mathbf{e}} \cdot \partial \hat{\mathbf{e}}^* / \partial K_\mu + \hat{\mathbf{e}}^* \cdot \partial \hat{\mathbf{e}} / \partial K_\mu = \partial(\hat{\mathbf{e}}^* \cdot \hat{\mathbf{e}})/\partial K_\mu = 0$. Using equations (2.45) and (2.49), we can rewrite this equation as

$$\frac{\mathrm{d}\phi^{(0)}}{\mathrm{d}\tau} = -\mathrm{i}\frac{\mathrm{d}\hat{\mathbf{e}}}{\mathrm{d}\tau} \cdot \hat{\mathbf{e}}^* + \frac{1}{2\mathrm{i}} \left(\hat{\mathbf{e}}^* \cdot \frac{\partial \boldsymbol{D}}{\partial K_\mu} \cdot (\mathbf{1} - \hat{\mathbf{e}}\hat{\mathbf{e}}^*) \cdot \frac{\partial \hat{\mathbf{e}}}{\partial r_\mu} - \frac{\partial \hat{\mathbf{e}}^*}{\partial r_\mu} \cdot (\mathbf{1} - \hat{\mathbf{e}}\hat{\mathbf{e}}^*) \cdot \frac{\partial \boldsymbol{D}}{\partial K_\mu} \cdot \hat{\mathbf{e}} \right) \\ + \mathrm{Im}(\boldsymbol{\Psi}) : \nabla_K \nabla_K H. \tag{2.95}$$

For clarity, we have divided the polarisation dependent piece into two terms, one parallel to $\hat{\mathbf{e}}$, and the other perpendicular to it. Using equation (2.50), this simplifies to

$$\frac{\mathrm{d}\phi^{(0)}}{\mathrm{d}\tau} = \mathrm{Im}(\boldsymbol{\Psi}) : \nabla_K \nabla_K H \\ - \mathrm{i}\frac{\mathrm{d}\hat{\mathbf{e}}}{\mathrm{d}\tau} \cdot \hat{\mathbf{e}}^* + \frac{1}{2\mathrm{i}} \left(\frac{\partial \hat{\mathbf{e}}^*}{\partial K_\mu} \cdot \boldsymbol{D} \cdot \frac{\partial \hat{\mathbf{e}}}{\partial r_\mu} - \frac{\partial \hat{\mathbf{e}}^*}{\partial r_\mu} \cdot \boldsymbol{D} \cdot \frac{\partial \hat{\mathbf{e}}}{\partial K_\mu} \right). \tag{2.96}$$

We separate $\phi^{(0)}$ into two parts, the Gouy phase ϕ_G and the phase ϕ_P associated with how the polarisation changes when the probe beam passes through a plasma. The former is a beam effect, whereas the latter is a result from ray tracing. We define the phases ϕ_G and ϕ_P by their evolution equations,

$$\frac{\mathrm{d}\phi_G}{\mathrm{d}\tau} = \mathrm{Im}(\boldsymbol{\Psi}) : \nabla_K \nabla_K H, \tag{2.97}$$

and

$$\frac{\mathrm{d}\phi_P}{\mathrm{d}\tau} = -\mathrm{i}\frac{\mathrm{d}\hat{\mathbf{e}}}{\mathrm{d}\tau} \cdot \hat{\mathbf{e}}^* + \frac{1}{2\mathrm{i}} \left(\frac{\partial \hat{\mathbf{e}}^*}{\partial K_\mu} \cdot \boldsymbol{D} \cdot \frac{\partial \hat{\mathbf{e}}}{\partial r_\mu} - \frac{\partial \hat{\mathbf{e}}^*}{\partial r_\mu} \cdot \boldsymbol{D} \cdot \frac{\partial \hat{\mathbf{e}}}{\partial K_\mu} \right). \tag{2.98}$$

The $\mathrm{d}\hat{\mathbf{e}}/\mathrm{d}\tau \cdot \hat{\mathbf{e}}^*$ piece corrects for our choice of the vectors $\partial_\mu \hat{\mathbf{e}} \cdot \hat{\mathbf{e}}^*$, as discussed at the end of Section 2.1.3. If we had chosen the vectors $\partial_\mu \hat{\mathbf{e}} \cdot \hat{\mathbf{e}}^* = 0$, then we would get $\mathrm{d}\hat{\mathbf{e}}/\mathrm{d}\tau \cdot \hat{\mathbf{e}}^* = 0$. The other piece of $\mathrm{d}\phi_P/\mathrm{d}\tau$ is physical, and accounts for how the polarisation changes as the $\mathbf{B}$ and n_e varies along the beam path.

2.1.5 Summary of beam tracing equations

In the preceding portion of this section, we derived the equations to determine the functions of τ — $\mathbf{q}$, K_g, $\mathbf{K}_w$, $\boldsymbol{\Psi}_w$, $A^{(0)}$, and $\hat{\mathbf{e}}$. These equations are summarised here. First, we define

$$\boldsymbol{D}(\mathbf{q},\mathbf{K}) = \frac{c^2}{\Omega^2}\left(\mathbf{K}\mathbf{K} - K^2\mathbf{1}\right) + \boldsymbol{\epsilon}(\mathbf{q}). \tag{2.99}$$

Since $\boldsymbol{D}$ is Hermitian, we can find its eigenvalues and eigenvectors,

$$\boldsymbol{D}\cdot\hat{\mathbf{e}} = H\hat{\mathbf{e}}. \tag{2.100}$$

This equation defines the dispersion relation $H(\mathbf{q},\mathbf{K})$ corresponding to the polarisation $\hat{\mathbf{e}}(\mathbf{q},\mathbf{K})$. We want $H=0$ at all points along the central ray. One way to ensure that is to choose $\mathbf{K}$ such that $H=0$ at some arbitrary point $\mathbf{q}$ along the central ray. Then, evolve $\mathbf{q}$ and $\mathbf{K} = K_g\hat{\mathbf{g}} + \mathbf{K}_w$ using

$$\frac{\mathrm{d}\mathbf{q}}{\mathrm{d}\tau} = \nabla_K H, \tag{2.101}$$

and

$$\frac{\mathrm{d}\mathbf{K}}{\mathrm{d}\tau} = -\nabla H, \tag{2.102}$$

such that $H=0$ along the rest of the ray.

For convenience, instead of evolving $\boldsymbol{\Psi}_w$, we evolve the 3D matrix

$$\boldsymbol{\Psi}(\tau) = \nabla\nabla\psi\left(\tau, w_x=0, w_y=0\right), \tag{2.103}$$

from which $\boldsymbol{\Psi}_w$ is subsequently determined. The equation for $\boldsymbol{\Psi}$ is

$$\frac{\mathrm{d}\boldsymbol{\Psi}}{\mathrm{d}\tau} = -\left(\boldsymbol{\Psi}\cdot\nabla_K\nabla_K H\cdot\boldsymbol{\Psi} + \boldsymbol{\Psi}\cdot\nabla_K\nabla H + \nabla\nabla_K H\cdot\boldsymbol{\Psi} + \nabla\nabla H\right). \tag{2.104}$$

The matrix $\boldsymbol{\Psi}_w$ can be deduced from $\boldsymbol{\Psi}$ by projecting $\boldsymbol{\Psi}$ on the plane perpendicular to $\hat{\mathbf{g}}$.

Finally, we split the amplitude into its modulus and its phase,

$$A^{(0)} = \left|A^{(0)}\right| \exp\left[\mathrm{i}\left(\phi_G + \phi_P\right)\right]. \tag{2.105}$$

Its modulus is given by

$$\left|A^{(0)}\right| = C\left[\det\left(\mathrm{Im}\left(\boldsymbol{\Psi}_w\right)\right)\right]^{\frac{1}{4}} g^{-\frac{1}{2}}, \tag{2.106}$$

where C is a constant of integration and $\det\left[\mathrm{Im}\left(\boldsymbol{\Psi}_w\right)\right] = \mathrm{Im}\left(\Psi_{xx}\right)\mathrm{Im}\left(\Psi_{yy}\right) - \left[\mathrm{Im}\left(\Psi_{xy}\right)\right]^2$; its phase is $\phi_G + \phi_P$, which is composed of the Gouy phase ϕ_G, given by

$$\frac{\mathrm{d}\phi_G}{\mathrm{d}\tau} = -\mathrm{Im}(\boldsymbol{\Psi}) : \nabla_K \nabla_K H, \tag{2.107}$$

and the phase associated with the changing polarisation when propagating through a plasma ϕ_P, given by

$$\frac{\mathrm{d}\phi_P}{\mathrm{d}\tau} = \mathrm{i}\frac{\mathrm{d}\hat{\mathbf{e}}}{\mathrm{d}\tau}\cdot\hat{\mathbf{e}}^* - \frac{1}{2\mathrm{i}}\left(\frac{\partial\hat{\mathbf{e}}^*}{\partial K_\mu}\cdot\boldsymbol{D}\cdot\frac{\partial\hat{\mathbf{e}}}{\partial r_\mu} - \frac{\partial\hat{\mathbf{e}}^*}{\partial r_\mu}\cdot\boldsymbol{D}\cdot\frac{\partial\hat{\mathbf{e}}}{\partial K_\mu}\right). \tag{2.108}$$

Our derivation in 2.1, an alternative to Pereverzev's original work [47, 48], shows that the beam tracing equations for $\mathbf{q}$, K_g, $\mathbf{K}_w$, $\boldsymbol{\Psi}_w$, $A^{(0)}$, and $\hat{\mathbf{e}}$ are the result of forcing equation (2.5) to be a solution of equation (1.4).

Given the properties of the launch beam at the antenna, we can calculate how it evolves as it propagates into the plasma. This initial condition for a beam launched perpendicular to the surface of the antenna is

$$\mathbf{E}_{ant} = A_{ant}\hat{\mathbf{e}}_{ant}\exp\left(\frac{\mathrm{i}}{2}\mathbf{w}\cdot\boldsymbol{\Psi}_{w,ant}\cdot\mathbf{w}\right), \tag{2.109}$$

where we have chosen $\mathrm{i}s_{ant} = 0$, and noted that due to the vacuum dispersion relation, $\mathbf{K}_{w,ant} = 0$. The probe beam's electric field is thus

$$\begin{aligned}\mathbf{E}_b = A_{ant}\exp(\mathrm{i}\phi_G + \mathrm{i}\phi_P)\left[\frac{\det(\mathrm{Im}[\boldsymbol{\Psi}_w])}{\det(\mathrm{Im}[\boldsymbol{\Psi}_{w,ant}])}\right]^{\frac{1}{4}}\sqrt{\frac{g_{ant}}{g}} \\ \times\hat{\mathbf{e}}\exp\left(\mathrm{i}s + \mathrm{i}\mathbf{K}_w\cdot\mathbf{w} + \frac{\mathrm{i}}{2}\mathbf{w}\cdot\boldsymbol{\Psi}_w\cdot\mathbf{w}\right).\end{aligned} \tag{2.110}$$

2.2 Beam trace me up, Scotty

To simulate the propagation of Gaussian beams in tokamak plasmas, we have developed a new code, Scotty. It is a beam tracing code written in Python 3, entirely in cylindrical coordinates (R, ζ, Z), with an option to convert the output to Cartesian coordinates (X, Y, Z). The lab Cartesian coordinates X and Y are not to be confused with the beam-aligned coordinates x and y. Using cylindrical coordinates exploits the toroidal symmetry of tokamak plasmas, simplifying the beam tracing equations. Hence, although the theoretical work presented in this thesis is applicable to stellarators (in

regions where the appropriate orderings and approximations hold), Scotty cannot be used out-of-the-box for such devices. Nonetheless, the results presented in this thesis would still be applicable; one would just need to run a suitable beam-tracing code and post-process the output appropriately.

In cylindrical coordinates, we have $H(R, Z, K_R, K_\zeta, K_Z)$: a very natural choice of variables for a tokamak. The new spatial coordinates R, Z, ζ are defined as follows

$$R = \sqrt{X^2 + Y^2}, \tag{2.111}$$

$$\zeta = \tan^{-1}\left(\frac{Y}{X}\right), \tag{2.112}$$

$$Z = Z. \tag{2.113}$$

The components of $\mathbf{K}$ in the new coordinate system are

$$K_R = K_X \cos\zeta + K_Y \sin\zeta, \tag{2.114}$$

$$K_\zeta = \left(-K_X \sin\zeta + K_Y \cos\zeta\right)\sqrt{X^2 + Y^2}, \tag{2.115}$$

and

$$K_Z = K_Z. \tag{2.116}$$

Note that K_ζ is the toroidal mode number, and is thus dimensionless, instead of having units of inverse length (unlike the other components of the wavevector). Hence, $\mathbf{K}$ becomes

$$\mathbf{K} = K_R \nabla R + K_\zeta \nabla\zeta + K_Z \nabla Z, \tag{2.117}$$

being careful to remember that we have $\nabla R = \hat{\mathbf{R}}$, $\nabla Z = \hat{\mathbf{Z}}$, but $\nabla\zeta = \hat{\boldsymbol{\zeta}}/R$.

Since Scotty was inspired by TORBEAM [51], it has the option to use the same input files for equilibrium data. Specifically, $\mathbf{B}$ and the poloidal flux ψ_p on a grid (R and Z), as well as electron density as a function of radial coordinate $\sqrt{\psi_p}$. We split the magnetic field into toroidal and poloidal components,

$$\mathbf{B} = B_\zeta \hat{\boldsymbol{\zeta}} + B_R \hat{\mathbf{R}} + B_Z \hat{\mathbf{Z}}, \tag{2.118}$$

where B_ζ is the toroidal component of the magnetic field, and B_R and B_Z are its poloidal components. Scotty can also calculate $\mathbf{B}$ directly from EFIT output: this is

done by using RB_ζ and numerically evaluating the gradients of ψ_p. The magnetic field is calculated as follows:

$$B_R = -\frac{1}{R}\frac{\partial \psi_p}{\partial Z}, \tag{2.119}$$

$$B_\zeta = \frac{1}{R} I\left(\psi_p(R,Z)\right), \tag{2.120}$$

where I is proportional to the poloidal current, an output of EFIT, and

$$B_Z = \frac{1}{R}\frac{\partial \psi_p}{\partial R}. \tag{2.121}$$

Scotty assumes lossless propagation as it is written specially for DBS. Since we use MAST plasmas as a case study in this work, we do not need to account for the relativistic correction to the electron mass. As such, in its current implementation Scotty does not use temperature profiles, although we expect to add the relativistic correction in the near future.

In its current implementation, Scotty matches boundary conditions at the plasma-vacuum edge, using the generalised Snell's law [49] for $\boldsymbol{\Psi}$ (like TORBEAM) but not for $\mathbf{K}$ (unlike TORBEAM). Consequently, a possible discontinuity in $\nabla\nabla H$ arising from a sudden change in the density gradient is properly handled; see Appendix A for details.

The definitions of K_R, K_ζ, K_Z, in equations (2.114), (2.115), and (2.116) were chosen such that the electric field has the form:

$$\begin{aligned}\mathbf{E}_b \propto \exp\Big[&\mathrm{i}s + \mathrm{i}K_R\Delta R + \mathrm{i}K_Z\Delta Z + \mathrm{i}K_\zeta\Delta\zeta \\ &+ \frac{\mathrm{i}}{2}\big(\Psi_{RR}\left(\Delta R\right)^2 + 2\Psi_{RZ}\Delta R\Delta Z + \Psi_{ZZ}\left(\Delta Z\right)^2 \\ &+ \Psi_{\zeta\zeta}\left(\Delta\zeta\right)^2 + 2\Psi_{R\zeta}\Delta R\Delta\zeta + 2\Psi_{\zeta Z}\Delta\zeta\Delta Z\big)\Big],\end{aligned} \tag{2.122}$$

which gives us the definitions of the components of $\boldsymbol{\Psi}$ in cylindrical coordinates. The components Ψ_{RR}, Ψ_{ZZ}, $\Psi_{\zeta\zeta}$, Ψ_{RZ}, $\Psi_{R\zeta}$, and $\Psi_{Z\zeta}$ of the matrix $\boldsymbol{\Psi}$ in the new coordinate system must satisfy

$$\Psi_{\alpha\beta}(\tau) = \frac{\partial^2 \psi}{\partial r_\alpha \partial r_\beta}\left(\tau, w_x = 0, w_y = 0\right). \tag{2.123}$$

Hence, they are

$$\Psi_{RR} = \Psi_{XX}\cos^2\zeta + 2\Psi_{XY}\sin\zeta\cos\zeta + \Psi_{YY}\sin^2\zeta, \tag{2.124}$$

$$\Psi_{ZZ} = \Psi_{ZZ}, \tag{2.125}$$

$$\begin{aligned}\Psi_{\zeta\zeta} = &\left[\Psi_{XX}\sin^2\zeta - 2\Psi_{XY}\sin\zeta\cos\zeta + \Psi_{YY}\cos^2\zeta\right]\left(X^2+Y^2\right)\\ &- \left(K_X\cos\zeta + K_Y\sin\zeta\right)\sqrt{X^2+Y^2},\end{aligned} \tag{2.126}$$

$$\Psi_{RZ} = \Psi_{XZ}\cos\zeta + \Psi_{YZ}\sin\zeta, \tag{2.127}$$

$$\begin{aligned}\Psi_{R\zeta} = &\left[-\Psi_{XX}\sin\zeta\cos\zeta + \Psi_{XY}\left(\cos^2\zeta - \sin^2\zeta\right) + \Psi_{YY}\sin\zeta\cos\zeta\right]\sqrt{X^2+Y^2}\\ &- K_X\sin\zeta + K_Y\cos\zeta,\end{aligned} \tag{2.128}$$

$$\Psi_{Z\zeta} = \left(-\Psi_{XZ}\sin\zeta + \Psi_{YZ}\cos\zeta\right)\sqrt{X^2+Y^2}. \tag{2.129}$$

The rest of the elements can be found by remembering that $\boldsymbol{\Psi}$ is symmetric.

With these new variables, the gradients become

$$\nabla = \nabla R\frac{\partial}{\partial R} + \nabla\zeta\frac{\partial}{\partial\zeta} + \nabla Z\frac{\partial}{\partial Z}, \tag{2.130}$$

and

$$\nabla_K = \nabla_K K_R\frac{\partial}{\partial K_R} + \nabla_K K_\zeta\frac{\partial}{\partial K_\zeta} + \nabla_K K_Z\frac{\partial}{\partial K_Z}. \tag{2.131}$$

Using all these properties, we can write the evolution equations in a way which makes their Hamiltonian character explicit,

$$\frac{\mathrm{d}q_\alpha}{\mathrm{d}\tau} = \frac{\partial H}{\partial K_\alpha}, \tag{2.132}$$

$$\frac{\mathrm{d}K_\alpha}{\mathrm{d}\tau} = -\frac{\partial H}{\partial r_\alpha}, \tag{2.133}$$

and

$$\frac{\mathrm{d}\Psi_{\alpha\beta}}{\mathrm{d}\tau} = -\frac{\partial^2 H}{\partial r_\alpha\partial r_\beta} - \Psi_{\alpha\gamma}\frac{\partial^2 H}{\partial K_\gamma\partial r_\beta} - \frac{\partial^2 H}{\partial r_\alpha\partial K_\eta}\Psi_{\eta\beta} - \Psi_{\alpha\gamma}\frac{\partial^2 H}{\partial K_\gamma\partial K_\eta}\Psi_{\eta\beta}. \tag{2.134}$$

Here we note that while $\mathrm{d}q_\zeta/\mathrm{d}\tau = \partial H/\partial K_\zeta$, the corresponding component of group velocity, given by

$$\mathbf{g} = \nabla_K H, \tag{2.135}$$

is $g_\zeta = R\ \partial H/\partial K_\zeta$; $\mathrm{d}q_\zeta/\mathrm{d}\tau = \partial H/\partial K_\zeta$ is an angular velocity, while g_ζ is a linear velocity, and they have different units.

Moving forward, the most obvious simplification to the above equations is due to toroidal symmetry: spatial gradients of equilibrium properties in the toroidal direction are zero, that is, $\partial H/\partial\zeta = 0$.

We proceed to solve these equations numerically, evolving $\boldsymbol{\Psi}$, from which $\boldsymbol{\Psi}_w$ may be obtained. Since $\boldsymbol{\Psi}$ is symmetric, it only has six independent components. We can further reduce the number of such components: equation (2.57) means we can reduce it by three. Hence, it is in principle possible to solve for only three independent components of $\boldsymbol{\Psi}$. However, we deemed the implementation too complex given the unclear benefits, which is why we have made a conscious design decision to solve for all six components

The initial conditions required by Scotty for the beam are as follows: frequency, initial beam widths and curvatures, poloidal φ_p and toroidal φ_t launch angles, and launch position. Note that only the initial q_R and q_Z need to be specified. The toroidal angle is taken to be zero at launch, $q_\zeta = 0$. The launch angles are defined the same way as TORBEAM [51], and are used to initialise $\mathbf{K}_{ant}$ as follows,

$$K_{R,ant} = -\frac{\Omega}{c}\cos\varphi_t \cos\varphi_p, \tag{2.136}$$

$$K_{\zeta,ant} = -\frac{\Omega}{c} R_{ant} \sin\varphi_t \cos\varphi_p, \tag{2.137}$$

$$K_{Z,ant} = -\frac{\Omega}{c}\sin\varphi_p. \tag{2.138}$$

Scotty uses SciPy's initial value problem solver to evolve the beam tracing ODEs. The solver has the option to easily switch between various integration methods. For this thesis, we use an explicit Runge-Kutta method of order 5(4) [58, 59].

Having broadly described the workings of Scotty, we proceed to describe our choice of dispersion relation, and the subtleties involved in doing this correctly (Section 2.2.1). After which, we lay out the parameters for two test cases that we use throughout Chapters 3–8 to illustrate our analytical results (Section 2.2.2). Chapter 9 deals more deeply with experimental data, and thus does not use these test cases.

2.2.1 Dispersion relation

In our derivation of beam tracing, the dispersion relation H is defined in equation (2.100). To calculate H, we first express the various components of the cold plasma dielectric tensor in the orthonormal basis $(\hat{\mathbf{u}}_1, \hat{\mathbf{u}}_2, \hat{\mathbf{b}})$. The $\hat{\mathbf{u}}_1$ and $\hat{\mathbf{u}}_2$ directions are perpendicular to $\hat{\mathbf{b}}$, and the $\hat{\mathbf{u}}_1$ direction together with $\hat{\mathbf{b}}$ defines a plane that contains $\mathbf{K}$, while $\hat{\mathbf{u}}_2$ is perpendicular to the plane of $\hat{\mathbf{b}}$ and $\mathbf{K}$. In this basis,

$$\boldsymbol{\epsilon} = \begin{pmatrix} \epsilon_{11} & -\mathrm{i}\epsilon_{12} & 0 \\ \mathrm{i}\epsilon_{12} & \epsilon_{11} & 0 \\ 0 & 0 & \epsilon_{bb} \end{pmatrix}, \tag{2.139}$$

where

$$\epsilon_{11} = 1 - \frac{\Omega_{pe}^2}{\Omega^2 - \Omega_{ce}^2}, \qquad \epsilon_{12} = \frac{\Omega_{pe}^2 \Omega_{ce}}{\Omega\left(\Omega^2 - \Omega_{ce}^2\right)}, \qquad \epsilon_{bb} = 1 - \frac{\Omega_{pe}^2}{\Omega^2}. \tag{2.140}$$

Here the subscripts $_1$, $_2$, and $_b$ denote the components in the $\hat{\mathbf{u}}_1$, $\hat{\mathbf{u}}_2$, and $\hat{\mathbf{b}}$ directions respectively. The components of $\boldsymbol{D}$ are

$$\boldsymbol{D} = \begin{pmatrix} D_{11} & -\mathrm{i}D_{12} & D_{1b} \\ \mathrm{i}D_{12} & D_{22} & 0 \\ D_{1b} & 0 & D_{bb} \end{pmatrix}, \tag{2.141}$$

where

$$D_{11} = \epsilon_{11} - \frac{c^2}{\Omega^2} K^2 \sin^2\theta_m, \tag{2.142}$$

$$D_{22} = \epsilon_{11} - \frac{c^2}{\Omega^2} K^2, \tag{2.143}$$

$$D_{bb} = \epsilon_{bb} - \frac{c^2}{\Omega^2} K^2 \cos^2\theta_m, \tag{2.144}$$

$$D_{12} = \epsilon_{12}, \tag{2.145}$$

$$D_{1b} = \frac{c^2}{\Omega^2} K^2 \sin\theta_m \cos\theta_m. \tag{2.146}$$

Here, the mismatch angle θ_m is defined in Figure 1.3. We proceed to solve the eigenvalue equation

$$\det\left(\boldsymbol{D} - H\mathbf{1}\right) = \begin{vmatrix} D_{11} - H & -\mathrm{i}D_{12} & D_{1b} \\ \mathrm{i}D_{12} & D_{22} - H & 0 \\ D_{1b} & 0 & D_{bb} - H \end{vmatrix} = 0, \tag{2.147}$$

getting

$$H^3 + h_2 H^2 + h_1 H + h_0 = 0, \tag{2.148}$$

where the coefficients h_2, h_1, and h_0 are

$$h_2 = -D_{11} - D_{22} - D_{bb}, \tag{2.149}$$

$$h_1 = D_{11}D_{bb} + D_{11}D_{22} + D_{22}D_{bb} - D_{12}^2 - D_{1b}^2, \tag{2.150}$$

and

$$h_0 = D_{22}D_{1b}^2 + D_{bb}D_{12}^2 - D_{11}D_{22}D_{bb}. \tag{2.151}$$

We use Cardano's formula to solve for H, getting three possible solutions

$$H_1 = \frac{h_t}{3\sqrt[3]{2}} - \sqrt[3]{2}\frac{3h_1 - h_2^2}{3h_t} - \frac{h_2}{3}, \tag{2.152}$$

$$H_2 = -\frac{1 - i\sqrt{3}}{6\sqrt[3]{2}}h_t + \left(1 + i\sqrt{3}\right)\frac{3h_1 - h_2^2}{3\sqrt[3]{4}h_t} - \frac{h_2}{3}, \tag{2.153}$$

and

$$H_3 = -\frac{1 + i\sqrt{3}}{6\sqrt[3]{2}}h_t + \left(1 - i\sqrt{3}\right)\frac{3h_1 - h_2^2}{3\sqrt[3]{4}h_t} - \frac{h_2}{3}, \tag{2.154}$$

where we have used the shorthand

$$h_t = \left[-2h_2^3 + 9h_2h_1 - 27h_0 + 3\sqrt{3}\left(4h_2^3h_0 - h_2^2h_1^2 - 18h_2h_1h_0 + 4h_1^3 + 27h_0^2\right)^{\frac{1}{2}}\right]^{\frac{1}{3}}. \tag{2.155}$$

To evolve the beam, we need to choose the solution that is zero along the entire path of the ray. Unfortunately, it is not immediately obvious which solutions correspond to the O and X modes. Moreover, Cardano's formula is complicated and cumbersome. Hence, we elect not to use this form of the dispersion relation to propagate the beam. We now prove that this is indeed a valid approach.

Instead of H, we used $\bar{H}\left(H(\mathbf{q}, \mathbf{K}), \mathbf{q}, \mathbf{K}\right)$, with the function $\bar{H}$ satisfying

$$\bar{H}(H = 0, \mathbf{q}, \mathbf{K}) = 0, \tag{2.156}$$

such that the derivatives of $\bar{H}$ with respect to $\mathbf{q}$ and $\mathbf{K}$ holding H constant vanish for $H = 0$. Bearing this in mind, we now evaluate the gradients of such an alternative dispersion relation, getting

$$\frac{\mathrm{d}\mathbf{K}}{\mathrm{d}\bar{\tau}} = -\nabla\bar{H}, \qquad \frac{\mathrm{d}\mathbf{q}}{\mathrm{d}\bar{\tau}} = \nabla_K\bar{H}, \tag{2.157}$$

and

$$\frac{\mathrm{d}\boldsymbol{\Psi}}{\mathrm{d}\bar{\tau}} = -\left(\boldsymbol{\Psi}\cdot\nabla_K\nabla_K\bar{H}\cdot\boldsymbol{\Psi} + \boldsymbol{\Psi}\cdot\nabla_K\nabla\bar{H} + \nabla\nabla_K\bar{H}\cdot\boldsymbol{\Psi} + \nabla\nabla\bar{H}\right), \tag{2.158}$$

where the new parameter $\bar{\tau}$ is defined by

$$\frac{\mathrm{d}\tau}{\mathrm{d}\bar{\tau}} = \frac{\partial\bar{H}}{\partial H}. \tag{2.159}$$

To obtain this result, we have used equation (2.57) in the derivation of equation (2.158). Here the derivatives of $\bar{H}$ are evaluated without holding H fixed, that is

$$\frac{\partial\bar{H}}{\partial\alpha} = \frac{\partial\bar{H}}{\partial H}\Big|_{\mathbf{q},\mathbf{K}}\frac{\partial H}{\partial\alpha} + \frac{\partial\mathbf{q}}{\partial\alpha}\cdot\nabla\bar{H}\Big|_{H,\mathbf{K}} + \frac{\partial\mathbf{K}}{\partial\alpha}\cdot\nabla_K\bar{H}\Big|_{H,\mathbf{q}}. \tag{2.160}$$

Consequently, we can calculate the beam parameters $\mathbf{q}$, $\mathbf{K}$, and $\boldsymbol{\Psi}$ from $\bar{H}$ as they are unaffected by choosing a new dispersion relation.

In our implementation of Scotty, we make the following choice for the dispersion relation $\bar{H}$: the solution of the Booker quartic [60, 61]

$$\bar{H} = K^2\frac{c^2}{\Omega^2} + \frac{\beta \pm \sqrt{\beta^2 - 4\alpha\gamma}}{2\alpha} = 0, \tag{2.161}$$

where

$$\alpha = \epsilon_{bb}\sin^2\theta_m + \epsilon_{11}\cos^2\theta_m, \tag{2.162}$$

$$\beta = -\epsilon_{11}\epsilon_{bb}\left(1+\sin^2\theta_m\right) - \left(\epsilon_{11}^2 - \epsilon_{12}^2\right)\cos^2\theta_m, \tag{2.163}$$

and

$$\gamma = \epsilon_{bb}\left(\epsilon_{11}^2 - \epsilon_{12}^2\right). \tag{2.164}$$

Recall that $\sin\theta_m$ is the mismatch angle, see Figure 1.3. The sign of the square root in equation (2.161) is chosen based on the mode. To figure out which sign corresponds to which mode, we consider the case where $\theta_m = 0$, getting

$$\frac{\beta \pm \sqrt{\beta^2 - 4\alpha\gamma}}{2\alpha} = \frac{-\epsilon_{11}^2 + \epsilon_{12}^2 - \epsilon_{11}\epsilon_{bb} \pm |\epsilon_{11}^2 - \epsilon_{12}^2 - \epsilon_{11}\epsilon_{bb}|}{2\epsilon_{11}.} \tag{2.165}$$

We need to choose the signs such that we recover $K^2c^2/\Omega^2 = \epsilon_{bb}$ for the O mode and $K^2c^2/\Omega^2 = \epsilon_{11} + \epsilon_{12}/\epsilon_{11}$ for the X mode. Thus, if $\epsilon_{11}^2 - \epsilon_{12}^2 - \epsilon_{11}\epsilon_{bb} > 0$, the $+$ of the $\pm$ corresponds to the O mode. If it is less than zero, then $-$ of the $\pm$ corresponds to

the O mode. The other sign, in either case, would correspond to the X mode. Scotty selects the appropriate sign, and uses this $\bar{H}(H, \mathbf{q}, \mathbf{K})$ in place of H to find $\mathbf{q}$, $\mathbf{K}$, and $\boldsymbol{\Psi}$. Should one wish to use a different dispersion relation, it would be straightforward to modify Scotty accordingly.

There are a few quantities that depend on the definition of H given in equation (2.100). These are equations (2.106), (2.107), and (2.108). In particular, the exact definition of g in equation (2.106) is crucial for our result on localisation in Chapter 6. Our calculation of group velocity is dependent on the choice of dispersion relation, since

$$\bar{\mathbf{g}} = \frac{\mathrm{d}\tau}{\mathrm{d}\bar{\tau}} \frac{\mathrm{d}\mathbf{q}}{\mathrm{d}\tau}, \tag{2.166}$$

where the dependence of $\mathrm{d}\tau/\mathrm{d}\bar{\tau}$ on our choice of H is given in equation (2.159). We use Cardano's solution in equations (2.152), (2.153), and (2.154) in post-processing to determine g_{ant} and g in equation (2.110) consistent with our definition of H.

2.2.2 Test cases

From this point up until Chapter 8 inclusive, we use two test cases to illustrate our results. One of these cases is entirely analytical, while the other uses equilibrium data from a real shot which was carried out at the Mega Ampere Spherical Tokamak (MAST). We detail these two cases here, and unless otherwise stated in relevant chapters, the parameters here are what we then use. In both cases, the probe beam's frequency was taken to be 55 GHz with O-mode polarisation. In Chapter 9, we move beyond these two test cases and assess the beam model's applicability to wider experimental data.

For our analytical equilibrium, we use a large aspect ratio, circular flux surface equilibrium. The toroidal component is given by

$$B_\zeta = B_{\zeta,a} \frac{R_a}{R}, \tag{2.167}$$

where R_a is the R of the magnetic axis and $B_{\zeta,a}$ is the corresponding toroidal magnetic field at the said axis. The poloidal field inside the last closed flux surface, $(R - R_a)^2 +$

$Z^2 = a^2$, where a is the minor radius, is

$$B_R = B_p \frac{Z}{\sqrt{(R - R_a)^2 + Z^2}}, \tag{2.168}$$

and

$$B_Z = B_p \frac{R - R_a}{\sqrt{(R - R_a)^2 + Z^2}}. \tag{2.169}$$

Here, inside the last closed flux surface, we have

$$B_p = B_{p,a} \frac{\sqrt{(R - R_a)^2 + Z^2}}{a}, \tag{2.170}$$

where $B_{p,a}$ is the magnitude of the poloidal magnetic field on the last closed flux surface. Unless otherwise stated, we use $B_{p,a} = 0.1\text{T}$, $B_{\zeta,a} = 1\text{T}$, $R_a = 1.5\text{m}$, and $a = 0.5\text{m}$. The density profile was linear in the normalised poloidal flux $\sqrt{\psi_p}$, going from $n_e = 4 \times 10^{19}\text{m}^{-3}$ at $\sqrt{\psi_p} = 0$ to zero density at $\sqrt{\psi_p} = 1$. A circular beam is launched at $q_R = 2.2\text{m}$ and $q_Z = 0\text{m}$, with $\varphi_p = 6°$, $\varphi_t = 0°$, $R_{b,x} = R_{b,y} = -4.0\text{m}$, and $W_x = W_y = 4\text{cm}$.

To illustrate our model's ability to deal with real plasmas, we chose MAST shot 29908, at 190ms, as our second test case. This was one of six repeated shots used to study the effect of mismatch in an earlier paper [30], in which DBS data was analysed for these shots at 190ms. The RB_ζ and the normalised poloidal flux density ψ_p were determined by MSE-constrained EFIT, and we used equations (2.119), (2.120), and (2.121) to calculate $\mathbf{B}$. We used SciPy's bivariate spline to interpolate ψ_p [58]. To ensure that the second spatial derivatives are smooth, we used a degree of 5 and a smoothing factor of 2. This does not significantly change the poloidal flux profile, as can be seen from Figure 2.1.

The density profile was acquired by Thomson scattering. We chose to fit the density data rather than smooth it because it was noisy, which made the evaluation of $\nabla\nabla n$, and thus $\mathrm{d}\boldsymbol{\Psi}/\mathrm{d}\tau$, challenging. Since data processing is not the main focus of this thesis, we instead use the following function to fit the density data

$$n_e = C_1 \tanh\left[C_2 \left(\psi_{p,n} - C_3\right)\right], \tag{2.171}$$

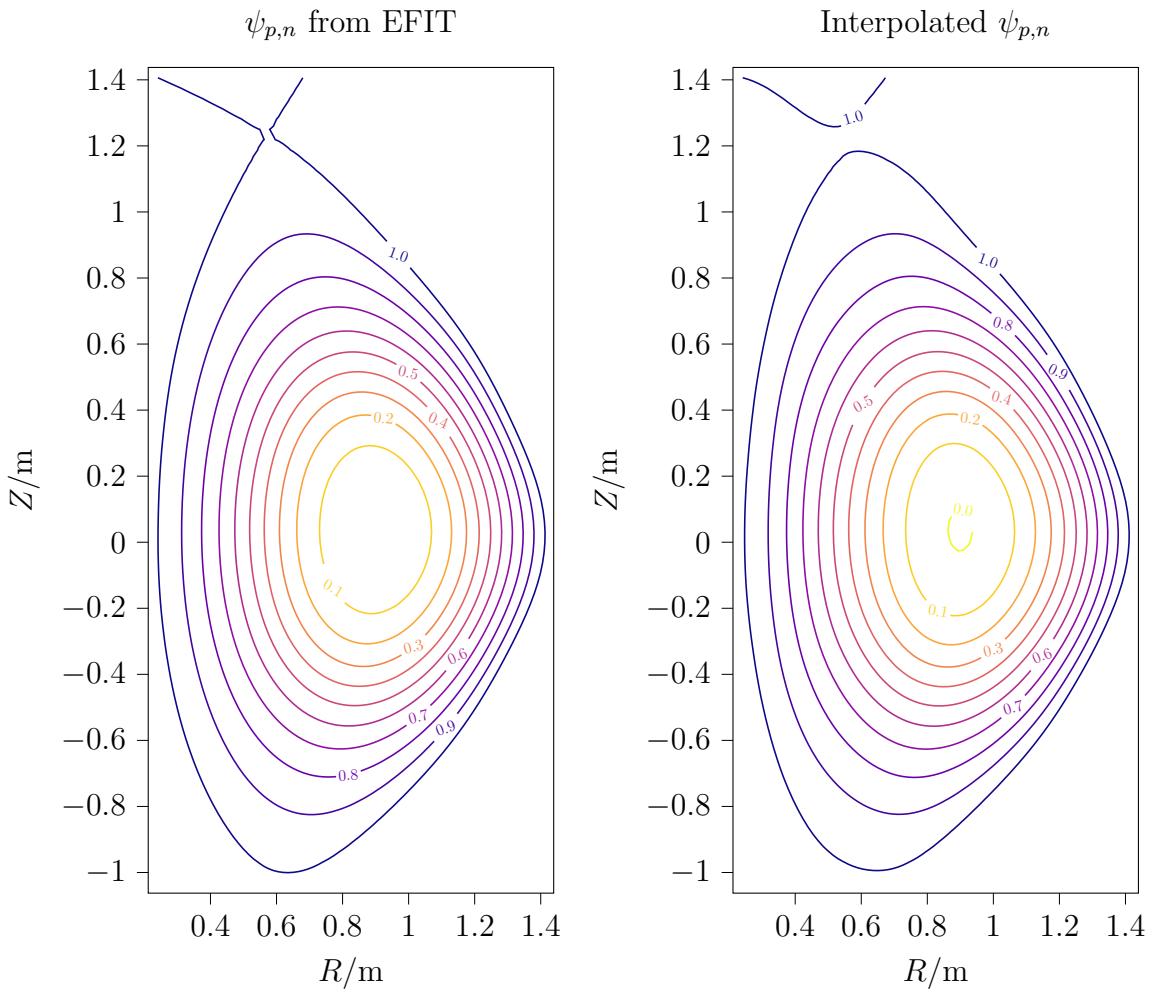

Figure 2.1: Data from MSE-constrained EFIT (left), after smoothing (right). Here $\psi_{p,n}$ is the normalised ψ_p such that $\psi_{p,n} = 1$ on the last closed flux surface and $\psi_{p,n} = 0$ on the magnetic axis (left). The smoothing spline (right) gives $\psi_{p,n} < 0$ in a region of space near the magnetic axis. Thankfully, the beam is never in that region in the simulations used for this thesis, so this is not an issue.

where $\psi_{p,n}$ is the normalised ψ_p such that $\psi_{p,n} = 1$ on the last closed flux surface and $\psi_{p,n} = 0$ on the magnetic axis. The coefficients $C_1 = 3.25 \times 10^{19}\mathrm{m}^{-3}$, $C_2 = -2.4$, and $C_3 = 1.22$ were determined via manual fitting by visual inspection. These coefficients were used by Scotty directly to calculate the density. Notice that the fit gives negative densities for $\psi_{p,n} > C_3$; at these values of ψ, the density is set to 0. The fit is not particularly good when $\psi_{p,n} \lesssim 0.4$; the experimental density profile is hollow. Fortunately, this is not a problem for the current work, since the beams studied in this thesis do not enter that region.

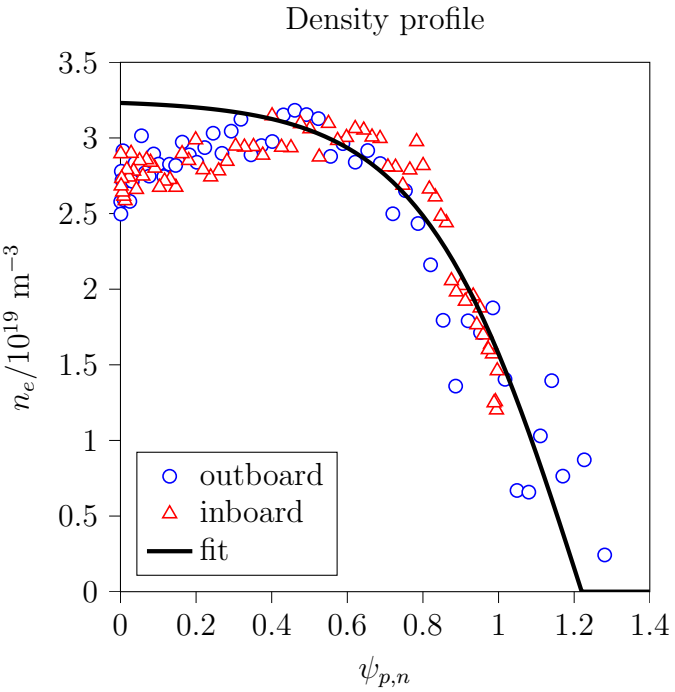

Figure 2.2: Electron density n_e data from the Thomson scattering diagnostic as a function of normalised poloidal flux (blue circles and red triangles, denoting measurements on the outboard and inboard respectively), hyperbolic tangent fit (black line). The fit is less good when $\psi_{p,n} \lesssim 0.4$; the experimental density profile is hollow. Fortunately, this is not a problem for the current work, since the beams studied in this thesis do not enter that region.

We launch a circular beam, at $q_R = 2.44\mathrm{m}$ and $q_Z = 0\mathrm{m}$, with $\varphi_p = 6°$, $\varphi_t = -6.4°$, $R_{b,x} = R_{b,y} = -72.8\mathrm{cm}$, and $W_x = W_y = 3.97\mathrm{cm}$. The launch beam's width and curvature were obtained from E-plane measurements of the 50 GHz beam of the MAST DBS [30]. This beam propagates through the plasma as given in Figure 2.3.

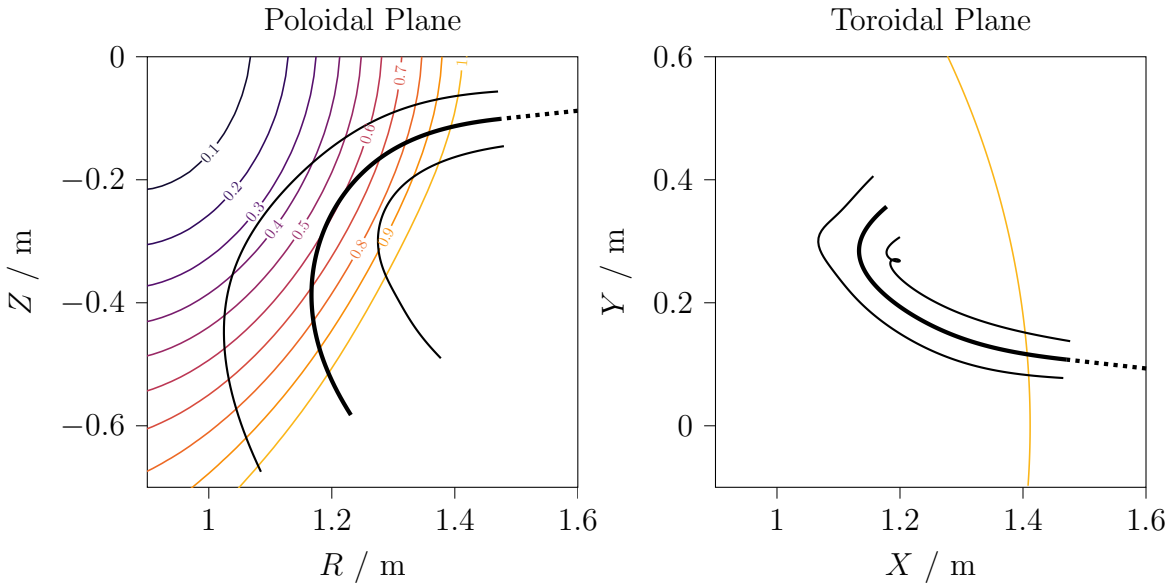

Figure 2.3: Beam propagation through MAST plasma, shot 29908 at 190ms. Poloidal (left) and toroidal (right) cross-sections. The orange line in the right figure shows the radial position of the last closed flux surface at the midplane. Thin solid lines give the 1/e positions of the Gaussian beam's electric field, and the dotted lines show the ray's propagation in vacuum. Notice that the thin solid line loops upon itself in the figure on the right: this is not an artefact, it is the result of the beam widening as it turns and travels a significant distance in the poloidal plane, while not propagating quite as far in the toroidal plane.

Chapter 3

Reciprocity theorem

The exact expression for the scattered electric field $\mathbf{E}_s$ is complicated. Coherent scattering in fusion plasmas has been studied extensively in cases where the wave frequency is much larger than the plasma frequency [62–64]. Since the frequency of the DBS beam is close to the plasma frequency, refraction is significant, making analysis even more challenging. Fortunately, we know that the emitted and received patterns of the antenna are the same. To simplify the subsequent equations, we define the antenna surface to be a surface perperpendicular to the beam propagation and close to the physical antenna. For the antenna to receive a wave, it must be of the same form as the emitted wave, shown in equation (2.109), but time reversed. Since the received and emitted waves are travelling in opposite directions, their wavevectors and beamfront curvatures, given by $\mathrm{Re}(\boldsymbol{\Psi})$, have opposite signs. The received and emitted waves must also have the same envelope, given by $\mathrm{Im}(\boldsymbol{\Psi})$, to pass through the optics of the DBS system. The polarisation of the emitted wave must be the same as that of the received wave. For example, an antenna emitting right circularly polarised light must also receive right circularly polarised light. However, the direction of travel has changed, and thus the direction the polarisation is moving also changes, as one might expect from time reversal symmetry. The received polarisation is thus the complex conjugate of that emitted. Consequently, at the antenna, the received scattered electric field must satisfy

$$\mathbf{E}_{r,ant} = A_r \hat{\mathbf{e}}^*_{ant} \exp\left(-\frac{\mathrm{i}}{2}\mathbf{w}\cdot\boldsymbol{\Psi}^*_{w,ant}\cdot\mathbf{w}\right), \tag{3.1}$$

where we have assumed that the antenna is in a vacuum and that the probe beam is launched perpendicular to the antenna surface. The scattered wave will be detected by the antenna if and only if it is of the form in equation (3.1).

To calculate A_r for a given $\mathbf{E}_s$, we project the scattered electric field on the Gaussian beam mode, the lowest order mode of the Gauss-Hermite beams, which form an orthogonal basis [65, 66],

$$A_r = \pi^{-1} \left[\det \left[\mathrm{Im}\left(\boldsymbol{\Psi}_{w,ant}\right)\right]\right]^{\frac{1}{2}} \int_{ant} \left[\mathbf{E}_s \cdot \hat{\mathbf{e}}_{ant} \exp\left(\frac{\mathrm{i}}{2}\mathbf{w} \cdot \boldsymbol{\Psi}_{w,ant} \cdot \mathbf{w}\right)\right] \mathrm{d}S. \tag{3.2}$$

The $\pi^{-1} \left[\det \left[\mathrm{Im}\left(\boldsymbol{\Psi}_{w,ant}\right)\right]\right]^{1/2}$ piece is the reciprocal of what we would get if we evaluated the 2D Gaussian surface integral, as shown in Appendix B.2. We have assumed that the DBS optics produces a sufficiently good Gaussian beam, such that the contribution to the signal from higher order modes is negligible.

We use reciprocity to obtain A_r without calculating $\mathbf{E}_s$ in its entirety. The reciprocity theorem is a standard method of calculating the signal received by an antenna. However, it cannot be used in its usual form when the medium is a magnetised plasma. In order to deal with highly magnetised plasmas in tokamaks, some modifications have to be made. Specifically, the reciprocal beam has to be launched into a plasma which has its dielectric tensor transposed [23, 24, 67], which is the same as having its magnetic field reversed. The dielectric tensor has to be transposed to maintain time reversal symmetry. Like previous work on reciprocity, we use the superscript $^{(+)}$ to denote solutions in the medium with the transposed dielectric tensor, which is

$$\frac{c^2}{\Omega^2} \nabla \times \left(\nabla \times \mathbf{E}^{(+)}\right) = \boldsymbol{\epsilon}_{eq}^{T} \cdot \mathbf{E}^{(+)}. \tag{3.3}$$

To obtain A_r in equation (3.2), we contract equation (1.5) with $\mathbf{E}^{(+)}$,

$$\frac{c^2}{\Omega^2} \mathbf{E}^{(+)} \cdot \nabla \times \left(\nabla \times \mathbf{E}_s\right) = \mathbf{E}^{(+)} \cdot \boldsymbol{\epsilon}_{eq} \cdot \mathbf{E}_s + \mathbf{E}^{(+)} \cdot \boldsymbol{\epsilon}_{tb} \cdot \mathbf{E}_b, \tag{3.4}$$

and integrate by parts, using equation (3.3) to obtain

$$\frac{c^2}{\Omega^2} \nabla \cdot \left[\left(\nabla \times \mathbf{E}_s\right) \times \mathbf{E}^{(+)} - \left(\nabla \times \mathbf{E}^{(+)}\right) \times \mathbf{E}_s\right] = \mathbf{E}^{(+)} \cdot \boldsymbol{\epsilon}_{tb} \cdot \mathbf{E}_b. \tag{3.5}$$

Choosing the right surface and the right boundary condition for $\mathbf{E}^{(+)}$ on that surface, one can calculate A_r from a volume integral of $\mathbf{E}^{(+)} \cdot \boldsymbol{\epsilon}_{tb} \cdot \mathbf{E}_b$,

$$\int [(\nabla \times \mathbf{E}_s) \times \mathbf{E}^{(+)} + \mathbf{E}_s \times (\nabla \times \mathbf{E}^{(+)})] \cdot \mathrm{d}\mathbf{S} = \int \frac{\Omega^2}{c^2} \mathbf{E}^{(+)} \cdot \boldsymbol{\epsilon}_{tb} \cdot \mathbf{E}_b \, \mathrm{d}V. \tag{3.6}$$

We impose that $\mathbf{E}^{(+)}$ at the antenna is

$$\mathbf{E}^{(+)}_{ant} = \pi^{-1} \left\{ \det \left[\mathrm{Im} \left(\boldsymbol{\Psi}_{w,ant} \right) \right] \right\}^{\frac{1}{2}} \hat{\mathbf{e}}_{ant} \exp \left(\frac{\mathrm{i}}{2} \mathbf{w} \cdot \boldsymbol{\Psi}_{w,ant} \cdot \mathbf{w} \right). \tag{3.7}$$

The behaviour of $\mathbf{E}^{(+)}$ as it propagates into the transposed plasma is governed by the beam tracing equations. The beam's evolution is governed by the dispersion relation $\boldsymbol{D} \cdot \hat{\mathbf{e}} = 0$, where $\boldsymbol{D}$ was defined in equation (2.99). When the dielectric tensor of the plasma is transposed, the dispersion relation is $\boldsymbol{D}^T \cdot \hat{\mathbf{e}}^{(+)} = 0$. The fact that $\boldsymbol{D}$ is Hermitian implies that $\boldsymbol{D}^\dagger \cdot \hat{\mathbf{e}} = 0$. Thus, $\boldsymbol{D}^T \cdot \hat{\mathbf{e}}^* = 0$, and we conclude that $\hat{\mathbf{e}}^{(+)} = \hat{\mathbf{e}}^*$. Intuitively, this makes sense, since transposing the dielectric tensor corresponds to switching the direction of the magnetic field; hence, left-handed polarisation in the transposed plasma behaves the same as right-handed polarisation in the physical plasma and vice versa. As such, the reciprocal beam $\mathbf{E}^{(+)}$ propagates like the probe beam $\mathbf{E}_b$, except for its polarisation being complex conjugated. Since $\mathbf{E}^{(+)}$ at the antenna, equation (3.7), has the same form as $\mathbf{E}_b$ at the antenna and follows the same set of evolution equations, except for the complex conjugated polarisation, the reciprocal beam is

$$\begin{aligned} \mathbf{E}^{(+)} = \pi^{-1} \sum_{i=O,X} \alpha_i \left\{ \det \left[\mathrm{Im} \left(\boldsymbol{\Psi}_{w,ant} \right) \right] \right\}^{\frac{1}{4}} \left\{ \det \left[\mathrm{Im} \left(\boldsymbol{\Psi}_{w,i} \right) \right] \right\}^{\frac{1}{4}} \left(\frac{g_{ant}}{g_i} \right)^{\frac{1}{2}} \\ \times \hat{\mathbf{e}}_i^* \exp(\mathrm{i}\phi_{G,i} - \mathrm{i}\phi_{P,i}) \exp \left(\mathrm{i}s_i + \mathrm{i}\mathbf{K}_{w,i} \cdot \mathbf{w}_i + \frac{\mathrm{i}}{2} \mathbf{w}_i \cdot \boldsymbol{\Psi}_{w,i} \cdot \mathbf{w}_i \right), \end{aligned} \tag{3.8}$$

where the coefficients α_i give the relative amplitudes of the O and X modes. We remark that ϕ_G does not change sign, unlike ϕ_P. We now match the expression for the reciprocal electric field, equation (3.8), with its initial condition, equation (3.7), giving

$$\hat{\mathbf{e}}_{ant} = \alpha_{O,ant} \hat{\mathbf{e}}^*_{O,ant} + \alpha_{X,ant} \hat{\mathbf{e}}^*_{X,ant}. \tag{3.9}$$

Since the dispersion relation $\boldsymbol{D}$ is Hermitian, its eigenvectors are orthogonal: $\hat{\mathbf{e}}_X \cdot \hat{\mathbf{e}}^*_O = 0$ and $\hat{\mathbf{e}}_O \cdot \hat{\mathbf{e}}^*_X = 0$. We contract equation (3.9) with $\hat{\mathbf{e}}^*_O$ and $\hat{\mathbf{e}}^*_X$ in turn, finding

$$\alpha_O = \hat{\mathbf{e}}_{ant} \cdot \hat{\mathbf{e}}_{O,ant}, \tag{3.10}$$

and

$$\alpha_X = \hat{\mathbf{e}}_{ant} \cdot \hat{\mathbf{e}}_{X,ant}. \tag{3.11}$$

Having found the coefficients for the O and X modes, we now explicitly have an expression for $\mathbf{E}^{(+)}$.

We proceed by evaluating the integral on the left side of equation (3.6) over a surface which both contains the antenna and is far enough from the plasma that we can write $\mathbf{E}_s$ as a summation of plane waves,

$$\mathbf{E}_s = \sum_{\mathbf{K}_s} \mathbf{A}_s \exp(\mathrm{i}\mathbf{K}_s \cdot \mathbf{r}), \tag{3.12}$$

which we can do because the antenna is typically situated away from the plasma. Due to the vacuum dispersion relation, the scattered microwaves at the antenna have almost the same wavenumber as that emitted, Ω/c, at the antenna. The integrand of the surface integral in equation (3.6) is

$$\begin{aligned}
&(\nabla \times \mathbf{E}_s) \times \mathbf{E}^{(+)} + \mathbf{E}_s \times (\nabla \times \mathbf{E}^{(+)}) \\
&\quad \simeq \sum_{\mathbf{K}_s} \left[\mathrm{i}(\mathbf{K}_s \cdot \mathbf{E}^{(+)})\mathbf{A}_s - \mathrm{i}(\mathbf{A}_s \cdot \mathbf{E}^{(+)})\mathbf{K}_s\right] \exp(\mathrm{i}\mathbf{K}_s \cdot \mathbf{r}) \\
&\quad + \sum_{\mathbf{K}_s} \left[\mathrm{i}(\mathbf{A}_s \cdot \mathbf{E}^{(+)})\mathbf{K} - \mathrm{i}(\mathbf{K} \cdot \mathbf{A}_s)\mathbf{E}^{(+)}\right] \exp(\mathrm{i}\mathbf{K}_s \cdot \mathbf{r}),
\end{aligned} \tag{3.13}$$

where we have used $\nabla \mathbf{E}^{(+)} \simeq \mathrm{i}\mathbf{K}\mathbf{E}^{(+)}$. At the antenna, $\mathbf{K}$ is normal to the surface, and as a result its electric field is parallel to the surface. Moreover, at the antenna, $\mathbf{E}^{(+)} \propto \exp(\mathrm{i}K_g \hat{\mathbf{g}} \cdot \mathbf{r})$, and any term that contains an $\mathbf{A}_s$ with $\mathbf{K}_s$ not exactly perpendicular to the surface of the antenna integrates to zero. Therefore, $\int \sum_{\mathbf{K}_s} (\mathbf{K}_s \cdot \mathbf{E}^{(+)})[\mathbf{A}_s \exp(\mathrm{i}\mathbf{K}_s \cdot \mathbf{r})] \cdot \mathrm{d}\mathbf{S} = 0$. Similarly, $\int (\mathbf{K} \cdot \mathbf{E}_s)\mathbf{E}^{(+)} \cdot \mathrm{d}\mathbf{S} = 0$. The scattered waves are always travelling out of the plasma; the probe beam is also travelling out of the plasma at all points, except at the antenna. Consequently, the terms that contain $\mathbf{A}_s \cdot \mathbf{E}^{(+)}$ cancel at all points other than on the antenna. The surface integral in equation (3.6) is thus

$$\begin{aligned}
\int [(\nabla \times \mathbf{E}_s) \times \mathbf{E}^{(+)} + \mathbf{E}_s \times (\nabla \times \mathbf{E}^{(+)})] \cdot \mathrm{d}\mathbf{S} &= -\int_{ant} 2\mathrm{i}\frac{\Omega}{c} \mathbf{E}_s \cdot \mathbf{E}^{(+)} \mathrm{d}S \\
&= -2\mathrm{i}\frac{\Omega}{c} A_r.
\end{aligned} \tag{3.14}$$

Here we have used the fact that the wavenumbers are Ω/c since the antenna is in vacuum. Hence, we get the reciprocity relation

$$A_r = \frac{\Omega \mathrm{i}}{2c} \int \mathbf{E}^{(+)} \cdot \boldsymbol{\epsilon}_{tb} \cdot \mathbf{E}_b \, \mathrm{d}V. \tag{3.15}$$

Before we conclude this section, we first show that this equation can be further simplified. We use the microwave and reciprocal electric fields, as well as the linearised dielectric tensor, in the reciprocity theorem. Substituting equations (1.3), (2.110), (3.8), (3.10), and (3.11) into the volume integral of the reciprocity theorem, equation (3.15), we get

$$\begin{aligned} A_r = \frac{\mathrm{i}\Omega A_{ant}}{2\pi c} \int \sum_{i=O,X} \hat{\mathbf{e}}_{ant} \cdot \hat{\mathbf{e}}_{i,ant} \left\{ \det \left[\mathrm{Im} \left(\boldsymbol{\Psi}_{w,i} \right) \right] \right\}^{\frac{1}{4}} \left(\frac{g_{ant}}{g_i} \right)^{\frac{1}{2}} \\ \times \exp(\mathrm{i}\phi_{G,i} - \mathrm{i}\phi_{P,i}) \exp \left(\mathrm{i}s_i + \mathrm{i}\mathbf{K}_{w,i} \cdot \mathbf{w}_i + \frac{\mathrm{i}}{2} \mathbf{w}_i \cdot \boldsymbol{\Psi}_{w,i} \cdot \mathbf{w}_i \right) \\ \times \frac{\delta n_e}{n_e} \hat{\mathbf{e}}_i^* \cdot (\boldsymbol{\epsilon}_{eq} - \mathbf{1}) \cdot \hat{\mathbf{e}} \ \exp(\mathrm{i}\phi_G + \mathrm{i}\phi_P) \left\{ \det \left[\mathrm{Im} \left(\boldsymbol{\Psi}_w \right) \right] \right\}^{\frac{1}{4}} \left(\frac{g_{ant}}{g} \right)^{\frac{1}{2}} \\ \times \exp \left(\mathrm{i}s + \mathrm{i}\mathbf{K}_w \cdot \mathbf{w} + \frac{\mathrm{i}}{2} \mathbf{w} \cdot \boldsymbol{\Psi}_w \cdot \mathbf{w} \right) \ \mathrm{d}V. \end{aligned} \tag{3.16}$$

To simplify this expression and thus the subsequent algebra, we first make an argument about the contribution of the reciprocal electric field to the backscattered amplitude.

In general, the O and X modes take different paths through the plasma, even if they enter the plasma at the same point. For a given polarisation of the probe beam $\mathbf{E}_b$, the reciprocal beam with the same polarisation will follow the same path as the probe beam, and the reciprocal beam with the opposite polarisation follows a different path. As a result, the reciprocal beam with the same polarisation as the probe beam overlaps with the probe beam over a volume of order $W^2 L$, whereas the reciprocal beam with the opposite polarisation in general overlaps only over a small volume W^3. Since the contribution to the integral from the reciprocal beam with the opposite polarisation to the probe beam is small by $W/L \ll 1$, equation (3.16) simplifies to

$$\begin{aligned} A_r = \frac{\mathrm{i}\Omega A_{ant}}{2\pi c} \hat{\mathbf{e}}_{ant} \cdot \hat{\mathbf{e}}_{ant} \int \left[\det[\mathrm{Im}(\boldsymbol{\Psi}_w)] \right]^{\frac{1}{2}} \frac{g_{ant}}{g} \exp(2\mathrm{i}\phi_G) \\ \times \frac{\delta n_e}{n_e} \hat{\mathbf{e}}^* \cdot (\boldsymbol{\epsilon}_{eq} - \mathbf{1}) \cdot \hat{\mathbf{e}} \ \exp(2\mathrm{i}s + 2\mathrm{i}\mathbf{K}_w \cdot \mathbf{w} + \mathrm{i}\mathbf{w} \cdot \boldsymbol{\Psi}_w \cdot \mathbf{w}) \, \mathrm{d}V. \end{aligned} \tag{3.17}$$

This is the form the of backscattered amplitude that we subsequently use.

Chapter 4

Backscattered electric field

4.1 Assumptions about turbulent fluctuations

We see that we need to evaluate the three spatial integrals in equation (3.17) to determine the backscattered signal. In order to do this, we need to make some assumptions about the nature of the turbulent fluctuations δn_e.

In this work, we take the plasma to be in steady state, such that the equilibrium electron density n_e has no time dependence, whereas we assume that the turbulent fluctuations δn_e can indeed have a fast time dependence t in addition to a spatial dependence. This time-dependence will be important in Section 5.1.1. For now, we will concentrate on the spatial properties δn_e.

We consider a tubular region of space around the Gaussian beam as it propagates through the plasma. This region of space is elongated along the ray, and across the ray it is several times the width of the Gaussian beam, such that the beam's electric field is effectively zero on the boundary of this region. We Fourier analyse δn_e in this volume. We use the usual assumptions for turbulent fluctuations [28, 29], considering electron density fluctuations δn_e with very large gradients across the magnetic field and small gradients along it. Hence, we define coordinates aligned with the magnetic field. We use $u_\parallel$, the arc length along magnetic field lines, and two variables u_1 and u_2 that both satisfy

$$\hat{\mathbf{b}}(\mathbf{q}(\tau) + \mathbf{w}) \cdot \nabla u_i = 0. \tag{4.1}$$

With these variables, we get

$$\delta n_e(\mathbf{r},t) = \int \delta\tilde{n}_e(k_{\perp,1},k_{\perp,2},u_\parallel,\omega)\exp\left(\mathrm{i}k_{\perp,1}u_1+\mathrm{i}k_{\perp,2}u_2-\mathrm{i}\omega t\right)\mathrm{d}k_{\perp,1}\ \mathrm{d}k_{\perp,2}\ \mathrm{d}\omega, \quad (4.2)$$

where ω has contributions from both the angular frequency of the turbulence in the plasma's frame and the Doppler shift due to the plasma flow, and

$$k_{\perp,\alpha} \sim \frac{1}{\lambda} \gg k_\parallel \sim \frac{1}{L} \sim \frac{\partial}{\partial u_\parallel} \quad (4.3)$$

are the components of the turbulence wavevector perpendicular to the magnetic field. We remind readers $u_\parallel$ is the arc length along magnetic field lines, and we now define u_1 and u_2 such that their gradients are perpendicular to each other at $\mathbf{w}=0$ (on the central ray). They are only perpendicular to each other along the central ray, and not when we move away from it; this is a consequence of magnetic shear. Any vector perpendicular to the magnetic field is resolved into two directions: $\hat{\mathbf{u}}_1 = \nabla u_1(\mathbf{w}=\mathbf{0})$ and $\hat{\mathbf{u}}_2 = \nabla u_2(\mathbf{w}=\mathbf{0})$. The subscripts $_1$ and $_2$ indicate projection on these directions respectively. We choose $\hat{\mathbf{u}}_1$ and $\hat{\mathbf{u}}_2$ as follows: $\hat{\mathbf{u}}_1$ is in the plane of $\hat{\mathbf{g}}$ and $\hat{\mathbf{b}}$, while $\hat{\mathbf{u}}_2$ is perpendicular to $\hat{\mathbf{g}}$, and both of them are perpendicular to $\hat{\mathbf{b}}$,

$$\hat{\mathbf{u}}_1 = \frac{(\hat{\mathbf{b}}\times\hat{\mathbf{g}})\times\hat{\mathbf{b}}}{|(\hat{\mathbf{b}}\times\hat{\mathbf{g}})\times\hat{\mathbf{b}}|}, \quad (4.4)$$

and

$$\hat{\mathbf{u}}_2 = \frac{\hat{\mathbf{b}}\times\hat{\mathbf{g}}}{|\hat{\mathbf{b}}\times\hat{\mathbf{g}}|}. \quad (4.5)$$

Here we take $\hat{\mathbf{b}}$ to be a shorthand for $\hat{\mathbf{b}}(\mathbf{q}(\tau)) = \hat{\mathbf{b}}(\tau)$. That is, $\hat{\mathbf{b}}$ is the unit vector of the magnetic field on the central ray. Note that if $\hat{\mathbf{g}}$ and $\hat{\mathbf{b}}$ are perpendicular to each other (that is, if there is no mismatch, as we later show), $\hat{\mathbf{u}}_1 = \hat{\mathbf{g}}$ (Figure 4.1). Note that this $\hat{\mathbf{u}}_1$ and $\hat{\mathbf{u}}_2$ are the same as that used in Section 2.2.1, as we will prove in equation (4.34). We align the basis for $\mathbf{w}$, see equation (2.3), with the basis for $\mathbf{k}_\perp$. We choose $\hat{\mathbf{y}} = \hat{\mathbf{u}}_2$ and denote projection in that direction with the subscript $_y$. The other basis vector for $\mathbf{w}$, which is perpendicular to both $\hat{\mathbf{g}}$ and $\hat{\mathbf{y}}$, will be

$$\hat{\mathbf{x}} = \frac{\hat{\mathbf{y}}\times\hat{\mathbf{g}}}{|\hat{\mathbf{y}}\times\hat{\mathbf{g}}|} = \frac{\hat{\mathbf{u}}_2\times\hat{\mathbf{g}}}{|\hat{\mathbf{u}}_2\times\hat{\mathbf{g}}|}. \quad (4.6)$$

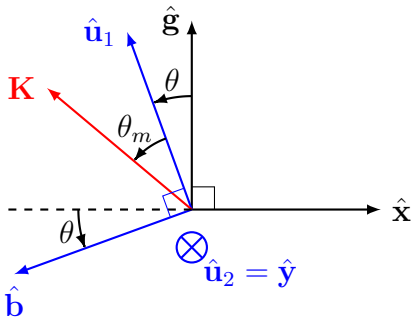

Figure 4.1: Bases for $\mathbf{k}_\perp$ and $\mathbf{w}$, with $\theta > 0$ and $\theta_m > 0$.

Based on the bases for $\mathbf{k}_\perp$ and $\mathbf{w}$, we define the angle θ such that

$$\cos\theta = \hat{\mathbf{g}} \cdot \hat{\mathbf{u}}_1, \tag{4.7}$$

and

$$\hat{\mathbf{x}} \cdot \hat{\mathbf{u}}_1 = -\sin\theta. \tag{4.8}$$

This angle θ is not the mismatch angle, but is of the same order as the mismatch angle, as we will later prove. The mismatch angle is

$$\sin\theta_m = \hat{\mathbf{K}} \cdot \hat{\mathbf{b}}, \tag{4.9}$$

which we take to be small,

$$\theta_m \sim \frac{\lambda}{W}, \tag{4.10}$$

in order to obtain a significant signal. This will be shown to be self-consistent at the end of our derivation.

Using the definitions of $\hat{\mathbf{u}}_1 = \nabla u_1(\mathbf{w} = \mathbf{0})$ and $\hat{\mathbf{u}}_2 = \nabla u_2(\mathbf{w} = \mathbf{0})$ above, we derive the coordinates u_1 and u_2 in Appendix C. We summarise the results here. They are

$$\begin{aligned} u_1 = &\int_0^\tau g(\tau')\cos\theta(\tau')\,\mathrm{d}\tau - w_x\sin\theta \\ &+ \frac{w_x^2}{2}\left(\frac{\sin\theta}{g}\frac{\mathrm{d}\theta}{\mathrm{d}\tau} - \boldsymbol{\kappa}\cdot\hat{\mathbf{x}}\sin\theta + \hat{\mathbf{x}}\cdot\nabla\hat{\mathbf{b}}\cdot\hat{\mathbf{g}} - \hat{\mathbf{x}}\cdot\nabla\hat{\mathbf{b}}\cdot\hat{\mathbf{x}}\tan\theta\right) \\ &+ w_x w_y\left(-\boldsymbol{\kappa}\cdot\hat{\mathbf{y}}\sin\theta + \hat{\mathbf{y}}\cdot\nabla\hat{\mathbf{b}}\cdot\hat{\mathbf{g}} + \frac{\sin\theta\tan\theta}{g}\frac{\mathrm{d}\hat{\mathbf{x}}}{\mathrm{d}\tau}\cdot\hat{\mathbf{y}} - \hat{\mathbf{y}}\cdot\nabla\hat{\mathbf{b}}\cdot\hat{\mathbf{x}}\tan\theta\right), \end{aligned} \tag{4.11}$$

and

$$u_2 = w_y + \frac{w_x^2}{2}\left(\frac{\tan\theta}{g}\frac{\mathrm{d}\hat{\mathbf{x}}}{\mathrm{d}\tau}\cdot\hat{\mathbf{y}} + \frac{\hat{\mathbf{x}}\cdot\nabla\hat{\mathbf{b}}\cdot\hat{\mathbf{y}}}{\cos\theta}\right) + w_x w_y\frac{\hat{\mathbf{y}}\cdot\nabla\hat{\mathbf{b}}\cdot\hat{\mathbf{y}}}{\cos\theta}. \tag{4.12}$$

Here,

$$\boldsymbol{\kappa} = \frac{1}{g}\frac{\mathrm{d}\hat{\mathbf{g}}}{\mathrm{d}\tau} \tag{4.13}$$

is the curvature of the central ray. This ray curvature should not be confused with the wavefront curvature, $1/R_b$. Note that we have kept corrections to u_1 and u_2 to order λ. Finally, the arc length along the magnetic field is

$$u_\parallel \simeq -\int_0^\tau g(\tau')\sin\theta(\tau')\mathrm{d}\tau' - w_x\cos\theta, \tag{4.14}$$

where we have neglected terms that are small in W/L. Since $k_\parallel \sim 1/L$, we have $k_\parallel u_\parallel \sim 1$, and the higher order contributions to $u_\parallel$ are not required.

4.2 Backscattered electric field: general

We proceed to evaluate the amplitude of the backscattered electric field, A_r. Writing the volume element in equation (3.17) as

$$\mathrm{d}V = g\ \mathrm{d}w_x\ \mathrm{d}w_y\ \mathrm{d}\tau, \tag{4.15}$$

and substituting equations (4.2), (4.11), and (4.12) into equation (3.17), we get

$$\begin{aligned} A_r = {} & \frac{\mathrm{i}\Omega A_{ant} g_{ant} \hat{\mathbf{e}}_{ant}\cdot\hat{\mathbf{e}}_{ant}}{2\pi c}\int [\det[\mathrm{Im}(\boldsymbol{\Psi}_w)]]^{\frac{1}{2}}\exp(2\mathrm{i}\phi_G)\exp\left(-\mathrm{i}\omega t\right) \\ & \times \frac{\delta\tilde{n}_e}{n_e}\ \hat{\mathbf{e}}^*\cdot(\boldsymbol{\epsilon}_{eq}-\mathbf{1})\cdot\hat{\mathbf{e}}\ \exp\left(2\mathrm{i}s + \mathrm{i}k_{\perp,1}\int_0^\tau g(\tau')\cos\theta(\tau')\ \mathrm{d}\tau'\right) \\ & \times \exp\left[\mathrm{i}(2\mathbf{K}_w + \mathbf{k}_{\perp,w})\cdot\mathbf{w} + \mathrm{i}\mathbf{w}\cdot\boldsymbol{M}_w\cdot\mathbf{w}\right]\ \mathrm{d}w_x\ \mathrm{d}w_y\ \mathrm{d}\tau\ \mathrm{d}k_{\perp,1}\ \mathrm{d}k_{\perp,2}\ \mathrm{d}\omega. \end{aligned} \tag{4.16}$$

Here $\mathbf{k}_\perp = k_{\perp,1}\hat{\mathbf{u}}_1 + k_{\perp,2}\hat{\mathbf{u}}_2$ and $\boldsymbol{M}_w$ is the symmetric modified $\boldsymbol{\Psi}_w$ matrix, given by

$$\boldsymbol{M}_w = \begin{pmatrix} M_{xx} & M_{xy} & 0 \\ M_{xy} & M_{yy} & 0 \\ 0 & 0 & 0 \end{pmatrix}, \tag{4.17}$$

where

$$\begin{aligned} M_{xx} = {} & \Psi_{xx} + \frac{k_{\perp,1}}{2}\left(\frac{\sin\theta}{g}\frac{\mathrm{d}\theta}{\mathrm{d}\tau} - \boldsymbol{\kappa}\cdot\hat{\mathbf{x}}\sin\theta + \hat{\mathbf{x}}\cdot\nabla\hat{\mathbf{b}}\cdot\hat{\mathbf{g}} - \hat{\mathbf{x}}\cdot\nabla\hat{\mathbf{b}}\cdot\hat{\mathbf{x}}\tan\theta\right) \\ & + \frac{k_{\perp,2}}{2}\left(\frac{\tan\theta}{g}\frac{\mathrm{d}\hat{\mathbf{x}}}{\mathrm{d}\tau}\cdot\hat{\mathbf{y}} + \frac{\hat{\mathbf{x}}\cdot\nabla\hat{\mathbf{b}}\cdot\hat{\mathbf{y}}}{\cos\theta}\right), \end{aligned} \tag{4.18}$$

$$M_{xy} = \Psi_{xy} + \frac{k_{\perp,1}}{2}\left(-\boldsymbol{\kappa}\cdot\hat{\mathbf{y}}\sin\theta + \hat{\mathbf{y}}\cdot\nabla\hat{\mathbf{b}}\cdot\hat{\mathbf{g}} + \frac{\sin\theta\tan\theta}{g}\frac{\mathrm{d}\hat{\mathbf{x}}}{\mathrm{d}\tau}\cdot\hat{\mathbf{y}} - \hat{\mathbf{y}}\cdot\nabla\hat{\mathbf{b}}\cdot\hat{\mathbf{x}}\tan\theta\right) + \frac{k_{\perp,2}}{2}\frac{\hat{\mathbf{y}}\cdot\nabla\hat{\mathbf{b}}\cdot\hat{\mathbf{y}}}{\cos\theta}, \tag{4.19}$$

and

$$M_{yy} = \Psi_{yy}. \tag{4.20}$$

It is worth noting a few points about this modified matrix. First, the modifications to $\boldsymbol{\Psi}_w$ are only to its real part, that is, the part associated with curvature (as opposed to width). Secondly, that these modifications depend on the curvature of the magnetic field and the magnetic shear, not on the curvature of the cut-off surface. As we will see in Chapter 7, this affects the wavenumber resolution, and our model gives a different result from widely-cited earlier work [3, 25]. In Scotty, we calculate the gradients of $\hat{\mathbf{b}}$ in cylindrical coordinates,

$$\nabla\hat{\mathbf{b}} = \frac{\partial b_R}{\partial R}\hat{\mathbf{R}}\hat{\mathbf{R}} + \frac{\partial b_R}{\partial Z}\hat{\mathbf{Z}}\hat{\mathbf{R}} + b_R\frac{\hat{\boldsymbol{\zeta}}\hat{\boldsymbol{\zeta}}}{R} + \frac{\partial b_Z}{\partial R}\hat{\mathbf{R}}\hat{\mathbf{Z}} + \frac{\partial b_Z}{\partial Z}\hat{\mathbf{Z}}\hat{\mathbf{Z}} + \frac{\partial b_\zeta}{\partial R}\hat{\mathbf{R}}\hat{\boldsymbol{\zeta}} + \frac{\partial b_\zeta}{\partial Z}\hat{\mathbf{Z}}\hat{\boldsymbol{\zeta}} - b_\zeta\frac{\hat{\boldsymbol{\zeta}}\hat{\mathbf{R}}}{R}. \tag{4.21}$$

To get this result, one should remember that the $\hat{\mathbf{R}}$ and $\hat{\boldsymbol{\zeta}}$ basis vectors depend on position. That is, we have used

$$\nabla\hat{\mathbf{R}} = \frac{\hat{\boldsymbol{\zeta}}\hat{\boldsymbol{\zeta}}}{R}, \tag{4.22}$$

and

$$\nabla\hat{\boldsymbol{\zeta}} = -\frac{\hat{\boldsymbol{\zeta}}\hat{\mathbf{R}}}{R}. \tag{4.23}$$

What the DBS community actually uses is not $A_r(t)$ directly, but its Fourier transform $\tilde{A}_r(\omega) = (2\pi)^{-1}\int A_r(t)\exp(\mathrm{i}\omega t)\,\mathrm{d}t$, which is

$$\tilde{A}_r(\omega) = \frac{\mathrm{i}\Omega A_{ant} g_{ant}\hat{\mathbf{e}}_{ant}\cdot\hat{\mathbf{e}}_{ant}}{2\pi c}\int[\det[\mathrm{Im}(\boldsymbol{\Psi}_w)]]^{\frac{1}{2}}\exp(2\mathrm{i}\phi_G) \times\frac{\delta\tilde{n}_e}{n_e}\,\hat{\mathbf{e}}^*\cdot(\boldsymbol{\epsilon}_{eq}-\mathbf{1})\cdot\hat{\mathbf{e}}\,\exp\left(2\mathrm{i}s + \mathrm{i}k_{\perp,1}\int_0^\tau g(\tau')\cos\theta(\tau')\,\mathrm{d}\tau'\right) \times\exp\left[\mathrm{i}(2\mathbf{K}_w+\mathbf{k}_{\perp,w})\cdot\mathbf{w} + \mathrm{i}\mathbf{w}\cdot\boldsymbol{M}_w\cdot\mathbf{w}\right]\,\mathrm{d}w_x\,\mathrm{d}w_y\,\mathrm{d}\tau\,\mathrm{d}k_{\perp,1}\,\mathrm{d}k_{\perp,2}. \tag{4.24}$$

The task ahead of us is to solve the integrals in equation (4.24). We begin by evaluating the Gaussian integrals in $\mathbf{w}$ (Section 4.2.1). When calculating Gaussian integrals with

complex coefficients, we need to be careful — see Appendix B. To solve the integral in τ, we have to make some assumptions about θ, which we do in section 4.2.2. Depending on the assumptions made, we can solve the integral in the *conventional tokamak* (section 4.3) or *spherical tokamak* (section 4.4) cases. Looking forward, we later show that the backscattered powers in both cases coincide in the right limits, Section 5.2.

4.2.1 Gaussian integrals in w_x and w_y

To solve the spatial integrals perpendicular to the beam, we first define the inverse of $\boldsymbol{M}_w$ as

$$\boldsymbol{M}_w^{-1} = \begin{pmatrix} M_{xx}^{-1} & M_{xy}^{-1} & 0 \\ M_{yx}^{-1} & M_{yy}^{-1} & 0 \\ 0 & 0 & 0 \end{pmatrix} = \begin{pmatrix} \begin{pmatrix} M_{xx} & M_{xy} \\ M_{yx} & M_{yy} \end{pmatrix}^{-1} & \begin{matrix} 0 \\ 0 \end{matrix} \\ \begin{matrix} 0 & 0 \end{matrix} & 0 \end{pmatrix}. \tag{4.25}$$

It is important to bear in mind that M_{ij}^{-1} is the ij component of $\boldsymbol{M}_w^{-1}$, and not $1/M_{ij}$. We then note that

$$\begin{aligned} &(2\mathbf{K}_w + \mathbf{k}_{\perp,w}) \cdot \mathbf{w} + \mathbf{w} \cdot \boldsymbol{M}_w \cdot \mathbf{w} \\ &\quad = \left[\mathbf{w} + \frac{1}{2}(2\mathbf{K}_w + \mathbf{k}_{\perp,w}) \cdot \boldsymbol{M}_w^{-1}\right] \cdot \boldsymbol{M}_w \cdot \left[\mathbf{w} + \frac{1}{2}\boldsymbol{M}_w^{-1} \cdot (2\mathbf{K}_w + \mathbf{k}_{\perp,w})\right] \\ &\quad - \frac{1}{4}(2\mathbf{K}_w + \mathbf{k}_{\perp,w}) \cdot \boldsymbol{M}_w^{-1} \cdot (2\mathbf{K}_w + \mathbf{k}_{\perp,w}). \end{aligned} \tag{4.26}$$

We substitute this expression into equation (4.16). Note that the integral over w_y in equation (4.24) is a Gaussian integral. However, the integral over w_x in equation (4.24) is not strictly a Gaussian integral because of the dependence on $u_\parallel$ on w_x; this dependence is negligible because the turbulent properties change slowly along a field line, allowing us to treat this integral as Gaussian as well. In Appendix B.2, we show how to calculate a 2D complex Gaussian integral. The turbulent fluctuations are evaluated at

$$\delta\tilde{n}_e\left(k_{\perp,1}, k_{\perp,2}, u_\parallel, \omega\right) \simeq \delta\tilde{n}_e\left(k_{\perp,1}, k_{\perp,2}, -\int_0^\tau g(\tau')\sin\theta(\tau')\,\mathrm{d}\tau', \omega\right), \tag{4.27}$$

and equation (4.24) thus becomes

$$\begin{aligned}\tilde{A}_r = &-\frac{\Omega A_{ant} g_{ant} \hat{\mathbf{e}}_{ant} \cdot \hat{\mathbf{e}}_{ant}}{2c} \int \left[\frac{\det\left[\mathrm{Im}\left(\boldsymbol{\Psi}_w\right)\right]}{\det\left(\boldsymbol{M}_w\right)}\right]^{\frac{1}{2}} \exp(2\mathrm{i}\phi_G) \\ &\times \frac{\delta\tilde{n}_e}{n_e}\ \hat{\mathbf{e}}^* \cdot (\boldsymbol{\epsilon}_{eq} - \mathbf{1}) \cdot \hat{\mathbf{e}}\ \exp\left(2\mathrm{i}s + \mathrm{i}k_{\perp,1} \int_0^\tau g(\tau') \cos\theta(\tau')\ \mathrm{d}\tau'\right) \\ &\times \exp\left[-\frac{\mathrm{i}}{4}(2\mathbf{K}_w + \mathbf{k}_{\perp,w}) \cdot \boldsymbol{M}_w^{-1} \cdot (2\mathbf{K}_w + \mathbf{k}_{\perp,w})\right]\ \mathrm{d}\tau\ \mathrm{d}k_{\perp,1}\ \mathrm{d}k_{\perp,2}. \end{aligned} \tag{4.28}$$

We note that the phase of $\sqrt{\det\left(\boldsymbol{M}_w\right)}$ is chosen from

$$\sqrt{\det\left(\boldsymbol{M}_w\right)} = \sqrt{M_{xx}} \sqrt{\frac{\det\left(\boldsymbol{M}_w\right)}{M_{xx}}}, \tag{4.29}$$

and the fact that these square roots must have

$$\mathrm{Im}\left(\sqrt{M_{xx}}\right) > 0, \tag{4.30}$$

and

$$\mathrm{Im}\left[\sqrt{\frac{\det\left(\boldsymbol{M}_w\right)}{M_{xx}}}\right] > 0. \tag{4.31}$$

A convenient way to remember this rule is to consider a purely imaginary $\boldsymbol{M}_w$, in which case this result is the most intuitive and sensible one. Refer to Appendix B.2 for a more detailed explanation of the underlying reasoning.

To simplify equation (4.28), we project $\mathbf{K}_w$ onto $\hat{\mathbf{x}}$ and $\hat{\mathbf{y}}$. Note that the dispersion relation for cold plasma depends on $\mathbf{K}$ only via K^2 and $(\mathbf{K} \cdot \hat{\mathbf{b}})^2$,

$$H(\mathbf{K}, \mathbf{q}) = H(K^2, (\mathbf{K} \cdot \hat{\mathbf{b}})^2, \mathbf{q}). \tag{4.32}$$

Thus, we find that

$$\mathbf{g} = \nabla_K H = 2\frac{\partial H}{\partial K^2}\mathbf{K} + 2K \sin\theta_m \frac{\partial H}{\partial (\mathbf{K} \cdot \hat{\mathbf{b}})^2}\hat{\mathbf{b}}. \tag{4.33}$$

and as a consequence

$$K_y = 0. \tag{4.34}$$

That is, the beam wavevector $\mathbf{K}$ is always in the plane defined by $\hat{\mathbf{b}}$ and $\hat{\mathbf{g}}$. Using these insights, we remark that there is an exponential decay of the signal with $k_{\perp,2}$ because

of the piece

$$\exp\left[-\frac{\mathrm{i}}{4}(2\mathbf{K}_w+\mathbf{k}_{\perp,w})\cdot\boldsymbol{M}_w^{-1}\cdot(2\mathbf{K}_w+\mathbf{k}_{\perp,w})\right]$$
$$=\exp\left[-\frac{\mathrm{i}}{4}\left((2K_x-k_{\perp,1}\sin\theta)^2M_{xx}^{-1}+2k_{\perp,2}(2K_x-k_{\perp,1}\sin\theta)M_{xy}^{-1}+k_{\perp,2}^2M_{yy}^{-1}\right)\right]. \tag{4.35}$$

Hence, $k_{\perp,2}$ cannot be of order $1/\lambda$, otherwise the argument of the exponential will be large and there will be no signal. Instead, by requiring that this argument can at most be of order unity, we find that

$$k_{\perp,2}\sim\frac{1}{W}. \tag{4.36}$$

4.2.2 Ordering θ_m: the conventional and spherical cases

We consider two cases: the *conventional tokamak* and the *spherical tokamak*. These are simply names for two different cases typical of but not exclusive to conventional and spherical tokamaks, respectively. Moreover, these orderings are not only applicable to tokamaks. As long as the orderings in either case hold, the results will be applicable. In particular, they are applicable to stellarators.

In the *conventional tokamak* case, we take the mismatch angle to be small for the entire length of the beam path,

$$\theta_m\sim\frac{\lambda}{W}. \tag{4.37}$$

In this situation, the backscattered signal is given by the Bragg condition, which we discuss in more detail in Section 4.3.

In the *spherical tokamak* case, we take the mismatch angle to be of order unity $\theta_m\sim 1$. In general, this requires more work and is beyond the scope of this thesis. However, in the special scenario where there is no mismatch ($\theta_m=0$) on at least one point along the beam path, the backscattered signal is dominated by this point. We derive the backscattered signal for this particular case in Section 4.4. In the right limits, we show that the *spherical tokamak* and *conventional tokamak* cases coincide.

4.3 Conventional tokamak

In this section, we solve the integral in τ for the *conventional tokamak* case, while the *spherical tokamak* case will be handled in Section 4.4. We begin by exploring in detail the orderings involved in the former case. Once we do this, we then proceed to evaluate the integral in τ via the method of stationary phase.

4.3.1 Ordering

We contract equation (4.33) with $\hat{\mathbf{b}}$, giving us

$$-g\sin\theta = 2K\left(\frac{\partial H}{\partial K^2} + \frac{\partial H}{\partial(\mathbf{K}\cdot\hat{\mathbf{b}})^2}\right)\sin\theta_m. \tag{4.38}$$

When $\theta_m \sim \lambda/W$, equation (4.33) gives us $g \simeq 2K\ \partial H/\partial K^2$ to leading order. Hence we find that

$$\sin\theta = -\left[1 + \frac{\partial H}{\partial(\mathbf{K}\cdot\hat{\mathbf{b}})^2}\left(\frac{\partial H}{\partial K^2}\right)^{-1}\right]\sin\theta_m. \tag{4.39}$$

The finer details of the relationship between θ and θ_m are discussed in Appendix D. However, to proceed, all we need is to note that since

$$\frac{\partial H}{\partial(\mathbf{K}\cdot\hat{\mathbf{b}})^2} \sim \frac{\partial H}{\partial K^2}, \tag{4.40}$$

we get

$$\theta \sim \theta_m \sim \frac{\lambda}{W}. \tag{4.41}$$

Consequently, we have

$$K_x = -K\sin(\theta_m + \theta) \simeq -K(\theta_m + \theta) \sim \frac{1}{W}. \tag{4.42}$$

Hence, K_x/K is small in mismatch angle, whereas

$$K_g = K\cos(\theta + \theta_m) \simeq K. \tag{4.43}$$

From equations (4.34) and (4.42), we find that $K_w/K = K_x/K \sim \theta_m$. At this point, we see that our ordering $\theta_m \sim \lambda/W$ is necessary for the mismatch angle to be small enough to allow for a backscattered signal to be detected. Indeed, using equations

(4.41) and (4.42), the M_{xx}^{-1} and M_{xy}^{-1} terms in the exponential of equation (4.35) are of order unity.

In a conventional tokamak, most of the magnetic field is in the toroidal direction $\hat{\mathbf{b}} \simeq \hat{\boldsymbol{\zeta}}$. Hence, to have $\theta \sim \lambda/W$, we require

$$\hat{\mathbf{g}} \cdot \hat{\boldsymbol{\zeta}} \sim \frac{\lambda}{W}. \tag{4.44}$$

Note that this is a maximal ordering. The consequence of this is that the group velocity of the probe beam can have a small toroidal component and the orderings will still hold, but everything still works perfectly fine if the group velocity is entirely in the poloidal plane. If this were the case, then the mismatch angle is simply the ratio of the poloidal magnetic field to the toroidal magnetic field, leading us to the conclusion that

$$\frac{B_p}{B} \sim \frac{\lambda}{W}. \tag{4.45}$$

In this situation, $\hat{\mathbf{e}}$ can be calculated exactly. In the basis of section 2.2.1, the polarisations of the O-mode and X mode are

$$\hat{\mathbf{e}}_O \propto \begin{pmatrix} 0 \\ 0 \\ 1 \end{pmatrix}, \tag{4.46}$$

and

$$\hat{\mathbf{e}}_x \propto \begin{pmatrix} \mathrm{i}\epsilon_{12} \\ \epsilon_{11} \\ 0 \end{pmatrix}. \tag{4.47}$$

Since we assume the antenna surface to be in vacuum, we take the limit $n_e \to 0$ to find the polarisation at the antenna. The polarisation is linear and hence $|\hat{\mathbf{e}}_{ant} \cdot \hat{\mathbf{e}}_{ant}| = 1$. Without loss of generality, we take $\hat{\mathbf{e}}_{ant}$ to be purely real, and in this case, $\hat{\mathbf{e}}_{ant} \cdot \hat{\mathbf{e}}_{ant} = 1$. If for purely perpendicular propagation, $\hat{\mathbf{e}}_{ant} \cdot \hat{\mathbf{e}}_{ant} = 1$, then for $\theta \sim \theta_m \ll 1$, it will be close to one.

In order to help develop better intuition of equation (4.42) and the various orderings, we launch various probe beams into high aspect ratio circular flux surface analytic equilibria with no Shafranov shift, described in Section 2.2.2. We fix the launch angles, and vary $B_{p,max}/B_{\zeta,max}$, thereby scaling $B_p/B_\zeta \sim B_p/B \sim \theta_m$ everywhere. We see from Figure 4.2 (left) that the magnitude of K_x scales accordingly, as expected. We

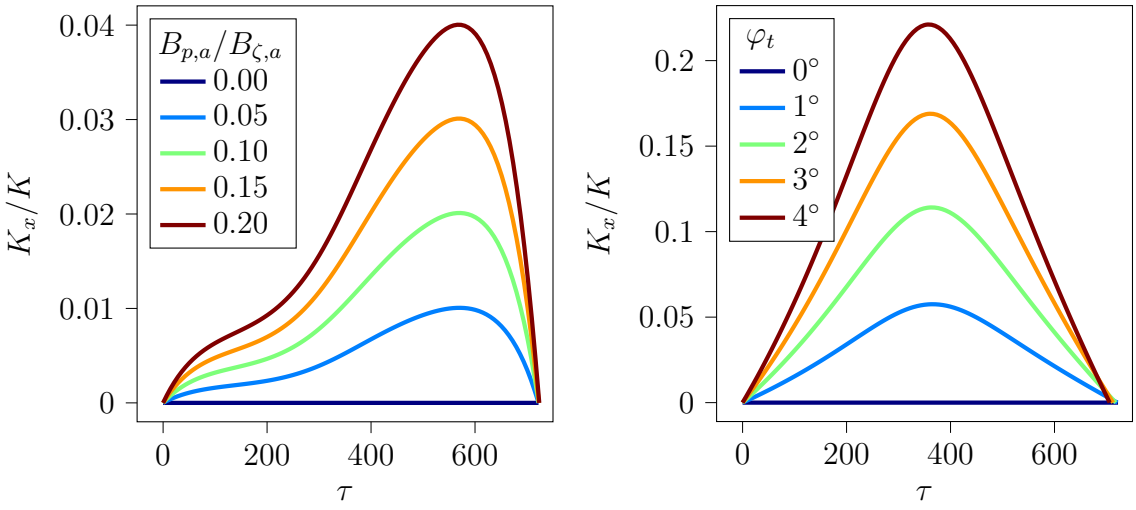

Figure 4.2: For a beam in the poloidal plane, increasing B_p/B increases the mismatch angle, which increases K_x/K (left). Increasing the toroidal launch angle also increases the mismatch angle, which increases K_x/K (right).

increase the toroidal launch angle for a plasma with $B_p = 0$, starting from a launch angle of 0, which corresponds to the beam being entirely in the poloidal plane. This also has the effect of increasing the mismatch angle, and we can see in Figure 4.2 (right) that K_x also increases.

4.3.2 Stationary phase integral in τ

We now proceed to evaluate the integral in τ in equation (4.28), exploiting the orderings above. Noticing that the function $\exp\left[2\mathrm{i}s + \mathrm{i}k_{\perp,1}\int_0^\tau g(\tau')\cos\theta(\tau')\,\mathrm{d}\tau'\right]$ oscillates quickly in τ since $2\mathrm{i}s + \mathrm{i}k_{\perp,1}\int_0^\tau g(\tau')\cos\theta(\tau')\,\mathrm{d}\tau' \sim L/\lambda \gg 1$, we use the method of stationary phase to evaluate the τ integral, an approach to DBS that is well-established [24]. The method works as follows. Since the exponential fluctuates quickly, the positive fluctuations cancel with the negative fluctuations, integrating to zero to lowest order. This does not happen where the phase is stationary, that is, when

$$\frac{\mathrm{d}}{\mathrm{d}\tau}\Big|_{\tau_\mu}\left[2s + k_{\perp,1}\int_0^\tau g(\tau')\cos\theta(\tau')\,\mathrm{d}\tau'\right] = 0, \tag{4.48}$$

where $\tau_\mu = \tau_a, \tau_b, \ldots$ are various points along the ray that satisfy this equation. Equation (4.48) is the Bragg condition alluded to in the introduction,

$$k_{\perp,1}\cos\theta(\tau_\mu) = -2K_g(\tau_\mu). \tag{4.49}$$

Neglecting terms that are small in mismatch, we get

$$k_{\perp,1} \simeq -2K(\tau_\mu), \tag{4.50}$$

which is how the Bragg condition is typically presented in the literature: at every point along the ray, there is a specific $k_{\perp,1}$ that is responsible for backscattering, and its value is determined solely by the wavenumber at that point. We consider the case where the density profile is monotonic. In such a situation, K decreases as we get close to the cut-off, and increases as we go further from it. Hence, for any given $k_{\perp,1}$, there are three possible scenarios, as shown in Figure 4.3. First, that $k_{\perp,1}$ is either too small or too large, such that at no point of the ray's trajectory is it responsible for backscattering. Second, that it backscatters the beam exactly once, at an extremum value of K along the path. Third, that the same $k_{\perp,1}$ is responsible for backscattering at two points along the path, $\tau_\mu = \tau_a$ and $\tau_\mu = \tau_b$; consequently, we have to add contributions from both these locations when taking the integral in τ. This can be extended to more complicated cases where the density profile is non-monotonic.

Since the dominant contributions to the integral are due to small intervals centred around $\tau_\mu = \tau_a, \tau_b, \ldots$, we Taylor expand the phase $2\mathrm{i}s + \mathrm{i}k_{\perp,1}\int_0^\tau g(\tau')\ \mathrm{d}\tau'$ around $\tau_a, \tau_b, \ldots$ to find these contributions. Usually, we will have at most two points to expand around (τ_a and τ_b), but we keep things general and sum over all of them, just in case one were to consider one of the aforementioned complicated cases. We first note that when the mismatch angle is small, $\theta_m \sim \lambda/W$, we have

$$\exp\left(\mathrm{i}k_{\perp,1}\int_0^\tau g(\tau')\cos\theta(\tau')\ \mathrm{d}\tau'\right) \simeq \exp\left(\mathrm{i}k_{\perp,1}\int_0^\tau g(\tau')\left(1-\frac{1}{2}\theta^2(\tau')\right)\ \mathrm{d}\tau'\right), \tag{4.51}$$

where we have discarded terms which are small. Hence, expanding the large phase term, we get

$$\begin{aligned}&\exp\left(2\mathrm{i}s + \mathrm{i}k_{\perp,1}\int_0^\tau g(\tau')\left(1-\frac{1}{2}\theta^2(\tau')\right)\ \mathrm{d}\tau'\right)\\ &\simeq \exp\left[2\mathrm{i}s(\tau_\mu) + \mathrm{i}k_{\perp,1}\int_0^{\tau_\mu} g(\tau')\left(1-\frac{1}{2}\theta^2(\tau')\right)\ \mathrm{d}\tau' + \mathrm{i}g(\tau_\mu)\frac{\mathrm{d}K}{\mathrm{d}\tau}\Big|_{\tau_\mu}(\tau-\tau_\mu)^2\right].\end{aligned} \tag{4.52}$$

Here the subscript $_\mu$ on functions of τ indicates these functions are evaluated at $\tau = \tau_\mu$. We have also used the Bragg condition, equation (4.50), to simplify some of the terms.

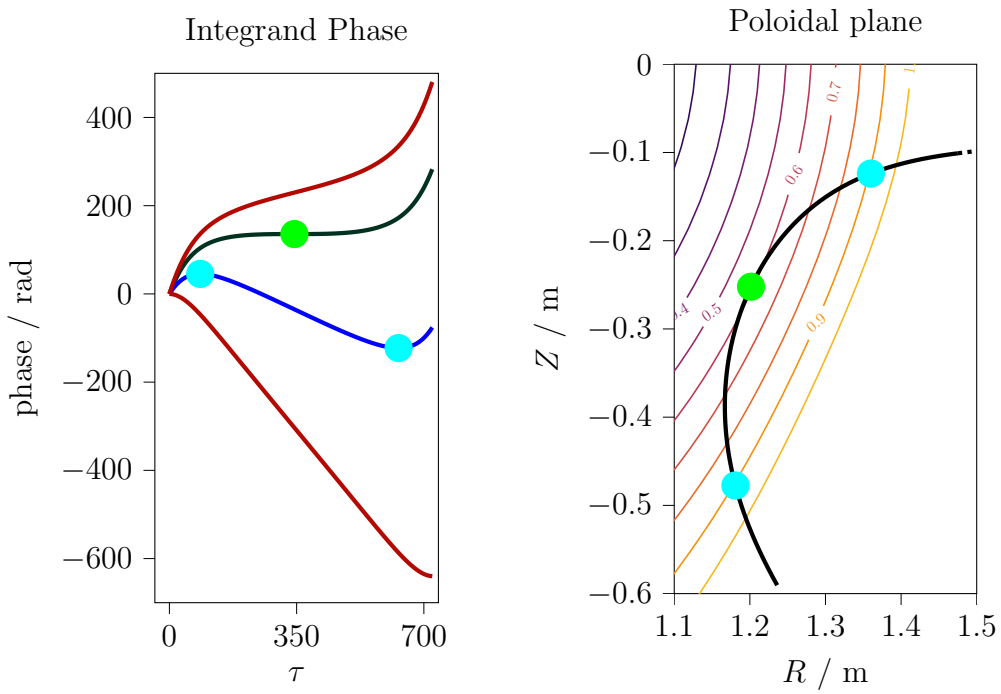

Figure 4.3: Every $k_{\perp,1}$ is associated with scattering at different points of the beam path in our MAST test case. Every point only backscatters one particular $k_{\perp,1}$. Red lines: these values of $k_{\perp,1}$ are not responsible for backscattering along the ray. Green line: the $k_{\perp,1}$ for which backscattering occurs at the extremum. Blue line: this value of $k_{\perp,1}$ backscatters from two points along the ray.

Thus, the final integral is again a Gaussian integral, and slowly-varying functions of τ such as $\delta\tilde{n}_e$ can be simply evaluated at $\tau_a, \tau_b, \ldots$,

$$\delta\tilde{n}_{e,\mu}\left(k_{\perp,1}, k_{\perp,2}, \omega\right) \simeq \delta\tilde{n}_e\left(k_{\perp,1}, k_{\perp,2}, -\int_0^{\tau_\mu} g(\tau')\sin\theta(\tau')\ \mathrm{d}\tau', \omega\right), \tag{4.53}$$

giving

$$\begin{aligned}\tilde{A}_r = &-\frac{\Omega A_{ant} g_{ant}}{2c}\int \sum_{\mu=a,b,\ldots}\left[\frac{\det\left[\mathrm{Im}\left(\boldsymbol{\Psi}_{w,\mu}\right)\right]}{\det\left(\boldsymbol{M}_{w,\mu}\right)}\right]^{\frac{1}{2}}\left[\pi\mathrm{i}\left(g_\mu\frac{\mathrm{d}K}{\mathrm{d}\tau}\Big|_{\tau_\mu}\right)^{-1}\right]^{\frac{1}{2}}\\ &\times\exp\left(2\mathrm{i}\phi_{G,\mu}\right)\ \hat{\mathbf{e}}_\mu^*\cdot\left(\boldsymbol{\epsilon}_{eq,\mu}-\mathbf{1}\right)\cdot\hat{\mathbf{e}}_\mu\frac{\delta\tilde{n}_{e,\mu}}{n_{e,\mu}}\\ &\times\exp\left[-\frac{\mathrm{i}}{4}(2\mathbf{K}_{w,\mu}+\mathbf{k}_\perp)\cdot\boldsymbol{M}_{w,\mu}^{-1}\cdot(2\mathbf{K}_{w,\mu}+\mathbf{k}_\perp)\right]\\ &\times\exp\left(2\mathrm{i}s_\mu+\mathrm{i}k_{\perp,1}\int_0^{\tau_\mu} g(\tau')\left(1-\frac{\theta^2(\tau')}{2}\right)\ \mathrm{d}\tau'\right)\ \mathrm{d}k_{\perp,1}\ \mathrm{d}k_{\perp,2}.\end{aligned} \tag{4.54}$$

With the mismatch angle being small, $\theta_m \sim W/L$, we remark that

$$\begin{aligned}&-\frac{\mathrm{i}}{4}(2\mathbf{K}_{w,\mu}+\mathbf{k}_\perp)\cdot\boldsymbol{M}_{w,\mu}^{-1}\cdot(2\mathbf{K}_{w,\mu}+\mathbf{k}_\perp)\\ &\quad\simeq-\mathrm{i}K_\mu^2\theta_{m,\mu}^2 M_{xx,\mu}^{-1}+\mathrm{i}k_{\perp,2}K_\mu\theta_{m,\mu}M_{xy,\mu}^{-1}-\frac{\mathrm{i}}{4}k_{\perp,2}^2 M_{yy,\mu}^{-1},\end{aligned} \tag{4.55}$$

and the corrections to $\boldsymbol{\Psi}_w$ are

$$M_{xx,\mu} \simeq \Psi_{xx,\mu} - \frac{k_{\perp,1}}{2}\left(\hat{\mathbf{b}}\cdot\nabla\hat{\mathbf{b}}\cdot\hat{\mathbf{g}}\right)_\mu, \tag{4.56}$$

and

$$M_{xy,\mu} \simeq \Psi_{xy,\mu} + \frac{k_{\perp,1}}{2}\frac{\left[\left(\hat{\mathbf{b}}\times\hat{\mathbf{g}}\right)\cdot\nabla\hat{\mathbf{b}}\cdot\hat{\mathbf{g}}\right]_\mu}{\left|\hat{\mathbf{b}}_\mu\times\hat{\mathbf{g}}_\mu\right|}. \tag{4.57}$$

Here we have used, $\hat{\mathbf{x}} \simeq -\hat{\mathbf{b}}$, $\hat{\mathbf{y}} = \hat{\mathbf{b}}\times\hat{\mathbf{g}}/|\hat{\mathbf{b}}\times\hat{\mathbf{g}}|$, and the result that $k_{\perp,2} \sim 1/W$, as we argued in equation (4.36). Hence, the $M_{xx,\mu}$ is modified by the curvature of the magnetic field $\mathbf{B}$, while $M_{xy,\mu}$ is modified by the magnetic shear.

Unfortunately, $\mathrm{d}K/\mathrm{d}\tau = 0$ at a minimum of one point along the ray, since K decreases as the beam enters the plasma and increases as it leaves. A proper treatment of this divergence requires us to consider the next order terms in the Taylor expansion of the phase $2\mathrm{i}s+\mathrm{i}k_{\perp,1}\int_0^{\tau_\mu} g(\tau')\left(1-\theta^2(\tau')/2\right)\ \mathrm{d}\tau'$, which we do in Section 4.3.3. However, this is not an important issue; the divergence is integrable, as we see in Chapter 6.

At this point, we find ourselves in a bit of a pickle. Consider the inverse Fourier transform of the density fluctuations

$$\delta\tilde{n}_{e,\mu}(k_{\perp,1},k_{\perp,2},\omega)=\frac{1}{4\pi^2}\int\delta n_e\left(u_1,u_2,-\int_0^{\tau_\mu}g(\tau')\sin\theta(\tau')\ \mathrm{d}\tau',t\right)\\ \times\exp\left(-\mathrm{i}k_{\perp,1}u_1-\mathrm{i}k_{\perp,2}u_2+\mathrm{i}\omega t\right)\mathrm{d}k_{\perp,1}\ \mathrm{d}k_{\perp,2}\ \mathrm{d}\omega. \quad (4.58)$$

We see from equations (4.11) and (4.12) that $u_1 \sim L$ and $u_2 \sim W$. Consequently, scales as large as $1/L$ for $k_{\perp,1}$ and $1/W$ for $k_{\perp,2}$ are large enough to change $\delta\tilde{n}_{e,\mu}$ by order unity. This is in addition to δn_e changing on the very small scale of λ. Moreover, in equation (4.54), there is a large phase term $k_{\perp,1}\int_0^{\tau_\mu} g(\tau')\mathrm{d}\tau' \sim k_{\perp,1}L \sim L/\lambda \gg 1$. These two facts mean that we have order unity change even when $k_{\perp,1}$ changes by as little as $1/L$ or when $k_{\perp,2}$ changes by $1/W$. Consequently, one would have to consider very large length scales $1/L$ which is not only undesirable from a physical point of view, but also prevents us from evaluating either of the remaining integrals. We can get around this by working with the time-averaged backscattered power instead. Using power avoids the need to deal with the phase, and time averaging leads to separation of scales in $\delta\tilde{n}_{e,\mu}$, thereby eliminating the long length scales. This will be presented in Chapter 5. Before we move on, however, we finish the current chapter by discussing two related issues. First, in Section 4.3.3, we show that there is indeed no divergence in the backscattered signal at the cut-off. Secondly, having worked with the *conventional tokamak* orderings thus far, we deal with the electric field in the *spherical tokamak* case in Section 4.4.

4.3.3 Region near the cut-off

We use τ_c to denote the location where $\mathrm{d}K/\mathrm{d}\tau = 0$. The subscript $_c$ means that the function is evaluated at $\tau = \tau_c$, the nominal cut-off location.

We call $k_{c,1}$ the particular $k_{\perp,1}$ which scatters at τ_c,

$$k_{c,1} = -2K_c = -2K(\tau_c). \quad (4.59)$$

We Taylor expand the large phase piece $2\mathrm{i}s+\mathrm{i}k_{\perp,1}\int_0^\tau g(\tau')\,\mathrm{d}\tau'$ of equation (4.28) around $k_{c,1}$ and τ_c to determine what happens at the scattering location τ_c,

$$2s + k_{\perp,1}\int_0^\tau g(\tau')\,\mathrm{d}\tau = 2s_c + k_{c,1}\int_0^{\tau_c} g(\tau')\,\mathrm{d}\tau + (k_{\perp,1}-k_{c,1})\int_0^{\tau_c} g(\tau')\,\mathrm{d}\tau' + g_c(k_{\perp,1}-k_{c,1})(\tau-\tau_c) + \frac{1}{3}g_c\frac{\mathrm{d}^2K_g}{\mathrm{d}\tau^2}\Big|_{\tau_c}(\tau-\tau_c)^3. \tag{4.60}$$

We order

$$g_c\frac{\mathrm{d}^2K_g}{\mathrm{d}\tau^2}\Big|_{\tau_c}(\tau-\tau_c)^3 \sim \frac{L}{\lambda}\left(\frac{\tau-\tau_c}{\tau_L}\right)^3 \sim 1, \tag{4.61}$$

and

$$g_c(k_{\perp,1}-k_{c,1})(\tau-\tau_c) \sim (k_{\perp,1}-k_{c,1})L\frac{\tau-\tau_c}{\tau_L} \sim 1, \tag{4.62}$$

where $g\tau_L \sim L$. With these orderings, we can safely neglect the terms of the Taylor expansion of the phase that we have not included in equation (4.60). Equations (4.61) and (4.62) give $(\tau-\tau_c)/\tau_L \sim (\lambda/L)^{1/3} \ll 1$ and $(k_{\perp,1}-k_{c,1})/k_{c,1} \sim (\lambda/L)^{2/3} \ll 1$. As a result, functions that do not oscillate quickly with τ are evaluated only at τ_c. Then, using the integration variable

$$\xi = \left(g_c\frac{\mathrm{d}^2K_g}{\mathrm{d}\tau^2}\Big|_{\tau_c}\right)^{\frac{1}{3}}(\tau-\tau_c), \tag{4.63}$$

equation (4.28) becomes

$$\begin{aligned}\tilde{A}_r = -\frac{\Omega A_{ant}g_{ant}\pi}{c}\int &\left[\frac{\det\left[\mathrm{Im}\left(\boldsymbol{\Psi}_{w,c}\right)\right]}{\det\left(\boldsymbol{M}_{w,c}\right)}\right]^{\frac{1}{2}}\exp(2\mathrm{i}\phi_{G,c})\\ &\times\frac{\delta\tilde{n}_{e,c}}{n_{e,c}}\,\hat{\mathbf{e}}_c^*\cdot(\boldsymbol{\epsilon}_{eq,c}-\mathbf{1})\cdot\hat{\mathbf{e}}_c\,\exp\left[2\mathrm{i}s_t+\mathrm{i}k_{\perp,1}\int_0^{\tau_t}g(\tau')\left(1-\frac{\theta^2(\tau')}{2}\right)\,\mathrm{d}\tau'\right]\\ &\times\left(g_t\frac{\mathrm{d}^2K_g}{\mathrm{d}\tau^2}\Big|_{\tau_t}\right)^{-\frac{1}{3}}\mathrm{Ai}\left[(k_{\perp,1}-k_{t,1})g_t^{\frac{2}{3}}\left(\frac{\mathrm{d}^2K_g}{\mathrm{d}\tau^2}\Big|_{\tau_t}\right)^{-\frac{1}{3}}\right]\\ &\times\exp\left[-\frac{\mathrm{i}}{4}(2\mathbf{K}_{w,c}+\mathbf{k}_{\perp,w,c})\cdot\boldsymbol{M}_{w,c}^{-1}\cdot(2\mathbf{K}_{w,c}+\mathbf{k}_{\perp,w,c})\right]\,\mathrm{d}k_{\perp,1}\,\mathrm{d}k_{\perp,2}.\end{aligned} \tag{4.64}$$

where $\mathrm{Ai}(z) = (2\pi)^{-1}\int_{-\infty}^{\infty}\exp(z\xi+\xi^3/3)\mathrm{d}\xi$ is the Airy function. We have thus shown that there is indeed no divergence at the cut-off. This concludes our derivation of the electric field of the *conventional tokamak* case. In the next section, we move on to deriving the electric field for the *spherical tokamak* case.

4.4 Spherical tokamak

At the end of Section 4.2, we introduced the *conventional tokamak* and *spherical tokamak* orderings. Thus far, we have focused on the former. That is, we have taken $\theta_m \sim \lambda/W \ll 1$ along the beam. When the mismatch angle is not small at every point along the beam (*spherical tokamak* ordering), we consider only the simplified case in which one point along the path has no mismatch, $\tau = \tau_0$, and that the mismatch angle is large elsewhere.

To begin, we remind readers of the exponentially decaying piece in equation (4.28)

$$A_r \propto \exp\left[-\frac{\mathrm{i}}{4}\left(2K\sin(\theta+\theta_m)+k_{\perp,1}\sin\theta\right)^2 M_{xx}^{-1}\right], \tag{4.65}$$

where we have used equation (4.42). Since $k_{\perp,1} \sim K$ and $K^2 M_{xx}^{-1} \sim W^2/\lambda^2 \gg 1$, the signal is localised to the points where the mismatch is zero, $\theta_m = 0$, regardless of whether those are near the cut-off or not. Due to equation (4.38), $\theta = 0$ at this point as well. Hence, at the location with zero mismatch, the dominant scattered wavevector is given by the Bragg condition at this point. In a case in which the mismatch angle does not vanish at any point along the ray, we would need to use a steepest descent method to optimise for both the real (mismatch attenuation) and imaginary (stationary phase, conventionally called the Bragg condition) parts of the exponential. However, we will not cover this here.

We perform a Taylor expansion around the point of zero mismatch, for $g\,(\tau - \tau_0) \sim W$, which is a sensible ordering because the equilibrium properties such as the mismatch vary on length scales of L. Hence, a distance of W away from zero mismatch, we expect the mismatch to be $\sim W/L$. Thus, the argument of equation (4.65) is of order unity in the region $g\,(\tau - \tau_0) \sim W$, which means the backscattered signal is already significantly attenuated. The Bragg condition is also not exactly met away from τ_0, hence

$$2K_0 + k_{\perp,1} \sim \frac{1}{W}, \tag{4.66}$$

which we will later prove in equation (5.45).

We begin by introducing a few more orderings. From earlier, we had $\theta_0 = \theta_{m,0} = 0$. However, the derivatives of both θ and θ_m change on the length scale L,

$$\frac{\mathrm{d}\theta}{\mathrm{d}\tau} \sim \frac{\mathrm{d}\theta_m}{\mathrm{d}\tau} \sim \frac{1}{\tau_L}, \tag{4.67}$$

where $\tau_L \sim L/g$; at a distance of L away from τ_0, the mismatch is large $\theta \sim \theta_m \sim 1$. Using these orderings, we find that

$$(\tau - \tau_0) \frac{\mathrm{d}}{\mathrm{d}\tau}\Big|_{\tau_0} (2K_x - k_{\perp,1} \sin\theta) \simeq -2K_0 \frac{\mathrm{d}\theta_m}{\mathrm{d}\tau}\Big|_{\tau_0} (\tau - \tau_0) \sim \frac{1}{W}, \tag{4.68}$$

and

$$\begin{aligned}
&(\tau - \tau_0)^2 \frac{\mathrm{d}^2}{\mathrm{d}\tau^2}\Big|_{\tau_0} (2K_x - k_{\perp,1} \sin\theta) \\
&\quad \simeq \left[-4 \frac{\mathrm{d}K}{\mathrm{d}\tau}\Big|_{\tau_0} \left(\frac{\mathrm{d}\theta_m}{\mathrm{d}\tau}\Big|_{\tau_0} + \frac{\mathrm{d}\theta}{\mathrm{d}\tau}\Big|_{\tau_0} \right) - 2K_0 \frac{\mathrm{d}^2\theta_m}{\mathrm{d}\tau^2}\Big|_{\tau_0} \right] (\tau - \tau_0)^2 \\
&\quad \sim \frac{1}{L},
\end{aligned} \tag{4.69}$$

where we have used equation (4.42), and equation (4.66) to write $k_{\perp,1} \simeq -2K_0$. Taking into account all these considerations, and recalling that $k_{\perp,2} \sim 1/W$, we now Taylor expand the exponentially decaying piece, as well as the large phase piece, keeping terms of order unity

$$\begin{aligned}
&-\frac{1}{4}(2K_x - k_{\perp,1}\sin\theta)^2 M_{xx}^{-1} - \frac{1}{2} k_{\perp,2}(2K_x - k_{\perp,1}\sin\theta) M_{xy}^{-1} - \frac{1}{4} k_{\perp,2}^2 M_{yy}^{-1} \\
&\quad + 2s + k_{\perp,1} \int_0^{\tau} g(\tau') \cos\theta(\tau') \, \mathrm{d}\tau' \\
&\quad \simeq -\frac{1}{4} k_{\perp,2}^2 M_{yy,0}^{-1} + 2s_0 + k_{\perp,1} \int_0^{\tau_0} g(\tau') \cos\theta(\tau') \, \mathrm{d}\tau' \\
&\quad + \left(k_{\perp,2} K_0 \frac{\mathrm{d}\theta_m}{\mathrm{d}\tau}\Big|_{\tau_0} M_{xy,0}^{-1} + 2K_0 g_0 + k_{\perp,1} g_0 \right) (\tau - \tau_0) \\
&\quad + \left[g_0 \frac{\mathrm{d}K}{\mathrm{d}\tau}\Big|_{\tau_0} - K_0^2 \left(\frac{\mathrm{d}\theta_m}{\mathrm{d}\tau}\Big|_{\tau_0} \right)^2 M_{xx,0}^{-1} \right] (\tau - \tau_0)^2 .
\end{aligned} \tag{4.70}$$

To make the equations more manageable, we use the shorthand

$$G_0 \left(k_{\perp,1}, k_{\perp,2} \right) = \left[g_0 \frac{\mathrm{d}K}{\mathrm{d}\tau}\Big|_{\tau_0} - K_0^2 \left(\frac{\mathrm{d}\theta_m}{\mathrm{d}\tau}\Big|_{\tau_0} \right)^2 M_{xx,0}^{-1} \right]^{-1} . \tag{4.71}$$

We now proceed to solve the Gaussian integral in τ to get

$$\begin{aligned}\tilde{A}_r = &-\frac{\Omega A_{ant} g_{ant} \hat{\mathbf{e}}_{ant} \cdot \hat{\mathbf{e}}_{ant}}{2c} \int \left[\frac{\det\left[\mathrm{Im}\left(\boldsymbol{\Psi}_{w,0}\right)\right]}{\det\left(\boldsymbol{M}_{w,0}\right)}\right]^{\frac{1}{2}} \exp(2\mathrm{i}\phi_{G,0}) \\ &\times \frac{\delta\tilde{n}_{e,0}}{n_{e,0}}\ \hat{\mathbf{e}}_0^* \cdot \left(\boldsymbol{\epsilon}_{eq,0} - \mathbf{1}\right) \cdot \hat{\mathbf{e}}_0\ \exp\left(2\mathrm{i}s_0 + \mathrm{i}k_{\perp,1} \int_0^{\tau_0} g(\tau') \cos\theta(\tau')\ \mathrm{d}\tau'\right) \\ &\times \exp\left[-\frac{\mathrm{i}}{4}\left(k_{\perp,2} K_0 \frac{\mathrm{d}\theta_m}{\mathrm{d}\tau}\Big|_{\tau_0} M_{xy,0}^{-1} + 2K_0 g_0 + k_{\perp,1} g_0\right)^2 G_0\right] \\ &\times (\pi\mathrm{i}G_0)^{\frac{1}{2}} \exp\left[-\frac{\mathrm{i}}{4} k_{\perp,2}^2 M_{yy,0}^{-1}\right]\ \mathrm{d}k_{\perp,1}\ \mathrm{d}k_{\perp,2}. \end{aligned} \tag{4.72}$$

Here $\mathrm{Re}\left(\sqrt{\pi\mathrm{i}G_0}\right) \geq 0$ as discussed in Appendix B, and the density fluctuations are evaluated at

$$\delta\tilde{n}_{e,0}\left(k_{\perp,1}, k_{\perp,2}, \omega\right) = \delta\tilde{n}_e\left(k_{\perp,1}, k_{\perp,2}, -\int_0^{\tau_0} g(\tau') \sin\theta(\tau')\ \mathrm{d}\tau', \omega\right). \tag{4.73}$$

In principle, the mismatch could be zero at more than one point along the ray. In that case, the total backscattered signal is the sum of the backscattered signal of each of those points. In the interests of simplicity, we will not discuss this further in this thesis.

Chapter 5

Backscattered power

5.1 Conventional tokamak

For the reasons discussed at the end of Section 4.3.2, it is difficult to evaluate the $k_{\perp,1}$ and $k_{\perp,2}$ integrals when working with the backscattered amplitude. In order to make further analytical progress, we have to eschew the phase of A_r, and work with the time-averaged backscattered power instead. We introduce the correlation function (Section 5.1.1), and proceed to solve the Gaussian integral in $k_{\perp,2}$ (Section 5.1.2). Unfortunately, the final integral in $k_{\perp,1}$ cannot be solved analytically without making assumptions about the turbulence spectrum. This issue, along with a numerical solution to the $k_{\perp,1}$ integral, is discussed in Chapter 6.

5.1.1 Correlation function

We consider the correlation function for two density fluctuations, at $\mathbf{r}, t$ and $\mathbf{r}+\Delta\mathbf{r}, t+\Delta t$,

$$C(\mathbf{r}, t, \Delta\mathbf{r}, \Delta t) = \frac{\langle \delta n_e(\mathbf{r}, t)\delta n_e(\mathbf{r}+\Delta\mathbf{r}, t+\Delta t)\rangle_t}{\langle \delta n_e^2(\mathbf{r}, t)\rangle_t}. \tag{5.1}$$

$\mathbf{r}$ and $\Delta\mathbf{r}$ have different scales after time averaging, and this will be important later. Using equation (4.2), we express the density fluctuations in terms of their Fourier

transforms

$$\begin{aligned}
&\frac{\langle \delta n_e(\mathbf{r},t)\delta n_e(\mathbf{r}+\Delta\mathbf{r},t+\Delta t)\rangle_t}{\langle \delta n_e^2(\mathbf{r},t)\rangle_t} \\
&\quad = \left\langle \delta n_e^2(\mathbf{r},t)\right\rangle_t^{-1} \int \delta\tilde{n}_e\left(k_{\perp,1},k_{\perp,2},u_\parallel+\Delta u_\parallel,\omega\right)\delta\tilde{n}_e^*\left(k'_{\perp,1},k'_{\perp,2},u_\parallel,\omega'\right) \\
&\quad \times \exp\left[\mathrm{i}(k_{\perp,1}-k'_{\perp,1})u_1+\mathrm{i}(k_{\perp,2}-k'_{\perp,2})u_2\right]\left\langle \exp\left[-\mathrm{i}(\omega-\omega')t\right]\right\rangle_t \\
&\quad \times \exp\left(\mathrm{i}k_{\perp,1}\Delta u_1+\mathrm{i}k_{\perp,2}\Delta u_2-\mathrm{i}\omega\Delta t\right)\ \mathrm{d}k_{\perp,1}\ \mathrm{d}k_{\perp,2}\ \mathrm{d}\omega\ \mathrm{d}k'_{\perp,1}\ \mathrm{d}k'_{\perp,2}\ \mathrm{d}\omega'. \qquad (5.2)
\end{aligned}$$

Since we assumed our system was in steady state, we can perform the time average $<>_t$ over a sufficiently large time interval

$$T \gg \frac{1}{\omega}, \qquad (5.3)$$

such that we get a Dirac delta function as follows

$$\int_{-\infty}^{\infty} \exp\left[-\mathrm{i}(\omega-\omega')t\right]\ \mathrm{d}t = 2\pi\delta\left(\omega-\omega'\right). \qquad (5.4)$$

However, this is not true of $k_{\perp,i}-k'_{\perp,i}$, since there is a characteristic long length scale L. After time averaging, we assume separation of scales for $\mathbf{r}$ and $\Delta\mathbf{r}$, which means we have to order

$$k_{\perp,1}-k'_{\perp,1} \sim k_{\perp,2}-k'_{\perp,2} \sim \frac{1}{L}, \qquad (5.5)$$

but

$$k_{\perp,1} \sim k_{\perp,2} \sim \frac{1}{\lambda}. \qquad (5.6)$$

Note the apparent contradiction with equation (4.36): the Fourier transform of the turbulent fluctuations $\delta\tilde{n}_e$ has $k_{\perp,2} \sim 1/\lambda$, but backscattering requires $k_{\perp,2}$ to be as small as $1/W$ per equation (4.36). We will see shortly that this implies that we eventually should take $k_{\perp,2}=0$. For now, however, we get

$$\begin{aligned}
&\frac{\langle \delta n_e(\mathbf{r},t)\delta n_e(\mathbf{r}+\Delta\mathbf{r},t+\Delta t)\rangle_t}{\langle \delta n_e^2(\mathbf{r},t)\rangle_t} \\
&\quad = \left\langle \delta n_e^2(\mathbf{r},t)\right\rangle_t^{-1} \int \delta\tilde{n}_e\left(k_{\perp,1},k_{\perp,2},u_\parallel+\Delta u_\parallel,\omega\right)\delta\tilde{n}_e^*\left(k'_{\perp,1},k'_{\perp,2},u_\parallel,\omega\right) \\
&\quad \times \exp\left[\mathrm{i}(k_{\perp,1}-k'_{\perp,1})u_1+\mathrm{i}(k_{\perp,2}-k'_{\perp,2})u_2\right]\ \mathrm{d}k_{\perp,1}\ \mathrm{d}k_{\perp,2} \\
&\quad \times \exp\left(\mathrm{i}k_{\perp,1}\Delta u_1+\mathrm{i}k_{\perp,2}\Delta u_2-\mathrm{i}\omega\Delta t\right)\ \mathrm{d}\omega\ \mathrm{d}k'_{\perp,1}\ \mathrm{d}k'_{\perp,2}, \qquad (5.7)
\end{aligned}$$

We compare this to the Fourier transform of the correlation function with respect to $\Delta\mathbf{r}$ and Δt, which satisfies

$$C(\mathbf{r}, t, \Delta\mathbf{r}, \Delta t) = \int \widetilde{C}(\mathbf{r}, t, k_{\perp,1}, k_{\perp,2}, \Delta u_{\parallel}, \omega) \times \exp\left(\mathrm{i}k_{\perp,1}\Delta u_1 + \mathrm{i}k_{\perp,2}\Delta u_2 - \mathrm{i}\omega\Delta t\right)\, \mathrm{d}k_{\perp,1}\, \mathrm{d}k_{\perp,2}\, \mathrm{d}\omega. \tag{5.8}$$

Hence, we find that

$$\begin{aligned}\widetilde{C}(\mathbf{r}, t, k_{\perp,1}, k_{\perp,2}, \Delta u_{\parallel}, \omega) &= \left\langle \delta n_e^2(\mathbf{r}, t)\right\rangle_t^{-1} \int \delta\tilde{n}_e\left(k_{\perp,1}, k_{\perp,2}, u_{\parallel} + \Delta u_{\parallel}, \omega\right) \delta\tilde{n}_e^*\left(k'_{\perp,1}, k'_{\perp,2}, u_{\parallel}, \omega\right) \\ &\times \exp\left[\mathrm{i}(k_{\perp,1} - k'_{\perp,1})u_1 + \mathrm{i}(k_{\perp,2} - k'_{\perp,2})u_2\right]\, \mathrm{d}k'_{\perp,1}\, \mathrm{d}k'_{\perp,2}.\end{aligned} \tag{5.9}$$

Since we have assumed a steady-state plasma, there is no slow time dependence, so we drop it from $\widetilde{C}$ from here onwards. The t in δn_e, is a fast time dependence, which we need to keep.

We introduce the backscattered power spectral density p_r, such that the total backscattered power P_r is given by

$$P_r = \int p_r\, \mathrm{d}\omega. \tag{5.10}$$

To evaluate p_r, we multiply the backscattered amplitude, equation (4.54), by its complex conjugate, and we time average over a time T that satisfies equation (5.3) to find

$$\begin{aligned}\frac{p_r}{P_{ant}} &= \int \sum_{\mu=a,b,\ldots} F_\mu(k_{\perp,1}, k_{\perp,2}) \exp\left[2\mathrm{i}s(\tau_\mu(k_{\perp,1})) + \mathrm{i}k_{\perp,1}\int_0^{\tau_\mu(k_{\perp,1})} g(\tau'')\, \mathrm{d}\tau''\right] \\ &\times \delta\tilde{n}_{e,\mu}(k_{\perp,1}, k_{\perp,2}, \omega)\, \mathrm{d}k_{\perp,1}\, \mathrm{d}k_{\perp,2} \\ &\times \int \sum_{\nu=a,b,\ldots} F_\nu^*(k'_{\perp,1}, k'_{\perp,2}) \exp\left[-2\mathrm{i}s(\tau_\nu(k'_{\perp,1})) - \mathrm{i}k'_{\perp,1}\int_0^{\tau_\nu(k'_{\perp,1})} g(\tau'')\, \mathrm{d}\tau''\right] \\ &\times \delta\tilde{n}_{e,\nu}^*(k'_{\perp,1}, k'_{\perp,2}, \omega)\, \mathrm{d}k'_{\perp,1}\, \mathrm{d}k'_{\perp,2},\end{aligned} \tag{5.11}$$

where P_{ant} is the total power emitted by the antenna and where we have abbreviated

the slowly-varying piece of the amplitude (without density fluctuations) as

$$F_\mu(k_{\perp,1},k_{\perp,2}) = \frac{\Omega g_{ant}}{2c}\left[\frac{\det\left[\mathrm{Im}\left(\boldsymbol{\Psi}_{w,\mu}\right)\right]}{\det\left(\boldsymbol{M}_{w,\mu}\right)}\right]^{\frac{1}{2}}\left[\pi\mathrm{i}\left(g_\mu\frac{\mathrm{d}K}{\mathrm{d}\tau}\Big|_{\tau_\mu}\right)^{-1}\right]^{\frac{1}{2}}$$
$$\times\exp\left(2\mathrm{i}\phi_{G,\mu}\right)\ \hat{\mathbf{e}}_\mu^*\cdot\left(\boldsymbol{\epsilon}_{eq,\mu}-\mathbf{1}\right)\cdot\hat{\mathbf{e}}_\mu\frac{1}{n_{e,\mu}}$$
$$\times\exp\left[-\frac{\mathrm{i}}{4}(2\mathbf{K}_{w,\mu}+\mathbf{k}_\perp)\cdot\boldsymbol{M}_{w,\mu}^{-1}\cdot(2\mathbf{K}_{w,\mu}+\mathbf{k}_\perp)\right]$$
$$\times\exp\left(\frac{\mathrm{i}}{2}k_{\perp,1}\int_0^{\tau_\mu}g(\tau')\theta^2(\tau')\ \mathrm{d}\tau'\right). \tag{5.12}$$

We remind readers that τ_μ is a function of $k_{\perp,1}$. Hence, $F_\nu(k'_{\perp,1},k'_{\perp,2})$ would be evaluated at $\tau_\nu(k'_{\perp,1})$, rather than at $\tau_\nu(k_{\perp,1})$. Moving forward, we try to match equation (5.11) with the Fourier transform of the correlation function $\widetilde{C}$. First, we note that $F_\mu(k_{\perp,1},k_{\perp,2})$ depends slowly on $k_{\perp,1}$ and $k_{\perp,2}$, as we have taken the large phase term out of it. Hence, we can neglect $k_{\perp,i}-k'_{\perp,i}\sim 1/L\ll 1$, giving us

$$F_\nu(k'_{\perp,1},k'_{\perp,2})\simeq F_\nu(k_{\perp,1},k_{\perp,2}). \tag{5.13}$$

To deal with the exponential term outside $F_\mu(k_{\perp,1},k_{\perp,2})$, we Taylor expand $\tau_\nu(k'_{\perp,1})$ about $\tau_\nu(k_{\perp,1})$

$$2s\left(\tau_\nu(k'_{\perp,1})\right)+k'_{\perp,1}\int_0^{\tau_\nu(k'_{\perp,1})}g(\tau'')\ \mathrm{d}\tau''$$
$$\simeq 2s\left(\tau_\nu(k_{\perp,1})\right)+k'_{\perp,1}\int_0^{\tau_\nu(k_{\perp,1})}g(\tau'')\ \mathrm{d}\tau''$$
$$+\left[2K_\nu g_\nu+k'_{\perp,1}g_\nu\right]\left[\tau_\nu(k'_{\perp,1})-\tau_\nu(k_{\perp,1})\right]. \tag{5.14}$$

In order to gain the insight we need to proceed further, we consider the following piece of equation (5.11),

$$\sum_{\mu,\nu}\delta\tilde{n}_{e,\mu}(k_{\perp,1},k_{\perp,2},\omega)\delta\tilde{n}^*_{e,\nu}(k'_{\perp,1},k'_{\perp,2},\omega). \tag{5.15}$$

When $\mu\neq\nu$, τ_μ and τ_ν generally correspond to positions that, in the perpendicular direction, are many correlation lengths apart. For $\mu\neq\nu$, $\delta\tilde{n}_{e,\mu}\delta\tilde{n}^*_{e,\nu}$ can only become significant when τ_μ and τ_ν are either close to each other or connected by a length of magnetic field line of the order of the parallel correlation length. Since this only

happens on a countable number of flux surfaces, we ignore this possibility, and assume that when $\mu \neq \nu$, $\delta\tilde{n}_{e,\mu}\delta\tilde{n}^*_{e,\nu}$ is small. Hence, we find that

$$\begin{aligned}
&\sum_{\mu,\nu} \delta\tilde{n}_{e,\mu}(k_{\perp,1}, k_{\perp,2}, \omega)\delta\tilde{n}^*_{e,\nu}(k'_{\perp,1}, k'_{\perp,2}, \omega) \\
&\qquad \times \exp\left[2\mathrm{i}s_\mu + \mathrm{i}k_{\perp,1}\int_0^{\tau_\mu} g(\tau'')\ \mathrm{d}\tau'' - 2\mathrm{i}s_\nu - \mathrm{i}k'_{\perp,1}\int_0^{\tau_\nu} g(\tau'')\ \mathrm{d}\tau''\right] \\
&= \sum_{\mu} \delta\tilde{n}_{e,\mu}(k_{\perp,1}, k_{\perp,2}, \omega)\delta\tilde{n}^*_{e,\mu}(k'_{\perp,1}, k'_{\perp,2}, \omega) \\
&\qquad \times \exp\left\{\mathrm{i}\left(2K_\mu g_\mu + k'_{\perp,1}g_\mu\right)\left[\tau_\mu(k_{\perp,1}) - \tau_\mu(k'_{\perp,1})\right]\right\} \\
&\qquad \times \exp\left[\mathrm{i}\left(k_{\perp,1} - k'_{\perp,1}\right)\int_0^{\tau_\mu} g(\tau'')\ \mathrm{d}\tau''\right].
\end{aligned} \tag{5.16}$$

Here we can neglect the small term $\left(2K_\mu g_\mu + k'_{\perp,1}g_\mu\right)\left[\tau_\mu(k_{\perp,1}) - \tau_\mu(k'_{\perp,1})\right]$. Indeed, using

$$\tau_\mu(k_{\perp,1}) - \tau_\mu(k'_{\perp,1}) = -\frac{1}{2}\left(\frac{\mathrm{d}K}{\mathrm{d}\tau}\Big|_{\tau_\mu}\right)^{-1}(k_{\perp,1} - k'_{\perp,1}), \tag{5.17}$$

which is a result of the Bragg condition, equation (4.50), we show that term to be small,

$$\begin{aligned}
&\left(2K_\mu g_\mu + k'_{\perp,1}g_\mu\right)\left[\tau_\mu(k_{\perp,1}) - \tau_\mu(k'_{\perp,1})\right] \\
&\qquad = \frac{1}{2}\left(\frac{\mathrm{d}K}{\mathrm{d}\tau}\Big|_{\tau_\mu}\right)^{-1} g_\mu(k_{\perp,1} - k'_{\perp,1})^2 \sim \frac{\lambda}{L} \ll 1.
\end{aligned} \tag{5.18}$$

Using equations (5.16) and (5.13), we rewrite equation (5.11) as

$$\begin{aligned}
\frac{p_r}{P_{ant}} = \int \sum_{\mu=a,b,\ldots} &\delta\tilde{n}_{e,\mu}(k_{\perp,1}, k_{\perp,2}, \omega)\delta\tilde{n}^*_{e,\mu'}(k'_{\perp,1}, k'_{\perp,2}, \omega) \\
&\times \exp\left[\left(k_{\perp,1} - k'_{\perp,1}\right)\int_0^{\tau_\mu} g(\tau'')\ \mathrm{d}\tau''\right]\ \mathrm{d}k'_{\perp,1}\ \mathrm{d}k'_{\perp,2} \\
&\times |F_\mu(k_{\perp,1}, k_{\perp,2})|^2\ \mathrm{d}k_{\perp,1}\ \mathrm{d}k_{\perp,2},
\end{aligned} \tag{5.19}$$

and we match the result to the Fourier transform of the correlation function in equation

(5.9). We now get

$$\begin{aligned}\frac{p_r}{P_{ant}} = \frac{1}{4}\frac{\Omega^2}{c^2} g_{ant}^2 \pi \int \sum_{\mu=a,b,\ldots} \frac{\det\left[\mathrm{Im}\left(\boldsymbol{\Psi}_{w,\mu}\right)\right]}{\left|\det\left[\boldsymbol{M}_{w,\mu}\right]\right|} \left|\hat{\mathbf{e}}_\mu^* \cdot \left(\boldsymbol{\epsilon}_{eq,\mu} - \mathbf{1}\right) \cdot \hat{\mathbf{e}}_\mu\right|^2 \\ \times \left| g_\mu \frac{\mathrm{d}K}{\mathrm{d}\tau}\Big|_{\tau_\mu} \right|^{-1} \exp\left[2\mathrm{Im}\left(M_{xx,\mu}^{-1}\right) K_\mu^2 \theta_{m,\mu}^2\right] \\ \times \exp\left[-2\mathrm{Im}\left(M_{xy,\mu}^{-1}\right) K_\mu \theta_{m,\mu} k_{\perp,2} + \frac{1}{2}\mathrm{Im}\left(M_{yy,\mu}^{-1}\right) k_{\perp,2}^2\right] \\ \times \frac{\left\langle \delta n_{e,\mu}^2(t)\right\rangle_t}{n_{e,\mu}^2} \widetilde{C}_\mu(k_{\perp,1}, k_{\perp,2}, \omega)\, \mathrm{d}k_{\perp,1}\, \mathrm{d}k_{\perp,2}. \end{aligned} \tag{5.20}$$

Here, $\Delta u_\parallel$ in $\widetilde{C}_\mu$ is zero and the subscript $_\mu$ indicates that it is evaluated at $u_{\parallel,\mu}$; $\delta n_{e,\mu}^2$ is evaluated at $u_{\parallel,\mu} = -\int_0^{\tau_\mu} g(\tau') \sin\theta(\tau')\, \mathrm{d}\tau' \simeq 0$, $u_2 = 0$, and $u_1 = \int_0^{\tau_\mu} g(\tau'')\, \mathrm{d}\tau''$. Hence, $\mathbf{r} = \mathbf{q}(\tau_\mu(k_{\perp,1}))$, and so, for convenience, we have dropped the $\mathbf{r}$ dependence and denoted it with the subscript $_\mu$ instead.

5.1.2 Gaussian integral in $k_{\perp,2}$

We begin by manipulating equation (5.20) into a more wieldly form. Remarking that

$$\begin{aligned} &-2\mathrm{Im}\left(M_{xy,\mu}^{-1}\right) K_\mu \theta_{m,\mu} k_{\perp,2} + \frac{1}{2}\mathrm{Im}\left(M_{yy,\mu}^{-1}\right) k_{\perp,2}^2 \\ &\quad = \frac{1}{2}\mathrm{Im}\left(M_{yy,\mu}^{-1}\right)\left[k_{\perp,2} - 2K_\mu \theta_{m,\mu} \frac{\mathrm{Im}\left(M_{xy,\mu}^{-1}\right)}{\mathrm{Im}\left(M_{yy,\mu}^{-1}\right)}\right]^2 \\ &\quad - 2K_\mu^2 \theta_{m,\mu}^2 \frac{\left[\mathrm{Im}\left(M_{xy,\mu}^{-1}\right)\right]^2}{\mathrm{Im}\left(M_{yy,\mu}^{-1}\right)}, \end{aligned} \tag{5.21}$$

we see that the $k_{\perp,2}$ integral is a Gaussian integral. Thus, we find the $k_{\perp,2}$ selected by the signal,

$$\begin{aligned} k_{\perp,2} &\simeq k_{\mu,2}(\tau_\mu(k_{\perp,1})) \\ &= 2K_\mu \theta_{m,\mu} \frac{\mathrm{Im}\left(M_{xy,\mu}^{-1}\right)}{\mathrm{Im}\left(M_{yy,\mu}^{-1}\right)} \sim \frac{1}{W}. \end{aligned} \tag{5.22}$$

Interestingly, this is small in mismatch, and is exactly zero when there is no mismatch. The backscattered power is thus

$$\begin{aligned}\frac{p_r}{P_{ant}} = \frac{\pi}{4}\frac{\Omega^2}{c^2}g_{ant}^2 \int \sum_{\mu=a,b,\ldots} \frac{\det\left[\mathrm{Im}\left(\boldsymbol{\Psi}_{w,\mu}\right)\right]}{\left|\det\left[\boldsymbol{M}_{w,\mu}\right]\right|} \left|\hat{\mathbf{e}}_\mu^* \cdot \left(\boldsymbol{\epsilon}_{eq,\mu} - \mathbf{1}\right) \cdot \hat{\mathbf{e}}_\mu\right|^2 \\ \times \left|g_\mu \frac{\mathrm{d}K}{\mathrm{d}\tau}\Big|_{\tau_\mu}\right|^{-1} \exp\left[-2\frac{\left(k_{\perp,2} - k_{\mu,2}\right)^2}{\left(\Delta k_{\mu,2}\right)^2}\right] \exp\left[-2\frac{\theta_{m,\mu}^2}{\left(\Delta\theta_{m,\mu}\right)^2}\right] \\ \times \frac{\left\langle \delta n_{e,\mu}^2(t)\right\rangle_t}{n_{e,\mu}^2} \widetilde{C}_\mu(k_{\perp,1}, k_{\perp,2}, \omega)\ \mathrm{d}k_{\perp,1}\ \mathrm{d}k_{\perp,2}. \end{aligned} \tag{5.23}$$

Here, we use the notation

$$\Delta\theta_{m,\mu} = \frac{1}{K_\mu}\left(\frac{\mathrm{Im}\left(M_{yy,\mu}^{-1}\right)}{\left[\mathrm{Im}\left(M_{xy,\mu}^{-1}\right)\right]^2 - \mathrm{Im}\left(M_{xx,\mu}^{-1}\right)\mathrm{Im}\left(M_{yy,\mu}^{-1}\right)}\right)^{\frac{1}{2}}, \tag{5.24}$$

which gives the characteristic $1/\mathrm{e}^2$ width of the mismatch attenuation and

$$\Delta k_{\mu,2} = 2\left(\frac{-1}{\mathrm{Im}\left(M_{yy,\mu}^{-1}\right)}\right)^{\frac{1}{2}}, \tag{5.25}$$

which gives us the wavenumber resolution (in $1/\mathrm{e}^2$). For those seeking to design a synthetic DBS to study data from gyrokinetic simulations, equation (5.23) is the form of the backscattered signal that we recommend using.

If we take the $k_{\perp,2}$ wavenumber resolution, $\Delta k_{\mu,2}$, to be small, we can evaluate the Gaussian integral by using the approximation $k_{\perp,2} \simeq k_{\mu,2} \simeq 0$ in $\widetilde{C}_\mu$, $M_{xx,\mu}$, and $M_{xy,\mu}$. After doing this, we get

$$\begin{aligned}\frac{p_r}{P_{ant}} = \frac{\sqrt{2\pi^3}}{4}\frac{\Omega^2}{c^2}g_{ant}^2 \int \sum_{\mu=a,b,\ldots} \frac{\det\left[\mathrm{Im}\left(\boldsymbol{\Psi}_{w,\mu}\right)\right]}{\left|\det\left[\boldsymbol{M}_{w,\mu}\right]\right|} \left|\hat{\mathbf{e}}_\mu^* \cdot \left(\boldsymbol{\epsilon}_{eq,\mu} - \mathbf{1}\right) \cdot \hat{\mathbf{e}}_\mu\right|^2 \\ \times \left|g_\mu \frac{\mathrm{d}K}{\mathrm{d}\tau}\Big|_{\tau_\mu}\right|^{-1} \left[-\mathrm{Im}\left(M_{yy,\mu}^{-1}\right)\right]^{-\frac{1}{2}} \exp\left(-2\frac{\theta_{m,\mu}^2}{\left(\Delta\theta_{m,\mu}\right)^2}\right) \\ \times \frac{\left\langle \delta n_{e,\mu}^2(t)\right\rangle_t}{n_{e,\mu}^2} \widetilde{C}_\mu(k_{\perp,1}, k_{\mu,2}, \omega)\ \mathrm{d}k_{\perp,1}. \end{aligned} \tag{5.26}$$

Here $M_{xx,\mu}$ as well as $M_{xy,\mu}$ are evaluated at $k_{\perp,2} = k_{\mu,2}$. The final integral in $k_{\perp,1}$ cannot be evaluated analytically. However, we can make a few simplifications to the current form of the backscattered power, thereby making clearer the physics involved.

5.1.3 Final simplifications

We hone in on three pieces of equation (5.26), showing how they may be normalised and re-expressed in more explicit forms. We begin by writing equation (5.26) as

$$\frac{p_r}{P_{ant}} = \frac{\sqrt{\pi^3}e^4}{2c^2\Omega^2\epsilon_0^2 m_e^2 \bar{W}_y} \sum_{\mu=a,b,\ldots} \int \varepsilon_\mu \frac{\bar{W}_y \det\left[\mathrm{Im}\left(\boldsymbol{\Psi}_w\right)\right]}{\sqrt{2}\left|\det\left[\boldsymbol{M}_w\right]\right| \left[-\mathrm{Im}\left(M_{yy}^{-1}\right)\right]^{\frac{1}{2}}} \exp\left(-2\frac{\theta_m^2}{\left(\Delta\theta_m\right)^2}\right) \times \left\langle \delta n_e^2(t)\right\rangle_t \widetilde{C}_\mu(k_{\perp,1}, k_{\mu,2}, \omega)\; g_{ant}^2 \left| g_\mu \frac{\mathrm{d}K}{\mathrm{d}\tau}\Big|_{\tau_\mu}\right|^{-1} \mathrm{d}k_{\perp,1}, \tag{5.27}$$

where ε and $\bar{W}_y$ will be introduced in the following lines. The first piece we focus on is related to the polarisation; we call this piece ε,

$$\varepsilon_\mu = \frac{\Omega^4\epsilon_0^2 m_e^2}{e^4 n_{e,\mu}^2} |\hat{\mathbf{e}}_\mu^* \cdot (\boldsymbol{\epsilon}_{eq,\mu} - \mathbf{1}) \cdot \hat{\mathbf{e}}_\mu|^2. \tag{5.28}$$

The second pertains to the widths (beam) and curvatures (beam and field lines),

$$\frac{\bar{W}_y}{\sqrt{2}} \frac{\det\left[\mathrm{Im}\left(\boldsymbol{\Psi}_{w,\mu}\right)\right]}{\left|\det\left[\boldsymbol{M}_{w,\mu}\right]\right| \left[-\mathrm{Im}\left(M_{yy,\mu}^{-1}\right)\right]^{\frac{1}{2}}}. \tag{5.29}$$

Here $\bar{W}_y$ is the value that $W_y = \sqrt{2/\mathrm{Im}(\Psi_{yy})}$ takes at the beam waist, in vacuum. The final piece contains the integrable divergence

$$g_{ant}^2 \left| g_\mu \frac{\mathrm{d}K}{\mathrm{d}\tau}\Big|_{\tau_\mu}\right|^{-1} \mathrm{d}k_{\perp,1}. \tag{5.30}$$

We first look into the polarisation piece, ε. Using equation (2.99) and recalling that the polarisation $\hat{\mathbf{e}}$ is the eigenvector of $\boldsymbol{D}$ corresponding to $H = 0$, see Section 2.1.2, we re-express the polarisation piece as

$$\varepsilon_\mu = \frac{\Omega^4\epsilon_0^2 m_e^2}{e^4 n_{e,\mu}^2} \left| \frac{c^2}{\Omega^2} K_\mu^2 \left[1 - \left(\hat{\mathbf{K}}_\mu \cdot \hat{\mathbf{e}}_\mu\right)^2\right] - 1\right|^2. \tag{5.31}$$

This expression can be made simpler for the O-mode, but is less obvious for the X-mode. Assuming the polarisation is reasonably well-aligned upon entering the plasma, we have $\hat{\mathbf{e}} \cdot \hat{\mathbf{b}} \simeq 1$ for the O-mode. For the cold plasma dispersion relation, $\mathbf{K} = K\cos\theta_m \hat{\mathbf{u}}_1 + K\sin\theta_m \hat{\mathbf{b}}$ by definition of the mismatch angle, and consequently $|\hat{\mathbf{K}} \cdot \hat{\mathbf{e}}| \sim \theta_m$ for the O-mode. Thus, the O-mode polarisation piece is

$$\varepsilon_\mu = \frac{\Omega^4\epsilon_0^2 m_e^2}{e^4 n_{e,\mu}^2} \left(\frac{c^2}{\Omega^2} K_\mu^2 - 1\right)^2. \tag{5.32}$$

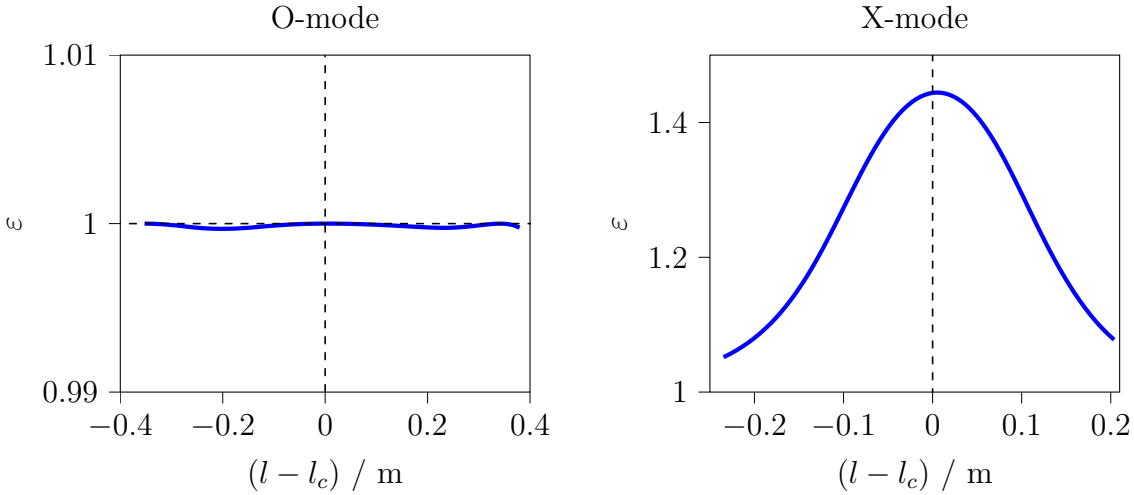

Figure 5.1: The O-mode polarisation piece (left) and that of the X-mode (right) along the ray, for the MAST test case. Notice that the O-mode polarisation piece is almost exactly 1, as expected. The X-mode polarisation piece does seem to give more localisation to the cut-off, but this may not be generally true.

Making use of the O-mode dispersion, $\epsilon_{bb,\mu} - K_\mu^2 c^2/\Omega^2 \simeq 0$, we find that

$$\varepsilon_\mu \simeq 1, \tag{5.33}$$

which is constant, see Figure 5.1 (left). For the X-mode, even when $\theta_m = 0$, the polarisation piece ε depends on the relative sizes of Ω_{ce} and Ω_{pe}. Since we do not make any assumptions about them, we will not further simplify the polarisation piece for the X-mode in this work. Should one wish to calculate the polarisation piece of the X-mode, one should use its full expression, given in equation (5.31). An example is given in Figure 5.1 (right).

Subsequently, we briefly discuss the piece related to the widths and curvatures,

$$\frac{\bar{W}_y}{\sqrt{2}} \frac{\det\left[\mathrm{Im}\left(\boldsymbol{\Psi}_{w,\mu}\right)\right]}{\left|\det\left[\boldsymbol{M}_{w,\mu}\right]\right| \left[-\mathrm{Im}\left(M_{yy,\mu}^{-1}\right)\right]^{\frac{1}{2}}}. \tag{5.34}$$

Due to the complexity of this piece, we do not simplify it any further. Instead, we explain our choice of normalisation. The idea is that we want this piece to be 1 under certain conditions which make the problem easier. Consider the waist of a Gaussian beam in vacuum. Take $\boldsymbol{M} = \boldsymbol{\Psi}$ for simplicity. Assume also that this beam is not astigmatic, that is, the beam widths are minimised at the same point in τ. At this

same point, the real parts of $\boldsymbol{\Psi}$ are simply 0. If $\boldsymbol{\Psi}_w$ is also diagonal in the $(\hat{\mathbf{x}}, \hat{\mathbf{y}}, \hat{\mathbf{g}})$ basis, then the prefactor $\bar{W}_y/\sqrt{2}$ ensures that this piece is 1.

Finally, we simplify the piece containing the integrable divergence. First, differentiate the Bragg condition with respect to τ

$$\frac{\mathrm{d}k_{\perp,1}}{\mathrm{d}\tau} = -2\frac{\mathrm{d}K}{\mathrm{d}\tau}, \tag{5.35}$$

and use this to find that

$$\mathrm{d}k_{\perp,1}\left|g_\mu \frac{\mathrm{d}K}{\mathrm{d}\tau}\Big|_{\tau_\mu}\right|^{-1} = \frac{2}{g}\mathrm{d}\tau_\mu. \tag{5.36}$$

Since we sum over μ, equation (5.23), we can express the integration as being over the beam path,

$$\frac{2}{g_\mu}\mathrm{d}\tau_\mu = \frac{2}{g^2}\mathrm{d}l. \tag{5.37}$$

This piece is thus

$$g_{ant}^2\left|g_\mu \frac{\mathrm{d}K}{\mathrm{d}\tau}\Big|_{\tau_\mu}\right|^{-1}\mathrm{d}k_{\perp,1} = \frac{g_{ant}^2}{g^2}\mathrm{d}l, \tag{5.38}$$

where one has to be careful to use the form of the dispersion relation used in our beam tracing derivation, equation (2.100). Using the definition of H, we find that equation (4.33) gives us $g_{ant} = 2c/\Omega$ (since we take the antenna to be in vacuum).

In summary, after all these simplifications are done and dusted, equation (5.27) is now

$$\frac{p_r}{P_{ant}} = \frac{\sqrt{\pi^3}e^4}{2c^2\Omega^2\epsilon_0^2 m_e^2 \bar{W}_y}\int \varepsilon\, \frac{g_{ant}^2}{g^2}\frac{\bar{W}_y \det\left[\mathrm{Im}\left(\boldsymbol{\Psi}_w\right)\right]}{\sqrt{2}\left|\det\left[\boldsymbol{M}_w\right]\right|\left[-\mathrm{Im}\left(M_{yy}^{-1}\right)\right]^{\frac{1}{2}}} \times \exp\left(-2\frac{\theta_m^2}{\left(\Delta\theta_m\right)^2}\right)\left\langle \delta n_e^2(t)\right\rangle_t \widetilde{C}_l(\omega)\ \mathrm{d}l. \tag{5.39}$$

We remind readers that the variables in this equation are now functions of arc-length along the ray, which is why we have dropped the subscript $_\mu$. The notation $\widetilde{C}_l$ indicates that the correlation function is evaluated at $\mathbf{q}(\tau(l))$, $k_{l,1}(l)$, $k_{\perp,2} = 0$, and $\Delta u_\parallel = 0$, which are all functions of arc-length as well. Note that ε is given by equation (5.31); for the O-mode, this can be simplified to equation (5.33), while we do not further simplify it for the X-mode.

Chapters 6–8 explore localisation, wavenumber resolution, and mismatch attenuation, which are various pieces of equations (5.23) and (5.39).

5.2 Spherical tokamak

Before we continue further, we first show that in the appropriate limit, the *conventional* and *spherical* cases give the same result. This enables us to use the *conventional tokamak* formulation even in cases which are moderately in the *spherical tokamak* regime. Showing that the backscattered amplitudes in these cases match is challenging due to the large phase term $k_{\perp,1}\int_0^\tau g(\tau')\cos\theta(\tau')\mathrm{d}\tau'$. Instead, it is easier to show that the backscattered powers match. To do this, we perform subsidiary expansions of both the *conventional* and *spherical* expressions. For the former, we take the mismatch to be large and perform a Taylor expansion of $k_{\perp,1}$ about $-2K_0$. For the *spherical* case, we make the mismatch less than order unity $\theta_m \ll 1$ throughout the beam path. In this intermediate range,

$$1 \gg \theta_m \gg \frac{\lambda}{W}, \tag{5.40}$$

both models should be applicable and must coincide.

In such an endeavour, the backscattered power of the *conventional* case is given by equation (5.20); that of the *spherical* case can be determined by applying the same methods used in Section 5.1, giving

$$\begin{aligned}\frac{p_r}{P_{ant}} = {}& \frac{1}{4}\frac{\Omega^2}{c^2} g_{ant}^2 \left|\hat{\mathbf{e}}_{ant}\cdot\hat{\mathbf{e}}_{ant}\right|^2 \pi \int \frac{\det\left[\mathrm{Im}\left(\boldsymbol{\Psi}_{w,0}\right)\right]}{\left|\det\left(\boldsymbol{M}_{w,0}\right)\right|} \left|\hat{\mathbf{e}}_0^*\cdot\left(\boldsymbol{\epsilon}_{eq,0}-\mathbf{1}\right)\cdot\hat{\mathbf{e}}_0\right|^2 \\ & \times \frac{1}{|G_0|}\exp\left\{\frac{1}{2}\,\mathrm{Im}\left[\left(k_{\perp,2}K_0\frac{\mathrm{d}\theta_m}{\mathrm{d}\tau}\Big|_{\tau_0} M_{xy,0}^{-1} + 2K_0 g_0 + k_{\perp,1} g_0\right)^2 G_0\right]\right\} \\ & \times \exp\left[\frac{1}{2}\mathrm{Im}\left(M_{yy,0}^{-1}\right)k_{\perp,2}^2\right] \frac{\left\langle \delta n_{e,0}^2(t)\right\rangle_t}{n_{e,0}^2}\widetilde{C}_0(k_{\perp,1},k_{\perp,2},\omega)\;\mathrm{d}k_{\perp,1}\;\mathrm{d}k_{\perp,2}.\end{aligned} \tag{5.41}$$

We now perform the subsidiary expansion of the *spherical case*. We begin by expanding G_0 — see equation (5.41) — to get

$$\begin{aligned}G_0 &= \left(\frac{\mathrm{d}K}{\mathrm{d}\tau}\Big|_{\tau_0} g_0 - K_0^2\left(\frac{\mathrm{d}\theta_m}{\mathrm{d}\tau}\Big|_{\tau_0}\right)^2 M_{xx,0}^{-1}\right)^{-1} \\ &\simeq \left(\frac{\mathrm{d}K}{\mathrm{d}\tau}\Big|_{\tau_0} g_0\right)^{-1} + K_0^2\left(\frac{\mathrm{d}\theta_m}{\mathrm{d}\tau}\Big|_{\tau_0}\right)^2 M_{xx,0}^{-1}\left(\frac{\mathrm{d}K}{\mathrm{d}\tau}\Big|_{\tau_0} g_0\right)^{-2},\end{aligned} \tag{5.42}$$

where we have kept terms up to order unity for the exponential. However, when it comes to the $|G_0|^{-1}$ outside the exponential, see equation (5.41), we only need to keep

the zeroth order term, ignoring the first order correction. It is worth noting that we looked at several MAST shots, and the difference between the full expression and the expansion was indeed negligible. We introduce the notation

$$\Delta k_{\perp,1} = k_{\perp,1} - k_{\perp,1,0} = k_{\perp,1} + 2K_0, \tag{5.43}$$

where we have used the Bragg condition at the zero-mismatch point. We see that the signal decays exponentially with $\Delta k_{\perp,1}$, hence we order the most quickly decaying term to be of order one

$$-\mathrm{Im}\left[\left(\Delta k_{\perp,1}\right)^2 K_0^2 \left(\frac{\mathrm{d}\theta_m}{\mathrm{d}\tau}\Big|_{\tau_0}\right)^2 M_{xx,0}^{-1} \left(\frac{\mathrm{d}K}{\mathrm{d}\tau}\Big|_{\tau_0}\right)^{-2}\right] \sim 1. \tag{5.44}$$

This gives us the size of $\Delta k_{\perp,1}$

$$\Delta k_{\perp,1} \sim \frac{1}{\theta_m W}, \tag{5.45}$$

which makes physical sense, since one would expect better localisation at τ_0 with larger mismatch along the ray. In the *spherical tokamak* subsection, we had $\theta_m \sim 1$, which gives $\Delta k_{\perp,1} \sim 1/W$, justifying equation (4.66). We now take $\theta_m \ll 1$ and expand the exponentially decaying piece from equation (4.72), using equations (5.42), (5.43), and (5.45), getting

$$\begin{aligned}
&\frac{1}{2}\mathrm{Im}\left[\left(k_{\perp,2}K_0\frac{\mathrm{d}\theta_m}{\mathrm{d}\tau}\Big|_{\tau_0} M_{xy,0}^{-1} + g_0\Delta k_{\perp,1}\right)^2 \left(g_0\frac{\mathrm{d}K}{\mathrm{d}\tau}\Big|_{\tau_0} - K_0^2\left(\frac{\mathrm{d}\theta_m}{\mathrm{d}\tau}\Big|_{\tau_0}\right)^2 M_{xx,0}^{-1}\right)^{-1}\right] \\
&\quad + \frac{1}{2}\mathrm{Im}\left(M_{yy,0}^{-1}\right) k_{\perp,2}^2 \\
&\simeq \frac{1}{2}\Delta k_{\perp,1}^2 K_0^2 \left(\frac{\mathrm{d}\theta_m}{\mathrm{d}\tau}\Big|_{\tau_0}\right)^2 \left(\frac{\mathrm{d}K}{\mathrm{d}\tau}\Big|_{\tau_0}\right)^{-2} \mathrm{Im}\left(M_{xx,0}^{-1}\right) \\
&\quad + k_{\perp,2}\Delta k_{\perp,1} K_0 \frac{\mathrm{d}\theta_m}{\mathrm{d}\tau}\Big|_{\tau_0} \left(\frac{\mathrm{d}K}{\mathrm{d}\tau}\Big|_{\tau_0}\right)^{-1} \mathrm{Im}\left(M_{xy,0}^{-1}\right) + \frac{1}{2}k_{\perp,2}^2 \mathrm{Im}\left(M_{yy,0}^{-1}\right),
\end{aligned} \tag{5.46}$$

where we have neglected terms that are small.

We proceed to perform a subsidiary expansion of the *conventional tokamak* case, equation (4.54), in the limit $\theta_m \gg \lambda/W$. To determine the relationship between τ_μ and $k_{\perp,1}$ around τ_0, we differentiate equation (4.49) with respect to τ, at $\tau = \tau_0$, to get

$$\frac{\mathrm{d}\tau_\mu}{\mathrm{d}k_{\perp,1}}\Big|_{\perp,1,0} = -\left(2\frac{\mathrm{d}K}{\mathrm{d}\tau}\Big|_{\tau_0}\right)^{-1}, \tag{5.47}$$

which we then use in our expansion in $k_{\perp,1}$ of the exponential decaying piece in equation (5.20). Together with equations (5.43), and (5.45), this gives us

$$\begin{aligned}
&2\mathrm{Im}\left(M^{-1}_{xx,\mu}\right) K^2_\mu \theta^2_{m,\mu} - 2\mathrm{Im}\left(M^{-1}_{xy,\mu}\right) K_\mu \theta_{m,\mu} k_{\perp,2} + \frac{1}{2}\mathrm{Im}\left(M^{-1}_{yy,\mu}\right) k^2_{\perp,2} \\
&= \frac{1}{2} k^2_{\perp,2}\left(M^{-1}_{yy,0}\right) + \; k_{\perp,2}\left(M^{-1}_{xy,0}\right) \Delta k_{\perp,1} \left(\frac{\mathrm{d}K}{\mathrm{d}\tau}\Big|_{\tau_0}\right)^{-1} K_0 \frac{\mathrm{d}\theta_m}{\mathrm{d}\tau}\Big|_{\tau_0} \\
&\quad + \frac{1}{2}\left(M^{-1}_{xx,0}\right) \Delta k^2_{\perp,1} \left(K_0 \frac{\mathrm{d}\theta_m}{\mathrm{d}\tau}\Big|_{\tau_0}\right)^2 \left(\frac{\mathrm{d}K}{\mathrm{d}\tau}\Big|_{\tau_0}\right)^{-2},
\end{aligned} \tag{5.48}$$

where we have neglected terms which are small $\ll 1$ and recalled that the Bragg condition is exactly met at τ_0. We note that equations (5.46) and (5.48) match, showing that the exponential decay is indeed the same in both cases. As such, we can use the *conventional tokamak* formulation even for moderate *spherical tokamak* cases.

Chapter 6

Localisation

As the beam propagates through the plasma, it is backscattered by various different $k_{\perp,1}$, the exact value of which is given by the Bragg condition. Whereas it might be tempting to think of some sort of 'wavenumber resolution' for $k_{\perp,1}$, having to fulfil the Bragg condition means that each $k_{\perp,1}$ is associated with specific points along the ray. Hence, it is more physically suitable to think of the spread of backscattered $k_{\perp,1}$ as localisation along the ray. A large part of the backscattered power comes from near the cut-off, as we will see shortly. The localisation around the cut-off due to scattering physics is strong, but on its own it is not enough to restrict the backscattered signal to the cut-off. We seek to understand how we can get further localisation, by studying the prefactor

$$\frac{g_{ant}^2}{g^2} \frac{\bar{W}_y \det\left[\mathrm{Im}\left(\boldsymbol{\Psi}_w\right)\right]}{\sqrt{2}\left|\det\left[\boldsymbol{M}_w\right]\right| \left[-\mathrm{Im}\left(M_{yy}^{-1}\right)\right]^{\frac{1}{2}}}. \tag{6.1}$$

of the density fluctuations and correlation function in equation (5.26). We have deliberately omitted the pieces associated with polarisation, equation (5.31), and mismatch

$$\exp\left[-2\frac{\theta_m^2}{\left(\Delta\theta_m\right)^2}\right]. \tag{6.2}$$

The mismatch may indeed affect localisation (Chapter 9), and in fact, is the dominant mechanism of localisation in the *spherical tokamak* case (Section 4.4). However, assuming we are not dealing with such extreme situations, we deem it more physically insightful to discuss the effect of mismatch later (Chapters 8 and 9).

We analyse two contributions to the localisation, which we call the *ray* piece

$$\frac{g_{ant}^2}{g^2}, \tag{6.3}$$

and the *beam* piece

$$\frac{\bar{W}_y \det\left[\mathrm{Im}\left(\boldsymbol{\Psi}_w\right)\right]}{\sqrt{2}\left|\det\left[\boldsymbol{M}_w\right]\right|\left[-\mathrm{Im}\left(M_{yy}^{-1}\right)\right]^{\frac{1}{2}}}. \tag{6.4}$$

They are named as such because the former can be determined with ray tracing alone, while the latter requires beam tracing. The *ray* piece requires one to use the appropriate dispersion relation, equation (2.100), to calculate the group velocity.

We now apply our model to our MAST test case. In Figure 6.1, we show the localisation due to the *ray* and *beam* pieces. We see that there is some localisation to the cut-off due to the *ray* piece. Since the localisation associated with the *ray* and *beam* pieces is complicated, we use the following method to determine the localisation length. First, integrate the localisation with respect to arc length along the central ray, from the point the beam enters the plasma until the point it leaves. Second, choose two points along the ray, integrate localisation with respect to arc length l from the first point to the second, and make sure that this result is 80% that of the first integral. These two points show the start and end of the region where most of the signal is coming from. In this work, we choose the first and second points such that the value of the localisation piece is the same at these two points. Third, take the localisation length to be half of the arc length between the first and second points. The localisation length associated with the combined *beam* and *ray* pieces calculated by this method is 19cm, which is large, indicating that, in experiments, there are probably other mechanisms of localisation.

We now consider the turbulence spectrum, which may futher contribute to localisation. For electrostatic turbulece, references [68–70] suggest that the spectrum is of the form $\widetilde{C}_\mu(k_{\perp,1}, k_{\mu,2}, \omega) \propto k_\perp^{-10/3}$ for $k_\perp \rho_i \ll 1$ and $\widetilde{C}_\mu(k_{\perp,1}, k_{\mu,2}, \omega) \propto k_\perp^{-13/3}$ for $k_\perp \rho_i \gg 1$. The spectrum piece associated with the backscattered power is thus

$$\left(\frac{K}{K_{ant}}\right)^{-\frac{10}{3}} \qquad \text{or} \qquad \left(\frac{K}{K_{ant}}\right)^{-\frac{13}{3}}, \tag{6.5}$$

where we have used the Bragg condition to express $k_{\perp,1}$ in terms of the beam's wavenumber. Since the magnitude of the wavevector is minimum at the cut-off, there is significantly more turbulence with the appropriate $k_{\perp,1}$ for backscattering. We now multiply the piece $(K/K_{ant})^{-13/3}$, Figure 6.2 (left), together with the beam and ray pieces, and

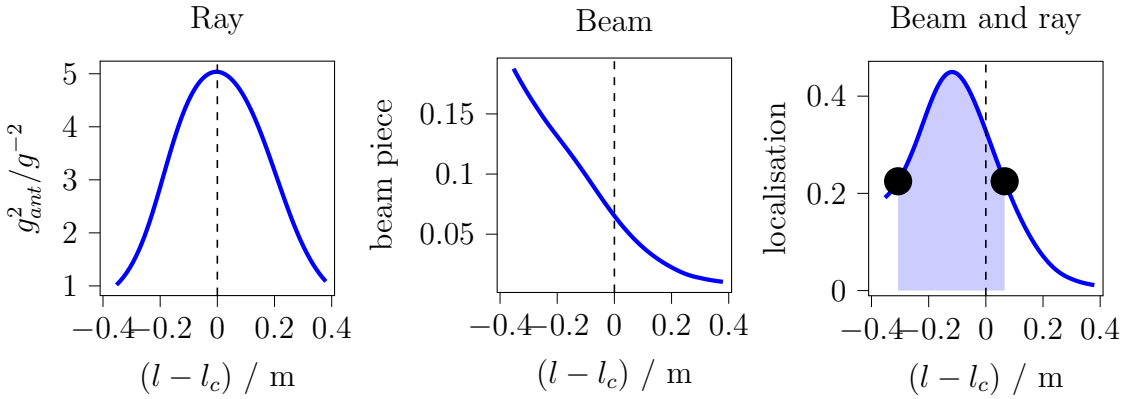

Figure 6.1: Ray (left) and beam (middle) contributions to localisation as a function of distance along the central ray from the cut-off location for the MAST test case. The beam piece is given explicitly in equation (6.4). Product of the ray and beam pieces (right); the shaded area is 80% of the total area under the curve. Black points mark the start and end of the shaded area; note that we have chosen these points such that they have the same ordinate value, that is, the same value of localisation. The corresponding half width is 19cm.

see what this overall localisation gives, Figure 6.2 (right). We find the localisation length, after taking the spectrum into account, to be around 13cm for our MAST test case, Figure 6.2.

It is important to note that this distance $l-l_c$, where l_c is the arc-length of the cut-off position, is measured along the ray. For an O-mode beam, the ray's radial component of group velocity is small near the cut-off, hence more of the signal is coming from fairly similar flux surfaces, unlike what it might ostensibly seem given the fairly large half-width, see Figure 6.3. Apart from that, it is interesting to note that the peak of localisation is shifted away from the cut-off, by around $l - l_c = 6$cm or so, due to the changing *beam* piece near the cut-off. The physical intuition as to why the *beam* piece decreases as the beam propagates is as follows: the MAST DBS was designed to have the beam waist before the plasma, hence the beam is always getting wider while in the plasma. Thus far, we have shown plots of the integrand of equation (5.39), and calculated the associated localisation lengths. Since these lengths are calculated from the cumulative integrals of the localisation pieces, we plot the cumulative integrals themselves in Figure 6.4.

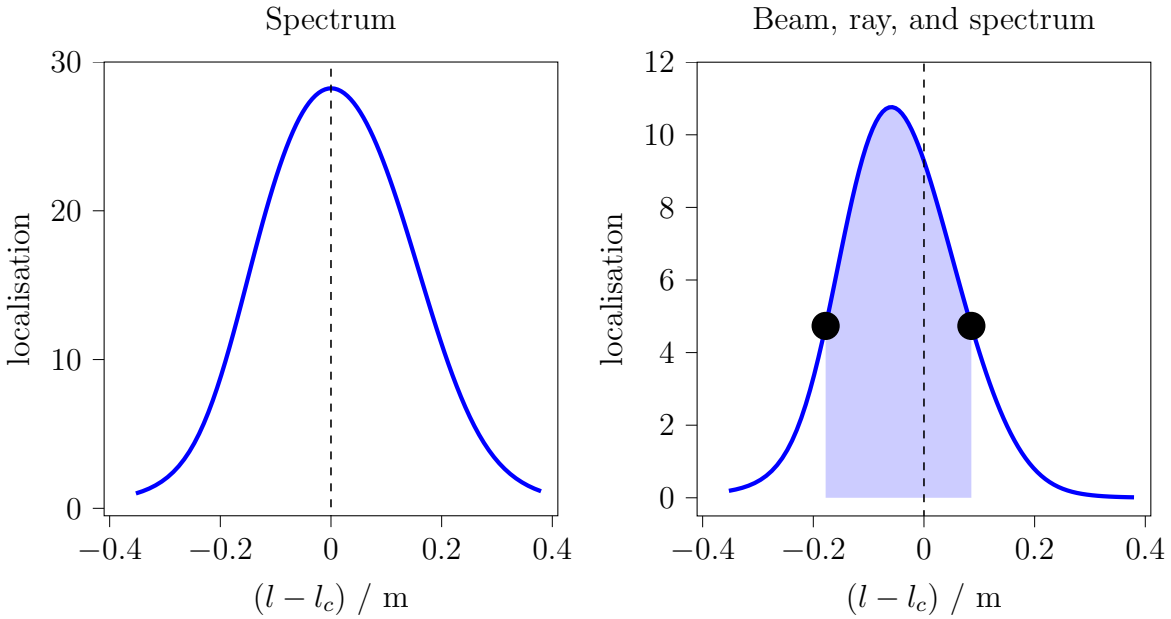

Figure 6.2: Localisation due to the power-law turbulence spectrum (left) and overall localisation (right). Here l_c is the distance along the central ray, from launch to cut-off location. The overall localisation is the product of equations (6.4), (6.2), and (6.5). The shaded area is 80% of the total area under the curve, and the black points mark the start and end of the shaded area. The corresponding half width is 13cm. Note that we have chosen the black points such that they have the same ordinate value, that is, the same value of localisation.

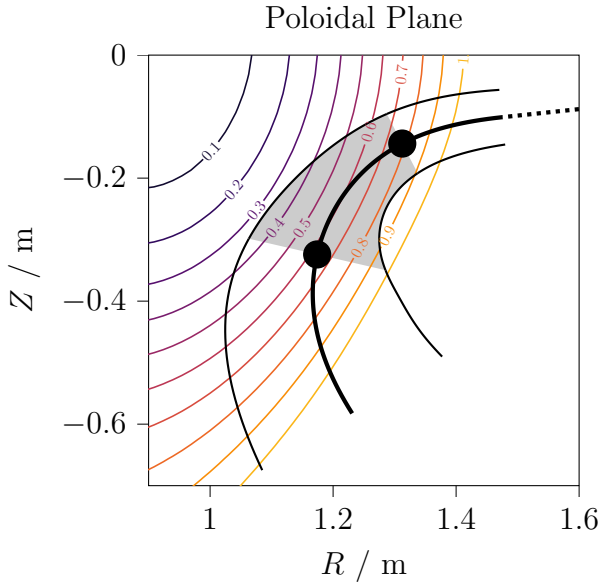

Figure 6.3: Most of the signal (80%) comes from the region between the two black points. The thick solid line shows the path of the central ray. Thin solid lines give the 1/e positions of the Gaussian beam's electric field, and the dotted lines show the ray's propagation in vacuum.

Since every point along the ray is associated with a particular $k_{\perp,1}$ as a result of the stationary phase integral in Section 4.3.2, it is impossible to divorce the localisation and $k_{\perp,1}$ resolution. We show how to calculate the associated $k_{\perp,1}$ resolution from the spatial localisation in Section 7.1.

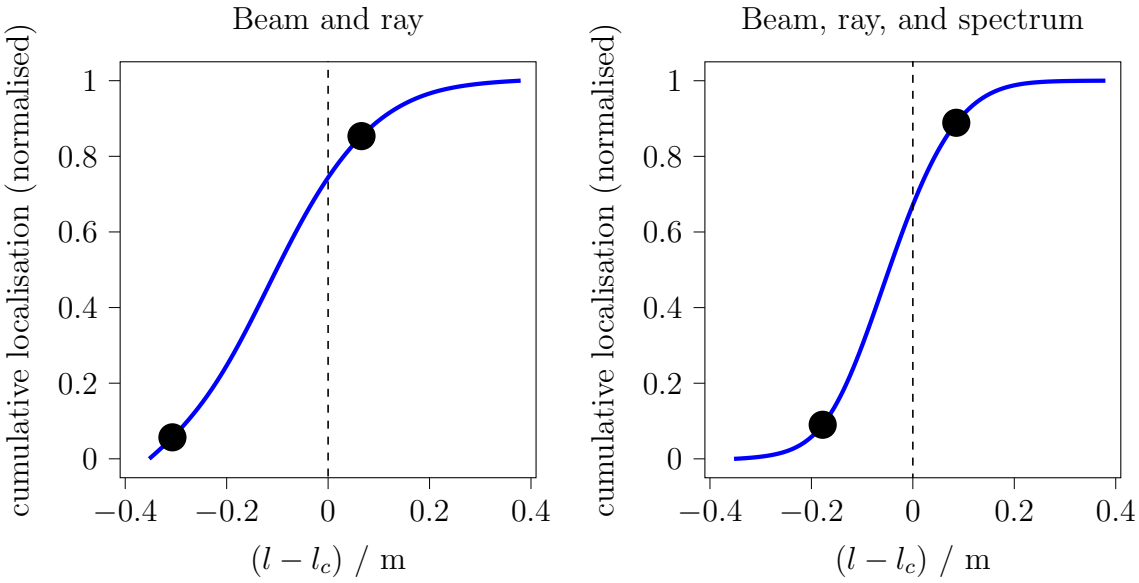

Figure 6.4: Here we show the cumulative integrals of localisation for the MAST test case, normalised such that it is 0 upon entering the plasma, and 1 when leaving. On the left, we look at the *beam* and *ray* pieces, and on the right, we include the *spectrum* piece as well. These pieces are shown as a function of arc length from the cut-off, $l - l_c$. The vertical dashed line shows the location of the cut-off. The two black points in each figure correspond to that of Figure 6.1 (right) and Figure 6.2 (right), indicating the start and end of 80% range, which gives where most of the backscattered signal comes from.

Chapter 7

Wavenumber resolution

The wavenumber resolution is different for $k_{\perp,1}$ and $k_{\perp,2}$. The calculation of the former follows from the previous section on localisation, while that of the latter is simply given by equation (5.25). Consequently, this section is split into two parts, discussing the $k_{\perp,1}$ and $k_{\perp,2}$ resolutions in turn.

7.1 $k_{\perp,1}$ resolution

The $k_{\perp,1}$ resolution, $\Delta k_{\perp,1}$, cannot be divorced from the localisation, Chapter 6. Nonetheless, one may consider it insightful to calculate it. In this section, we show how this can be achieved.

Since the *ray* piece as a function of backscattered $k_{\perp,1}$ diverges at cut-off, namely at $k_{l,1} = -2K(l_c)$, one might wrongly suspect that the dominant backscattered $k_{l,1}$ comes from the cut-off as well. To properly deal with this divergence, which is integrable, we instead consider the cumulative integral of the *ray* piece. We show this in Figure 7.1 (bottom). As we can see from the figure, the median backscattered $k_{\perp,1}$ is not exactly that of the cut-off, regardless of whether we use the spectrum piece or not. The divergence means it is not particularly insightful to calculate and plot the localisation, the integrand of equation (5.27), to find the backscattered $k_{\perp,1}$ resolution. Instead, we directly take a cumulative integral of the localisation piece, and calculate the resolution from there, see Figure 7.1.

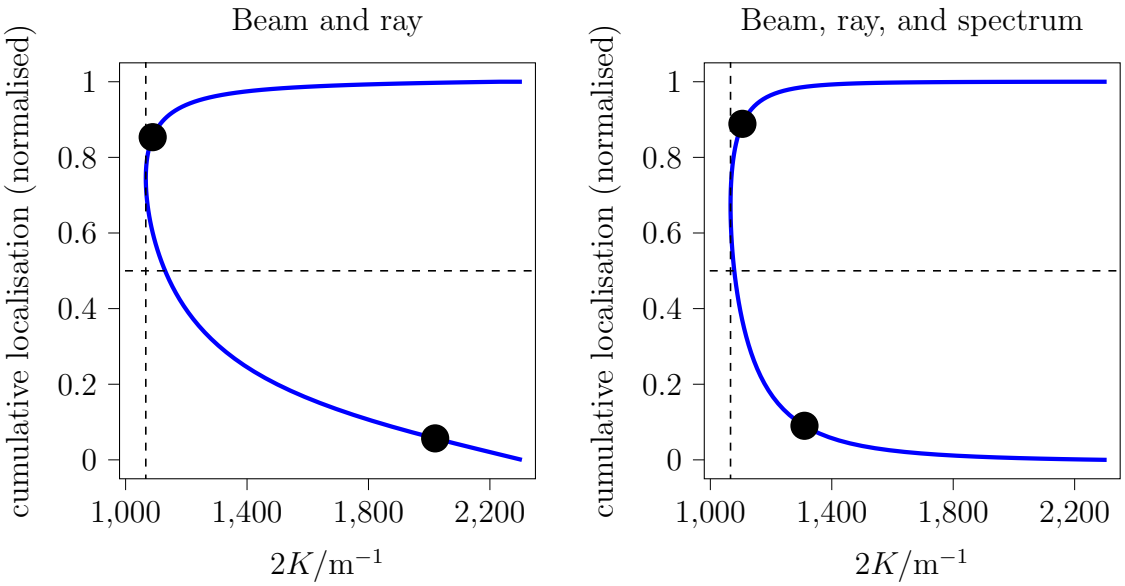

Figure 7.1: Here we show the normalised cumulative integrals of localisation as a function of backscattered $k_{\perp,1} = -2K$ (given by the Bragg condition) for the MAST test case. On the left, we look at the *beam* and *ray* pieces, and on the right, we include the *spectrum* piece as well. The start and end of the 80% range are marked on the graphs. The vertical dashed line indicates the backscattered $k_{\perp,1}$ at the cut-off. Note that the derivatives are infinite at the cut-off, but the plots themselves do not diverge, showing that the localisation piece is indeed integrable. The backscattered $|k_{\perp,1}|$ at the cutoff is $1070\mathrm{m}^{-1}$, while the values of $|k_{\perp,1}|$ at the ends of the 80% range are $2020\mathrm{m}^{-1}$ and $1090\mathrm{m}^{-1}$ (left) and $1310\mathrm{m}^{-1}$ and $1110\mathrm{m}^{-1}$ (right). The intersection of the horizontal dashed lines and the curves give the median backscattered $k_{\perp,1}$.

7.2 $k_{\perp,2}$ resolution

To understand the width of the Gaussian, $\Delta k_{\mu,2}$, we first consider a simple case with $M_{xy,\mu} = 0$. Then, $M^{-1}_{yy,\mu} = 1/M_{yy,\mu}$. Remembering that $M_{yy,\mu} = \Psi_{yy,\mu}$ exactly, and using the definitions given by equations (2.10) and (2.11), we find that equation (5.25) gives

$$\Delta k_{\mu,2} = \frac{2\sqrt{2}}{W_{y,\mu}} \left[1 + \frac{1}{4} K^2_\mu W^4_{y,\mu} \left(\frac{1}{R_{b,y,\mu}} \right)^2 \right]^{1/2} . \tag{7.1}$$

This recovers the widely-used expression for the wavenumber resolution for a circular beam in a slab. We do not see the corrections due to the curvature of the magnetic field lines or the magnetic shear in equation (7.1) because we have taken $M_{xy,\mu} = 0$. As useful as this might have been to gain some physical insight, in general, we cannot neglect $M_{xy,\mu}$. The corrections due to curvature and shear of the magnetic field are therefore important. These corrections affect the wavenumber resolution in a way that in general cannot be easily further simplified. Hence, one has to use equation (5.25) in its presented form to determine the wavenumber resolution. We now apply our full model, equation (5.25), to our MAST test case, Figure 7.2. By noticing the difference between the solid and dash-dot lines in the figure, one sees that the corrections indeed significantly affect wavenumber resolution.

In our model, the curvature of the cut-off surface does not affect the wavenumber resolution at all. One can understand this as follows. Physically, it is the curvature of the field lines and the magnetic shear that are important, since the beam is scattered off the turbulent fluctuations perpendicular to the field lines. The beam is not scattered from the cut-off surface per se — hence, strictly speaking, it is not the curvature of the cut-off surface that is important, as previously argued [3, 25].

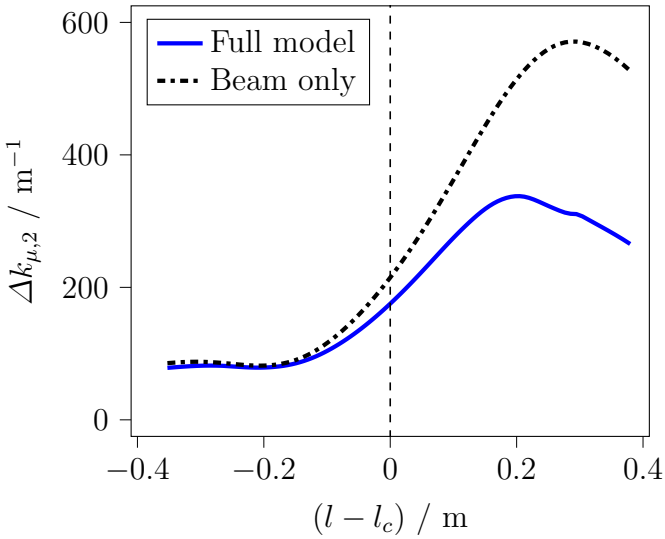

Figure 7.2: Wavenumber resolution for $k_{\perp,2}$ as a function of distance from the cut-off along the central ray $l - l_c$ for our MAST test case. The solid blue line includes the corrections arising from curvature and shear of $\hat{\mathbf{b}}$, while the dash-dot black line does not have these corrections, and only uses the beam properties.

Chapter 8

Mismatch

The backscattered spectral density decays exponentially with mismatch, since we have $p_r \propto \exp[-2\theta_{m,\mu}^2/(\Delta\theta_{m,\mu})^2]$, where $\Delta\theta_{m,\mu}$ is given by equation (5.24). This is consistent with our choice to take the mismatch angle to be small, such that the backscattered signal is large enough to detect.

8.1 Understanding mismatch attenuation

Like we did with the wavenumber resolution, we take $M_{xy,\mu} = 0$ to simplify the expression in order to gain some physical insight, getting

$$\Delta\theta_{m,\mu} = \frac{1}{K_\mu}\left[-\mathrm{Im}\left(\frac{1}{M_{xx,\mu}}\right)\right]^{-1/2}. \tag{8.1}$$

We write this out in full, to get

$$\Delta\theta_{m,\mu} = \frac{\sqrt{2}}{W_{x,\mu}K_\mu}\left[1 + \frac{W_{x,\mu}^4 K_\mu^2}{4R_{b,M,\mu}^2}\right]^{\frac{1}{2}}, \tag{8.2}$$

where we use the shorthand

$$\frac{1}{R_{b,M,\mu}} = \frac{1}{R_{b,x,\mu}} + \left(\hat{\mathbf{b}}\cdot\nabla\hat{\mathbf{b}}\cdot\hat{\mathbf{g}}\right)_\mu. \tag{8.3}$$

It has been reported [30] that for high K, the backscattered signal's amplitude is especially sensitive to the toroidal steering angle. This can be explained by mismatch. At a given finite mismatch angle, the attenuation due to mismatch is larger at larger K_μ, as seen from equation (5.24) and from Figure 8.1. Indeed, for

$$K_\mu \gg \frac{2R_{b,M,\mu}}{W_{x,\mu}^2}, \tag{8.4}$$

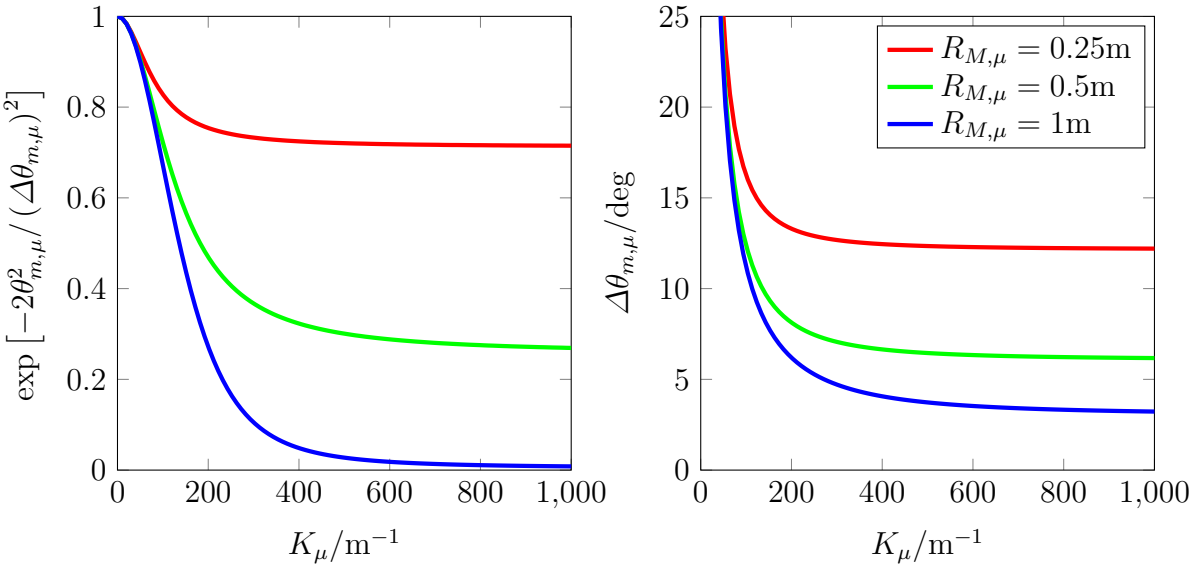

Figure 8.1: How beam parameters at the scattering location influence the attenuation due to mismatch. We do not use beam tracing for these graphs; instead, we vary the beam properties by hand and see what happens. Here, we have $1/R_M = 1/R_x + \hat{\mathbf{b}}\cdot\nabla\hat{\mathbf{b}}\cdot\hat{\mathbf{g}}$, $M_{xy} = 0$, $W_x = 7.5\mathrm{cm}$, and $\theta_m = 5°$. The line colours correspond to the same R_M for both graphs.

equation (8.2) reduces to

$$\exp\left[-2\frac{\theta_{m,\mu}^2}{\left(\Delta\theta_{m,\mu}\right)^2}\right] \approx \exp\left(-\theta_{m,\mu}^2\frac{4R_{b,M,\mu}^2}{W_{x,\mu}^2}\right), \tag{8.5}$$

at which point further increasing K_μ has no effect on the mismatch attenuation. These considerations are especially important when designing DBS systems with no toroidal optimisation; there will be a finite mismatch over many of the channels, and this will be more problematic at larger wavevectors. Understanding mismatch attenuation will help one to mitigate this issue.

We proceed to apply the unsimplified expression for mismatch attenuation, equation (5.24), to a real tokamak, Figure 8.2. We have taken there to be a 1.1° systematic error in the toroidal launch angle of the beam, which roughly corresponds to a $\sim 2°$ error in the mismatch at the cut-off $\theta_{m,c}$. This error is within the bounds of the offset required in previous work [30]. In Section 9.1.3, we show that this error can be properly accounted for if one were to carefully convert the mirror rotation angles into beam launch angles.

The beam and equilibrium plasma properties account for the experimentally-observed mismatch attenuation, and not backscattering from some $k_\parallel$ (which we neglect in our

model). This preliminary analysis of MAST data is a good proof of concept — we now understand, and are able to calculate, how mismatch attenuates the DBS signal. A more detailed analysis of the other channels (different frequencies) and other times will be performed in Chapter 9, which will enable us to better evaluate our model for use in real plasmas. This advancement means that we can now operate DBS in regimes where the mismatch is small, but not so small as to be negligible (as was required previously). New insights can thus be gained from existing data, and new experiments can be performed with less strict tolerances.

8.2 Simultaneous optimisation of mismatch optimisation and wavenumber resolution

A point of considerable interest is that the optimisations of both $k_{\perp,2}$ wavenumber resolution and mismatch attenuation have opposite requirements. To gain intuition, we consider the simplified case for $M_{xy,\mu} = 0$, where the associated mismatch attenuation is given in equation (8.2) and the $k_{\perp,2}$ wavenumber resolution in equation (7.1). When designing a DBS system, one would want to maximise resolution (minimise $\Delta k_{\mu,2}$) and minimise mismatch attenuation (maximise $\Delta\theta_{m,\mu}$). Hence, to optimise both simultaneously, one would need an elliptical beam.

We examine how the $-\mathrm{Im}\,(1/\Psi_{\alpha\alpha})$ piece behaves in vacuum and answer the question of whether it is larger at or far from the beam waist. The answer is not obvious. Consider the following example. The intuitive reason why the backscattered power is nonzero when there is a mismatch is because there is a spread in $\mathbf{K}$ due to the width and curvature of the beam. Specifically, we see that only the width and curvature in one direction matters, $\Psi_{xx,\mu}$. To maximise the aforementioned spread, we want very curved wavefronts (small $R_{x,\mu}$) and narrow beams (small $W_{x,\mu}$). The dependence on beam curvature means we want to be far from the waist, while the dependence on width means we want to be at the waist. Conversely, the wavenumber resolution, which depends on $\Psi_{yy,\mu}$, benefits from the low curvature near the waist, but from the larger beam widths far from the waist.

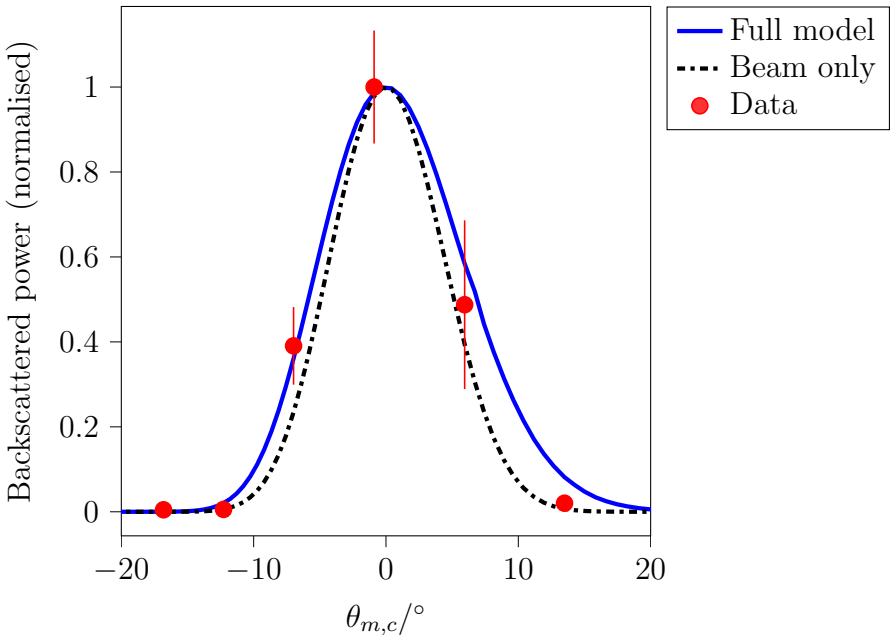

Figure 8.2: Red points indicate DBS data from repeated shots, where only the toroidal launch angle was varied [30]. We have taken there to be a 1.1° systematic error in the toroidal launch angle of the beam, which roughly corresponds to a $\sim 2^\circ$ error in the mismatch at the cut-off $\theta_{m,c}$. This error is within the bounds of the systematic offset required in previous work [30]. In Section 9.1.3, we show that this error can be properly accounted for if one were to carefully convert the mirror rotation angles into beam launch angles. The data points shown here are from similar flux surfaces, but at different mismatch angles. Hence, the attenuation that we see is mainly from the mismatch, since we expect the turbulent fluctuations to be largely the same. The solid blue line indicates the model's predicted attenuation due to mismatch, $\exp\left[-2\theta_{m,c}^2/\left(\Delta\theta_{m,c}\right)^2\right]$, given the beam properties at the cut-off when we launch the beam at various toroidal angles. The dash-dot black line shows the attenuation but with $\Delta\theta_{m,c}$ calculated from $\boldsymbol{\Psi}_w$ instead of $\boldsymbol{M}_w$, that is, calculated only from the beam properties without the corrections arising from the curvature and shear of $\hat{\mathbf{b}}$.

In fact, in vacuum, it can be shown that a elliptical beam satisfies

$$-\mathrm{Im}\left(\frac{1}{\Psi_{\alpha\alpha}}\right) = \frac{2}{W^2_{\alpha,waist}}, \tag{8.6}$$

at all points along the beam. Here, $\Psi_{\alpha\alpha}$ are the eigenvalues of $\boldsymbol{\Psi}_w$. Hence, it does not matter where we are along the beam nor where is the beam waist, the only important thing is the beam waist's width. We would want a narrower waist to optimise wavenumber resolution, and a wider waist to optimise mismatch attenuation. In order to reconcile these seemingly contradictory requirements, one could imagine using an elliptical Gaussian beam to simultaneously optimise widths in the relevant directions.

Despite the intuition that considering beams in vacuum may give us, the evolution of $\boldsymbol{\Psi}_w$ is ultimately more complicated in a plasma. This is one reason why using beam tracing is important. In Figure 8.3, we see that the beam in the plasma can indeed be quite different from what one would expect from vacuum propagation; the beam curvature goes to zero at two points, and neither of them are where the beam widths are at a minimum. Thus, the notion of a beam waist, where the widths are at a minimum and the wavefront curvatures are zero simultaneously, is not properly achieved to begin with. This insight is a demonstration of the strength of our model.

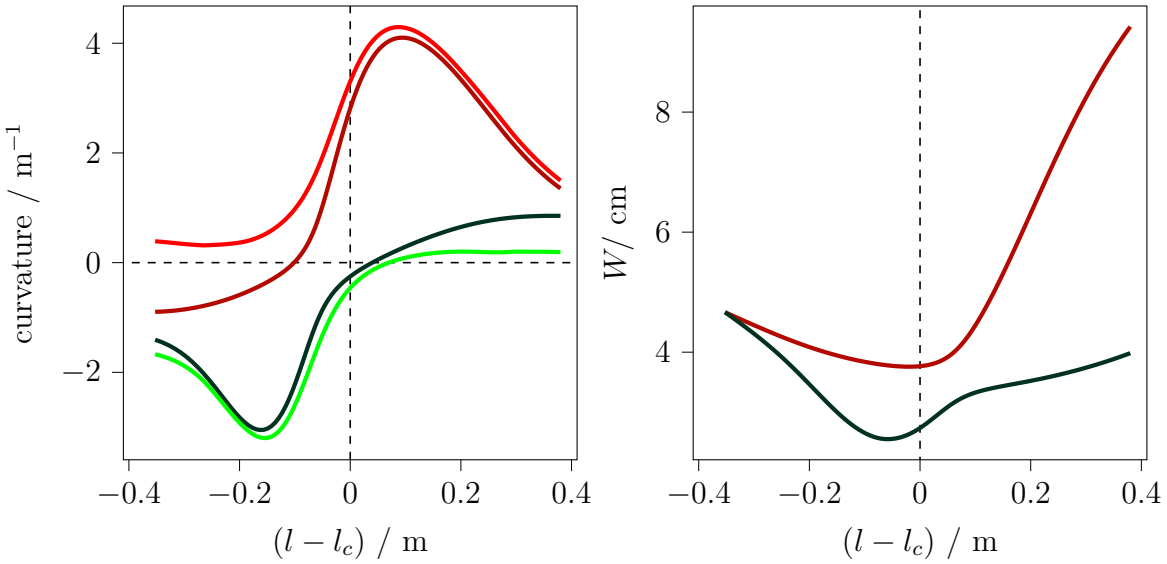

Figure 8.3: MAST test case, with launch parameters $R_{b,x} = R_{b,y} = -1.79$m, $W_x = W_y = 9.47$cm. Evolution of curvatures $1/R_b$ (left, dark green and dark right) and widths (right) along the beam, calculated from the diagonalised real and imaginary parts of $\boldsymbol{\Psi}$ respectively. The effective curvatures $1/R_{b,M}$ (left, bright green and bright red) are calculated from the diagonalised real part of $\boldsymbol{M}$. Note that in general, the directions of the principal widths, curvatures, and effective curvatures are not in the same direction. Here we plot the curvatures $1/R_b$ and $1/R_{b,M}$ rather than the radii of curvature R_b and $R_{b,M}$ to avoid a divergence. We remind readers that R_b is calculated from the real part of $\boldsymbol{\Psi}_w$, and analogously, $R_{b,M}$ is calculated from the real part of $\boldsymbol{M}_w$. At the point the beam enters the plasma (when these plots start), the principal curvatures are not the equal to each other, despite us launching a circular beam, because we have applied the vacuum-plasma boundary conditions, as described in Appendix A. Recall that $l - l_c$ is the distance along the central ray from the cut-off location.

Chapter 9

Experiment

Up until this point, we had illustrated the different parts of the beam model by looking of one of two test cases, as outlined in Section 2.2.2. In this chapter, we seek to rigorously compare the beam model to experimental data, over a range of frequencies and equilibria, enabling us to ascertain the applicability of the beam model to fusion experiments. We begin by detailing the MAST shots relevant to this thesis and how experimental data is processed, Section 9.1. Next, we have the key results of this chapter: we evaluate the effectiveness of the beam model in quantitatively accounting for the mismatch attenuation and its effect on localisation, Section 9.2.

9.1 Analysis of experimental data

9.1.1 Shot parameters

To evaluate our model, we study repeated shots from MAST where DBS data was available. By repeated shots, we mean groups of shots where the equilibria were similar, but the launch angle of the DBS diagnostic was varied. For clarity, we split our shots into three distinct groups. The second group is further divided into 2A and 2B, with slightly different neutral beam powers. The neutral beams in the third group's shots were not particularly reliable, with different beams failing at different times for the different shots. Two additional such groups were excluded from this work because the DBS launch angles were not varied systematically, making analysis rather convoluted. Shots from all three groups were studied.

Shot group 1 29904, 29905, 29906, 29908, 29909, 29910

Shot group 2A 29677, 29678, 29679, 29681, 29683, 29684

Shot group 2B 29692, 29693

Shot group 3 30142, 30143, 30144, 30145, 30146, 30147

All the shots in group 1 were repeated shots, with the same equilibrium. The shots in group 2 were also repeated shots (up to 230ms), but the neutral beam power for 2A was slightly higher than that of 2B [30]. We reproduce the equilibrium data from a previous work [30] here, with additional data from shot groups 2 and 3, to show the extent to which shots from a particular group are similar in Figure 9.1.

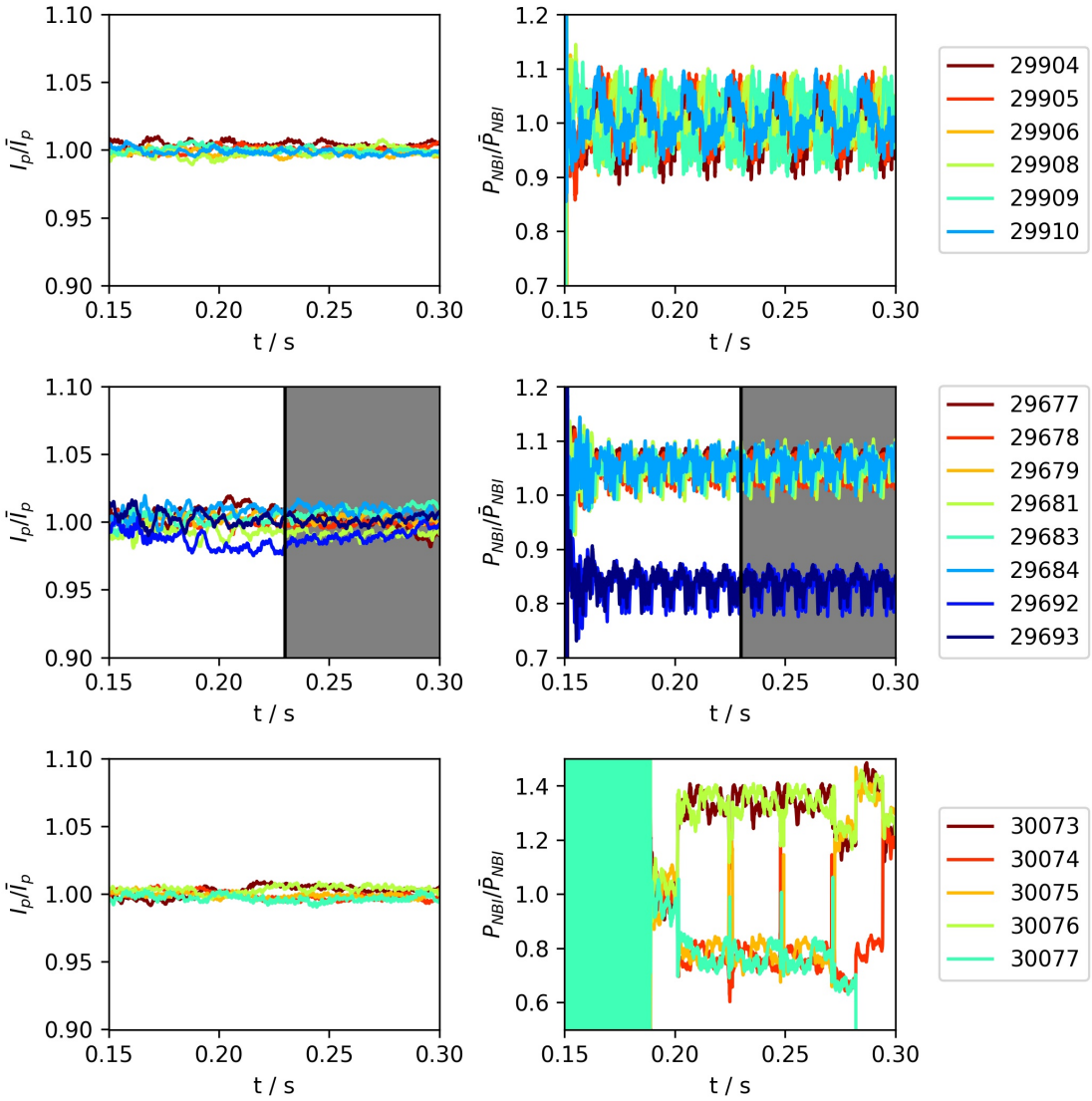

Figure 9.1: Shot group 1 (top), shot group 2 (middle), shot group 3 (bottom). Plasma current (left) and total NBI power (right), normalised to their respective means (averaged over all shots from each group). Different resonant magnetic perturbations were applied after 230ms for shot group 2, and hence that region is greyed out. In shot group 3, the neutral beams were only turned on later into the shot, explaining the noise at early times.

Shot group 1		
Shot number	φ_{rot}	φ_{tilt}
29904	$-4°$	$-4°$
29905	$-5°$	$-4°$
29906	$-6°$	$-4°$
29908	$-3°$	$-4°$
29909	$-2°$	$-4°$
29910	$-1°$	$-4°$
Shot group 2		
Shot number	φ_{rot}	φ_{tilt}
29677	$6°$	$1°$
29678	$4°$	$1°$
29679	$5°$	$1°$
29681	$3°$	$1°$
29683	$2°$	$1°$
29684	$1°$	$1°$
29692	$2°$	$1°$
29693	$2°$	$1°$
Shot group 3		
Shot number	φ_{rot}	φ_{tilt}
30073	$-4°$	$-4°$
30074	$5°$	$4°$
30075	$4°$	$4°$
30076	$3°$	$4°$
30077	$2°$	$4°$

Table 9.1: Summary of shots examined in this chapter, together with the DBS mirror angles used.

The bulk of the analysis of this chapter will focus on shot group 1, which we analyse at 10ms intervals from 160ms to 250ms. This group had the most repeated shots, and the launch angles of the DBS system covered a wide range of conditions, sufficient to show that the backscattered signal peaks at zero mismatch, at least in the right conditions.

The MAST DBS was set up in such a way that the V band and Q band launch polarisations were orthogonal. The majority of DBS measurements done in MAST were configured for X-mode Q band and O-mode V band. Shot group 3 is unique because it is a series of repeated shots where the polarisation for the bands were the

other way round (O-mode for the Q band). For any given frequency, the O-mode typically penetrates deeper into the plasma than the X-mode. Hence, for shot group 3, the lowest frequency of the V band and the highest frequency of the Q band had very similar paths. For completeness, we briefly look at data from shot group 3 later in this chapter.

9.1.2 Magnetic equilibria and density profiles

In order to determine the equilibrium dielectric tensor $\boldsymbol{\epsilon}_{eq}$, we need to know the electron density $n_e(\mathbf{r})$ and magnetic field $\mathbf{B}(\mathbf{r})$, both as functions of position. This is made simpler by assuming toroidal symmetry. Hence, we only need to know these quantities as expressed in the poloidal plane, as a function of R and Z. We use EFIT [71, 72], constrained by the motional Stark effect diagnostic [73] when possible, to determine the normalised poloidal flux and the toroidal magnetic field $\mathbf{B}_\zeta$. On the other hand, the Thomson scattering diagnostic [74] gives density n_e along its laser. Using this, together with the poloidal flux from EFIT at the points along the Thomson scattering laser beam, we express density as a function of flux label $n_e(\psi_p)$. We use a fit for the density profile and smooth the EFIT output as described in Section 2.2.2.

One can now calculate the probe beam's electric field with beam tracing. In this work, we use our beam tracing code, Scotty, Section 2.2. Calculating the effect of mismatch only requires the beam parameters and some post-processing with our model, so one is not limited to using Scotty; any beam tracing code (such as Torbeam [51]) would do.

MSE-constrained EFIT was available for shot groups 1 and 2 (see Table 9.1), but not for shot group 3. To faciliate the current work, EFIT for shot group 3 was reran with pressure-constraints; however, without MSE (the south NBI was not on), the pitch angle for these shots are only reliable near the edge. As we will later see, important insight will be drawn from core measurements of shot group 2. Since the old MSE-constrained EFIT runs did not have good fits in the core, new MSE-constrained EFIT analysis was specially done for this paper, ensuring that the pitch angle in the core is indeed reliable.

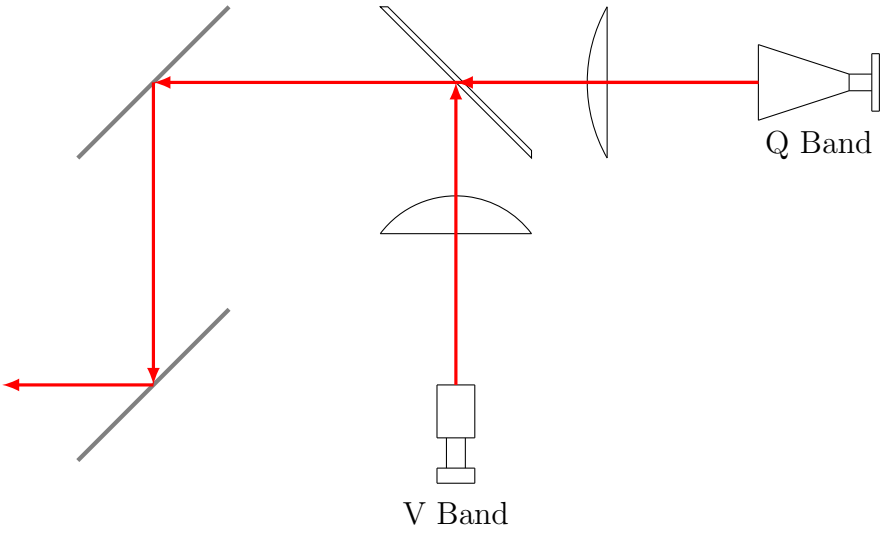

Figure 9.2: Simplified 2D schematic of the horns, lenses, polariser, and mirrors. The Q band beam is transmitted through the polariser, while the V band beam is reflected off it; this is why the polarisation of the two bands are always orthogonal to each other. The polariser is adjusted such that one band is in O-mode and the other X-mode. The last mirror here is the steering mirror, which appears in Figure 9.3. For a 3D view of the experimental layout, refer to Figure 6 of previous work on the MAST DBS [30].

9.1.3 Geometry of DBS hardware

There were two horns, one for the Q band (30GHz–50GHz) and the other for the V band (55GHz–75GHz). Both of these horns had their own focusing lenses, Figure 9.2. After some other optics [30], the beams were incident, at the same angle, on a steering mirror. This mirror was used to control the poloidal and toroidal launch angles of the beam. It is important to realise that the mirror angles, which we call rotation φ_{rot} (left and right) and tilt φ_{tilt} (up and down), are related to the Scotty (as well as other codes, like Torbeam and Genray) launch angles by a 3D transformation. A positive φ_{tilt} corresponds to the normal of the mirror pointing towards the sky (and negative corresponds to pointing towards the ground). The sign convention for φ_{rot} is given in Figure 9.3. When $\varphi_{rot} = 0$ and $\varphi_{tilt} = 0$, the beam is incident on the mirror at 45° and reflected at 45°, subsequently propagating in the midplane of the tokamak. However, $\varphi_{rot} = 0$ does not correspond to the beam being launched in the radial direction (straight toward the centre column); in this situation, the beam does not propagate towards the centre of the central column, but is displaced to the side

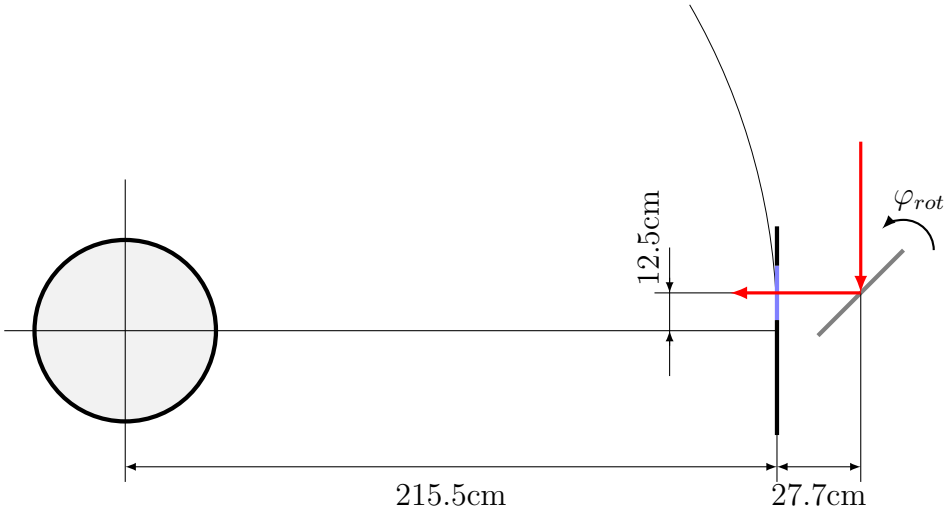

Figure 9.3: The steering mirror rotates around two axes, both of which pass through the point where the centre of the beam is incident on its surface. The angle φ_{rot} refers to the launch angle in the plane of the diagram, and φ_{tilt} adjusts the launch angle out of plane of the diagram. That is, they are related to the azimuthal and polar angles respectively. A positive φ_{tilt} corresponds to the normal of the mirror pointing towards the sky (and negative corresponds to pointing towards the ground). The sign convention for φ_{rot} is given in the diagram. In the diagram, we have $\varphi_{rot} = 0$ and $\varphi_{tilt} = 0$, such that the beam is incident at 45°, reflected at 45°, and propagates in the midplane of the tokamak. In this situation, however, the beam does not propagate towards the centre of the central column, but is displaced to the side by 12.5cm. The DBS was designed this way because the window was slightly offset to the side.

by 12.5cm, see Figure 9.3. Those wishing to analyse data from the old MAST DBS would do well to take meticulous care to ensure that all the above issues are properly accounted for.

The hardware was such that the polarisations of the beams from the two horns were always perpendicular to each other. These polarisations were optimised such that one horn would launch an O-mode beam, and the other an X-mode beam. Here the O-mode refers to the polarisation being parallel to the magnetic field upon entering the plasma, and the X mode refers to the polarisation being perpendicular to the magnetic field upon entry. Unfortunately, both of the more detailed parameter scans on MAST (shot groups 1 and 2) were done with the Q band in X-mode and the V band in O-mode. As such, the O-mode measurements were typically deeper in the core and the X-mode measurements closer to the edge for these two shot groups.

9.1.4 Beam parameters

The DBS system had eight Q band channels, as well as eight V band channels. However, for the shots studied, the highest frequency V band channel (75GHz) was not digitised. The beam width as a function of distance from the lens was measured for three different frequencies: 35GHz, 44.5GHz, and 50GHz (Q band), and no frequency-resolved measurements were performed for the V band. As such, we estimate the beam parameters based on the properties of the antennae.

The Q band antenna was a smooth conical horn. Since the electric field is perpendicular to the surface of conductors, we can estimate the wavefront curvature at the aperture of the antenna. The beam width at the aperture was estimated from the horn's geometric properties, using data from a lookup table [66]. The V band antenna was a corrugated conical horn. We estimate the beam waist to be located at the aperture of the antenna, and the size of the waist was calculated from the far-field divergence angle given in the horn's specifications. We then approximate the lenses as being thin and spherical. They thus modify the real part of $\boldsymbol{\Psi}_w$. Using vacuum propagation, we figure out what the beam properties are at the steering mirror, which is where the Scotty simulations begin. A more detailed account is given in Appendix E.

Admittedly, the best way to determine the initial beam parameters would simply be to measure them, especially since the beam pattern is not Gaussian until a significant distance from the horns, and the lenses are thick and aspherical. Since it is no longer possible to measure these parameters in the original system, we make do.

9.1.5 Spectral analysis of DBS signal

We use Welch's method of averaged periodograms [75] to calculate the spectral density, weighted with Hann windows [76] and using a 50% overlap. This method involves dividing a time period into equal segments, applying a Hann window to each of them, individually Fourier transforming them, and then finding the mean spectral density at every given frequency. The standard deviation is then used to estimate the associated standard error of the mean. In this work, we average over 101 segments. Each segment

spans 0.1024ms, which gives us a total of 5.2ms, since any two adjacent segments overlap. We then smooth the spectrum. The smoothing process works as follows. We consider a moving window of 5 points, discard the highest and lowest points, and then take the mean of the remaining 3 points. This is essentially a moving trimmed average.

DBS spectra are typically formed of two peaks: one centred at zero frequency, with the other at some Doppler-shifted frequency, see Figure 9.4. The latter is believed to contain the useful backscattered signal, while the former is thought to be a spurious contribution [77]. Hence, one tries to remove the zero-frequency peak, and analyse the Doppler-shifted peak. This enables one to find the Doppler shift and backscattered power of the signal. The Doppler shift is generally of interest as it sheds light on the velocity profile of the plasma. However, in this study, we are not interested in the frequency of this shift, and fitting the data is difficult because the Doppler-shifted peak is often asymmetric and broad; instead, we focus on the backscattered power. Consequently, the analysis procedure may be significantly simplified compared to that of previous work [30]. We find the total backscattered power at both positive and negative frequencies, and subtract the latter from the former, getting what we call the antisymmetric backscattered power (see Figure 9.4, left).

However, the zero-frequency peak is sometimes known to be slightly asymmetric, which would contribute spuriously to the antisymmetric backscattered power. As such, we compare this power with similar calculations where the spectral power at low Doppler shifts was ignored (see Figure 9.4, right). This was done for two cases: ignoring the spectral power when $|\omega| < 150$kHz and $|\omega| < 500$kHz. We find that these two method give similar results when the signal is localised near the cut-off, but different results otherwise; where this localisation away from the cut-off is discussed in Section 9.2.1. The larger the range of ω neglected when calculating the total backscattered power from spectral density, the closer the signal has to be localised near the cut-off for the results to give the same trends as the unadulterated antisymmetric backscattered power. This implies that there is a larger Doppler shift when the signal is localised near the cut-off, and a smaller shift when it is away from the cut-off. As a final check whether using the antisymmetric power to estimate the backscattered signal is comparable to more sophisticated techniques detailed in previous work [30], we compare

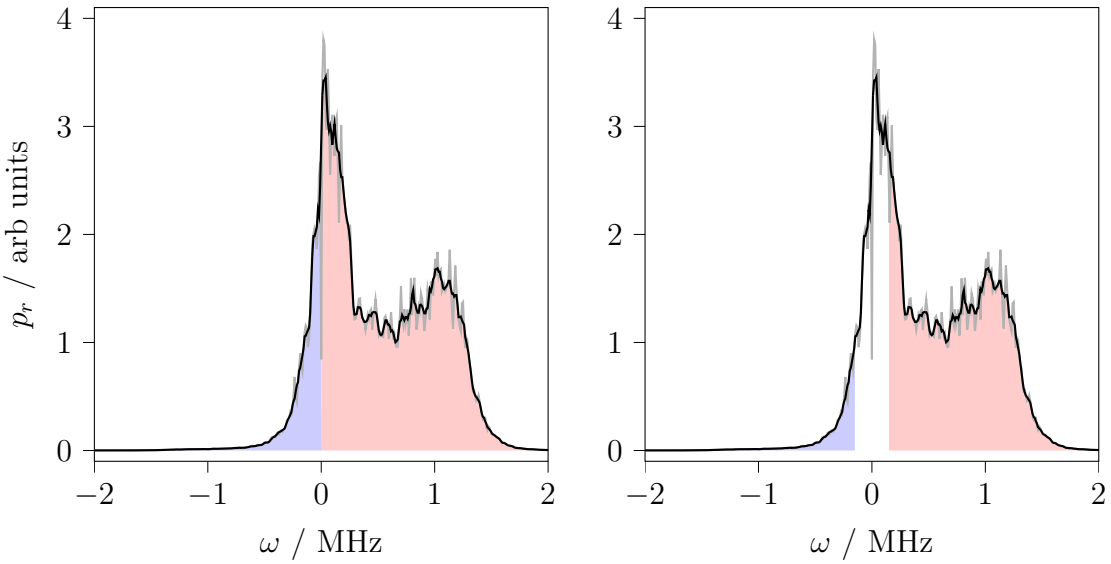

Figure 9.4: Welch periodogram (grey line) and smoothed spectrum (black line) for shot 29910, 55GHz channel, at 220ms. We calculate the signal by subtracting the blue area from the red area (left). This is compared with similar calculations where the spectral power at low Doppler shifts was ignored (right). We find that these two method give similar results when the signal is localised near the cut-off, but different results otherwise.

them in Figure 9.5. We find that the antisymmetric backscattered power is indeed a good estimate of the backscattered signal.

9.2 Mismatch attenuation

Here we discuss how effective our model is at predicting the effect of mismatch attenuation. Our approach is as follows. For a given frequency at a given time, there are six repeated shots (at least in shot group 1), launched at different angles φ_{rot}. We process the DBS data, determining the Doppler-shifted backscattered power for each of the repeated shots. The six backscattered powers are normalised to the maximum of the set, and then plotted as a function of rotation angle. The underlying assumption is as follows: when the backscattered power is maximal, the mismatch angle at the cut-off is probably small, and hopefully close to zero. Obviously, this is not usually the case, but it turns out to be a useful enough approximation, as one will later see.

To compare with the data, we run a parameter sweep of the mirror rotation angle

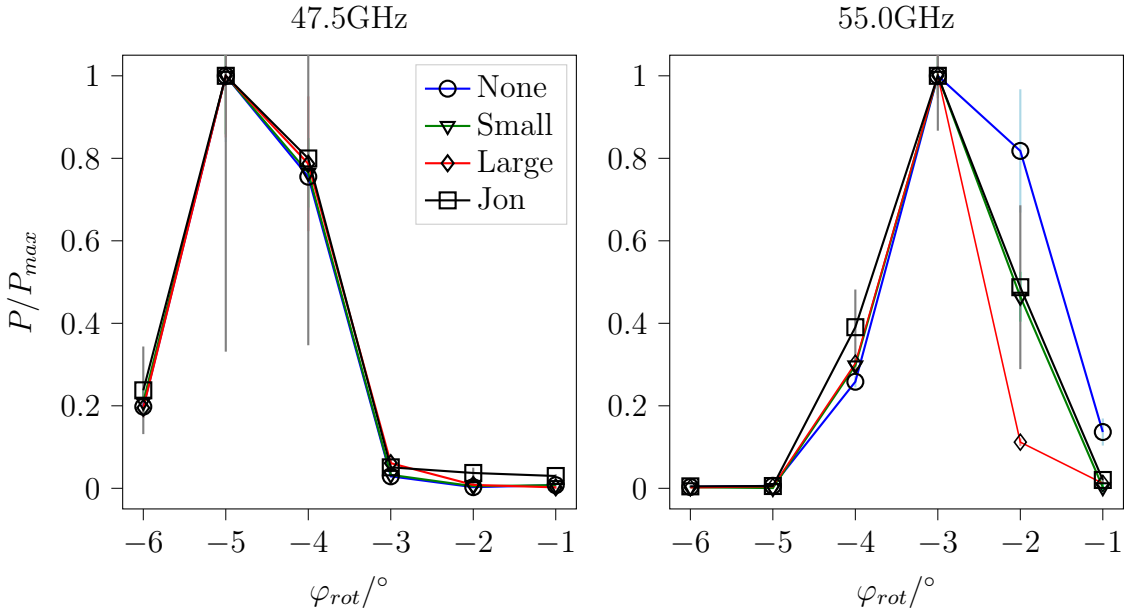

Figure 9.5: Calculated signal from antisymmetric backscattered power ('None'), antisymmetric backscattered power ignoring $|\omega| < 150$kHz ('Small'), antisymmetric backscattered power ignoring $|\omega| < 500$kHz ('Large'), and backscattered power calculated in earlier work ('Jon') [30]. All points in each series normalised to the maximum power of said series. These plots show that the antisymmetric backscattered power is a good estimate of the backscattered signal, for the purposes of our current work.

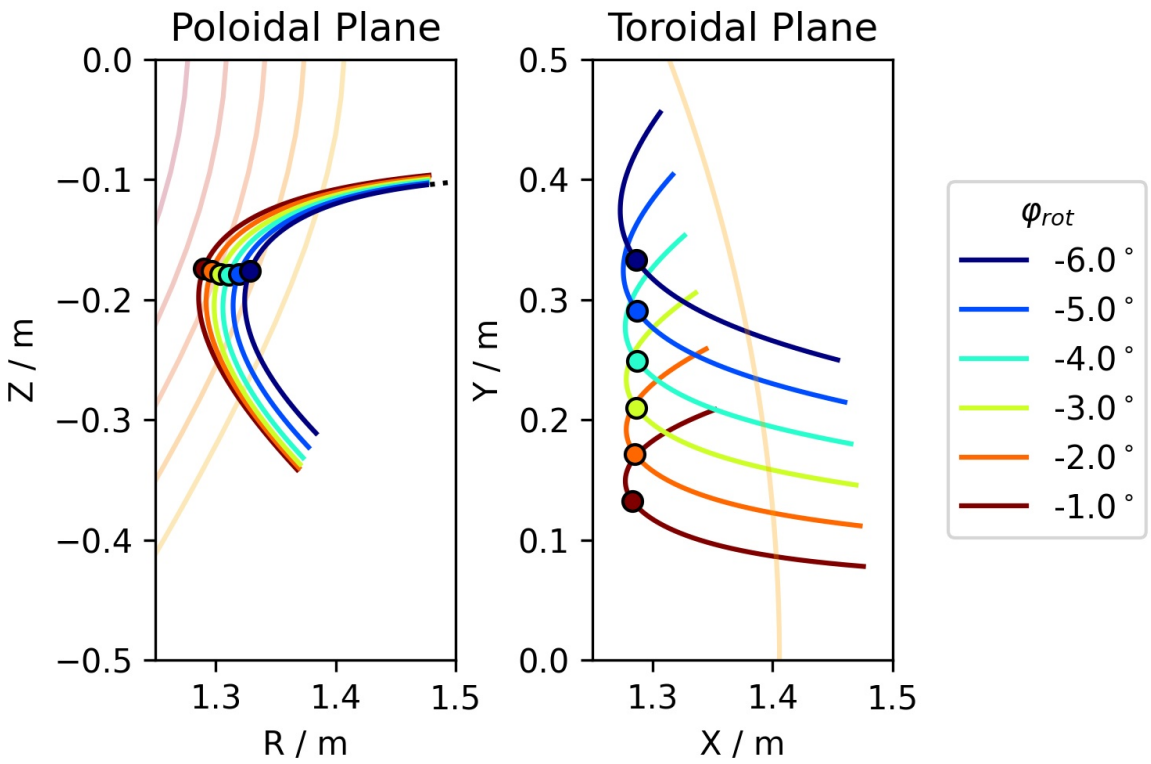

Figure 9.6: We show the trajectories of the 55GHz probe beam at 220ms. These beams are launched with different toroidal angles, and reach the cut-off at similar flux surfaces. For each ray, the circle marks the cut-off location, defined to be the point where the wavenumber K is minimised.

φ_{rot} in the beam-tracing code Scotty and plot the mismatch piece $\exp[-2(\theta_{m,c}/\Delta\theta_{m,c})^2]$ at the cut-off. Here cut-off is defined to be the point along the central ray where wavenumber K is minimised. One hopes that since different toroidal launch angles reach approximately the same cut-off surface, the density fluctuation would not have changed significantly (Figures 9.6 and 9.7). Thus, the difference in backscattered signals would be entirely due to the mismatch attenuation. Later on in this section, we see that this is a good approximation in some cases, but not in others.

We then calculate the various pieces of the localisation along the ray, given in Chapter 6. We remind readers that, in this thesis, the cut-off location refers to the point along the central ray where the beam wavenumber K is minimised, which is not necessarily at the turning point of the central ray. When K is minimised, both the ray and spectrum pieces are maximised. However, the beam and mismatch pieces have

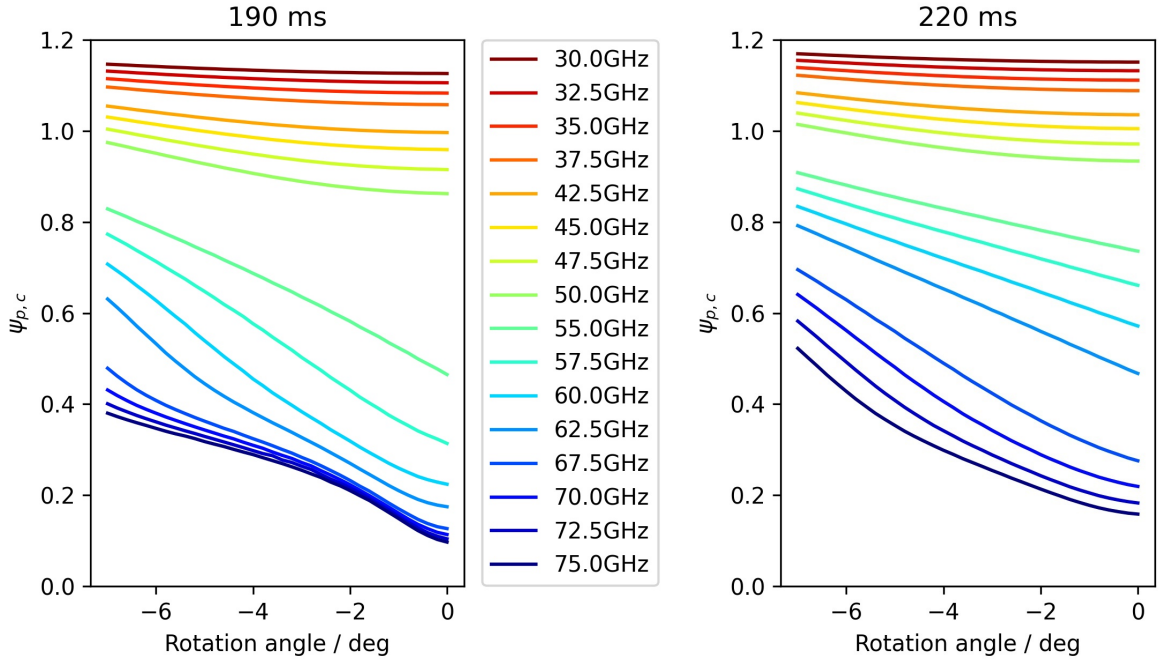

Figure 9.7: The normalised flux surface label at the cut-off for different frequencies and toroidal launch angles φ_{rot}, at 190ms and 220ms. The 55GHz line at 220ms (right) summarises Figure 9.6 (left).

their own dependence on position along the ray, which may result in the maximum of the total localisation piece not being at the cut-off. As such, in addition to the mismatch attenuation at the cut-off, we are also interested in the maximum value of the overall localisation along the ray, for a given launch angle. To illustrate these two quantities, we consider the equilibrium at 220ms of MAST shot 29908. We launch a beam at $\varphi_{rot} = 3°$ and show the various localisation pieces in Figure 9.8.

9.2.1 Comparison with data: V band

It is helpful to think of the V band frequencies as belonging to one of two categories, which we christened the *conventional* and *spherical* tokamak orderings in Chapter 4. In the *conventional tokamak* ordering, the mismatch angle is small along the path, $\theta_m \sim \lambda/W$, where λ is the wavelength of the beam and W its width, and so the signal is more-or-less localised to the cut-off location. This backscattered signal from the cut-off is attenuated by mismatch, which we determine with our model. In the *spherical tokamak* ordering, the mismatch angle is generally large along the beam $\theta_m \gg \lambda/W$,

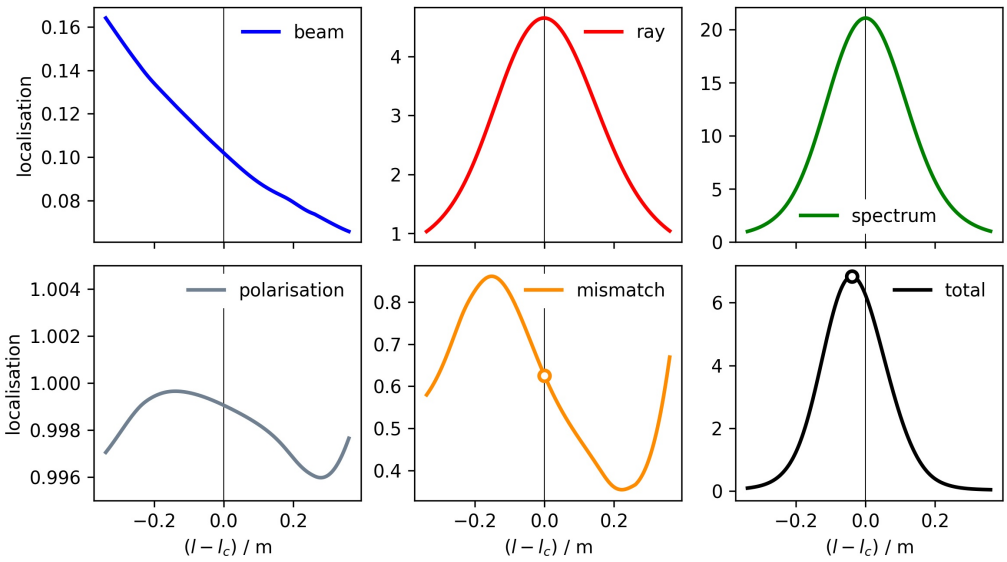

Figure 9.8: Localisation of the 62.5 GHz probe beams for shot 29908 at 220ms and $\varphi_{rot} = 3°$ as a function of arc length along the ray from the nominal cut-off location. The various pieces of the localisation, which when multiplied together, give the total localisation (bottom right). These contributions are plotted as a function of arc-length along the central ray from the cut-off location. Here localisation is the integrand in equation (5.39), which weigh the signal coming from various locations in the beam's path. The mismatch attenuation at the cut-off is indicated by an orange point (bottom middle), and the maximum total localisation by a black point (bottom right).

but is zero at some point, which may not be at the cut-off. The backscattered signal is localised to this point. We have chosen to present results at 220ms; the lower four V band frequencies more-or-less correspond to the *conventional tokamak* ordering, while the higher frequencies correspond to the *spherical tokamak* ordering. Now, recall that the characteristic width of the mismatch attenuation is a function of arc length along the central ray, $\Delta\theta_m(l)$. We use the mismatch attenuation at the cut-off (white-filled orange circle in Figure 9.8, lower row middle subplot) to plot the dash-dot lines in Figure 9.9, where this mismatch attenuation is calculated from $\Delta\theta_m(l_c)$ and $\theta_m(l_c)$. We see from Figure 9.9 that the mismatch attenuation at the cut-off accounts for the different signals for the lower frequencies. For the higher frequencies, the approximation that the backscattered signal comes from the cut-off location does not work so well.

We see that localisation of the DBS signal can be understood as having two different cases: the *conventional tokamak* and the *spherical tokamak*. The former case is what we typically think of when doing DBS, that the signal is localised to the cut-off, see Figure 9.10 (left). This is because the ray and spectrum pieces always localise the signal to the cut-off, by definition. The latter case is when the other localisation pieces conspire to move the dominant backscattering location away from the cut-off. The mismatch attenuation at the cut-off location being large shifts the point of maximum localisation elsewhere. Moreover, because of the diverging beam, the beam localisation piece is decreasing as the beam propagates. These two factors together mean that the signal is no longer localised to the cut-off, as shown in Figure 9.10 (right). Remember that *conventional tokamak* and *spherical tokamak* do not refer to all DBS measurements on such tokamaks, but rather, to their typical measurements if one does not put effort into optimising the launch angles.

9.2.2 Comparison with data: Q band

Analysis of the Q band data is more challenging. As we see from Figure 9.11, there is a systematic discrepancy between the experimental data and our model. We assume that there is some misalignment in the Q band optics that is equivalent to a systematic 2.5° error in the mirror angle. This accounts for the aforementioned discrepancy.

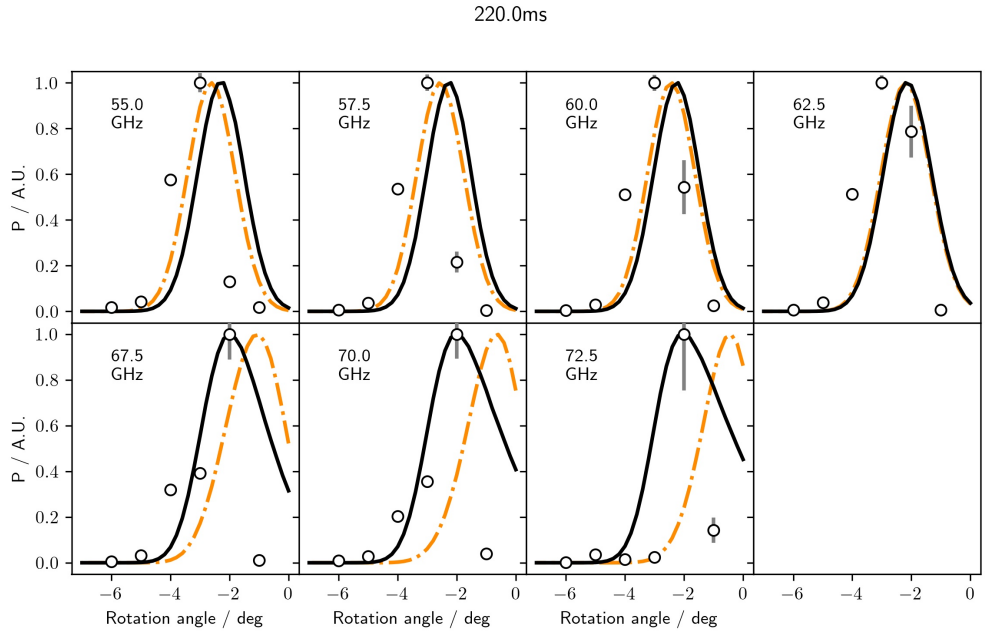

Figure 9.9: Comparison of experiment with the beam model for the V band frequencies. In each subplot, there are six black points; these show the experimental values of the backscattered power, normalised to the largest of the six points. The backscattered power was calculated as described in Section 9.1.5. The 75 GHz channel was not digitised for these shots, and is thus not shown. The dash-dot orange line shows the mismatch attenuation at the cutoff, given by $\exp[-2(\theta_{m,c}/\Delta\theta_{m,c})^2]$. The solid black line shows the maximum value of localisation for a given launch rotation angle, normalised to the maximum localisation in each subplot. These black and orange lines are calculated from the black and orange points at every launch angle in Figure 9.8. The experimental data (points) always follow the black line closely, and the orange line closely only for some frequencies, indicating that the signal is indeed localised away from the cut-off in some cases. Our model is able to accurately account for this effect.

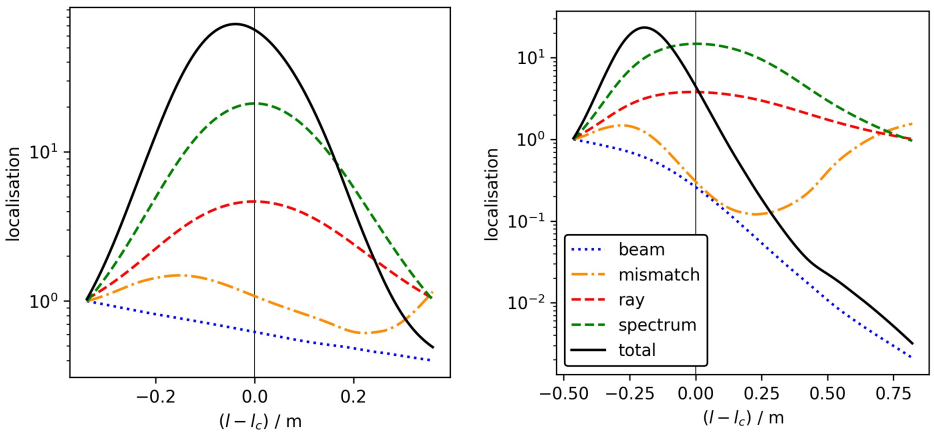

Figure 9.10: Localisation of the 62.5 GHz (left) and 67.5 GHz (right) probe beams at 220ms and $\varphi_{rot} = 3°$ as a function of arc length along the ray from the nominal cut-off location. In cases exemplified by the plot on the left, the backscattered signal mostly comes from the cut-off region (also shown in Figure 9.8). In other cases, the large mismatch at the cut-off causes the dominant backscattering location to be shifted to a region where there is less mismatch attenuation. For the MAST DBS, the diverging beam results in the beam localisation piece decreasing as the beam propagates. Hence, for longer paths, this piece also reduces the signal coming from the cut-off location. All pieces of the localisation have been normalised to their respective values at the point of entry into the plasma.

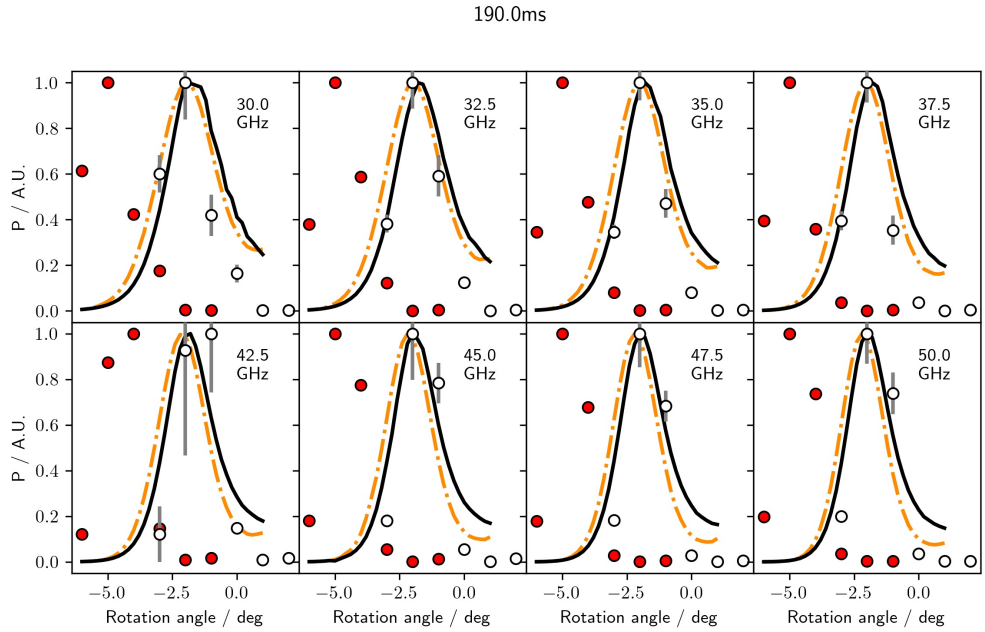

Figure 9.11: Data (red points), data assuming that there was a slight error in the launch angle (white points), model of the mismatch-attenuated backscattered signal from the cut-off (dash-dot orange line), model of backscattered signal (solid black line). In each subplot, there are six red points; these show the experimental values of the backscattered power, normalised to the largest of the six points. The white points are the same as the red points, but displaced to the right, accounting for the systematic error. For all frequencies shown here, the signal is fairly localised to the cut-off.

Since the lens had quite a short focal length, a slight $\sim$ 1mm transverse offset of the lens relative to the horn would already steer the beam enough to account for the 2.5° error. Alternatively, the Q band horn may simply not have been angled correctly. Analysis of shot group 2's Q-band also shows the same-sized offset as that in shotgroup 1. This offset is also consistent with results from shot group 3.

9.3 Outlook

In this chapter, we demonstrate that the beam model is able to quantitatively determine the mismatch attenuation, which is crucial for interpreting the DBS signal. This paves the way for accounting of mismatch attenuation in all future DBS studies. Even more interestingly, we show that mismatch attenuation can significantly affect localisation of the backscattered signal, moving the point of maximal backscattering away from

the nominal cut-off location. This is a testament to the predictive power of the beam model of DBS.

Chapter 10

Future work

Further work on the topic of this thesis can be characterised as belonging to one of two broad categories: deepening our understanding of the beam model of DBS and expanding the beam model to other techniques. With such developments, not only will we be able to better understand the data we get, but hopefully we will also be able to use microwave diagnostics to measure what they previously could not.

The beam model's ability to account for the MAST DBS backscattered signal for the series of repeated shots studied shows its utility and applicability to real systems. However, the repeated shots were carried out with a rather coarse toroidal launch angle sweep, and there was no poloidal launch angle sweep at all. Evaluation over a wider range of launch conditions and plasmas would help to further validate the model.

The ability of beam tracing to approximate the electric field of the probe beam near the cut-off was investigated in slab geometry some years ago [57]. This work showed that beam tracing was a good approximation for that geometry. It would be suitable, as due diligence, to extend that comparison to tokamak geometry, and compare full-wave to beam tracing. Conversely, one could run full wave codes in the appropriate limit to validate them in the beam tracing limit.

The beam model also has yet-untapped prospective of being used as a synthetic diagnostic, bridging the gap between gyrokinetic simulations and experimental measurements. In this respect, there is scope for leveraging our beam-tracing code, Scotty, to determine whether and how the Doppler shift contributes to localisation, which can then be incorporated into the beam model.

Unlike full-wave simulations, however, the beam model gives specific contributions to localisation (Chapter 6). This physical insight is crucial for interpretation of DBS data.

On a more applied level, the beam model's insights allow for better DBS diagnostics to be designed and built. For example, we have shown that mismatch attenuation is more severe at higher wavenumbers, such that one should check the mismatch attenuation at the highest wavenumber in the first instance.

The beam model would also yield valuable physical insight when applied to the cross-polarisation scattering diagnostic and the high-k scattering diagnostic. We envisage that the formalism of these two diagnostics would bear many similarities to that which was presented in this thesis. Much like with DBS, the beam models for these other diagnostics will need to be compared with experiments to ascertain their applicability.

Appendix A

Discontinuity of $\boldsymbol{\Psi}$ at the vacuum-plasma boundary

We are going to look at a special case of the vacuum-plasma boundary, where the density n_e is continuous, but its gradient ∇n_e is discontinuous. Hence, the ray part of beam tracing is well-behaved, but there will be a discontinuity in the beam part. We need to find the matching conditions at the boundary for $\boldsymbol{\Psi}$. This is a special case of what was presented in earlier work [49].

We take the density to be zero on the plasma-vacuum interface. We also assume a general 2D curvature of the interface surface, which is relevant to our concerns because density is specified on flux surfaces, curved in 2D.

We re-express the exponential piece in $\mathbf{E}_b$ at the vacuum-plasma boundary as

$$\begin{aligned} E_b \propto \exp\Big[& \mathrm{i}s^{vp} + \mathrm{i}K_R^{vp}\Delta R + \mathrm{i}K_Z^{vp}\Delta Z + \mathrm{i}K_\zeta^{vp}\Delta\zeta \\ & + \frac{\mathrm{i}}{2}\big(\Psi_{RR}\left(\Delta R\right)^2 + 2\Psi_{RZ}\Delta R\Delta Z + \Psi_{ZZ}\left(\Delta Z\right)^2 \\ & + \Psi_{\zeta\zeta}\left(\Delta\zeta\right)^2 + 2\Psi_{R\zeta}\Delta R\Delta\zeta + 2\Psi_{\zeta Z}\Delta\zeta\Delta Z\big)\Big], \end{aligned} \tag{A.1}$$

where the superscript ^{vp} indicates that the variables are continuous across the vacuum-plasma boundary. We need to impose continuity of $\mathbf{E}_b$ across this boundary. Since we are dealing with the special case where the density is zero at the boundary, there is no charge or current, so all components of $\mathbf{E}_b$ are continuous. To proceed, we have to figure out how to parameterise the vacuum-plasma boundary. Since the density is specified on a flux surface, the discontinuity in $\boldsymbol{\Psi}$ occurs on a flux surface, which we

take to also be the vacuum-plasma boundary. Two points on the same flux surface must have the same flux label. Hence, they are related by

$$\begin{aligned}\psi_p(R,Z) &= \psi_p(R+\Delta R, Z+\Delta Z)\\ &\simeq \psi_p(R,Z) + \frac{\partial\psi_p}{\partial R}\Delta R + \frac{\partial\psi_p}{\partial Z}\Delta Z\\ &+ \frac{1}{2}\left(\frac{\partial^2\psi_p}{\partial R^2}(\Delta R)^2 + 2\frac{\partial^2\psi_p}{\partial R\partial Z}\Delta R\Delta Z + \frac{\partial^2\psi_p}{\partial Z^2}(\Delta Z)^2\right),\end{aligned} \tag{A.2}$$

where we have expanded to second order. We write $\Delta R = \Delta R^{(0)} + \Delta R^{(1)} + \ldots$ and $\Delta Z = \Delta Z^{(0)} + \Delta Z^{(1)} + \ldots$. We parameterise poloidal displacement with ξ, such that

$$\begin{pmatrix} \Delta R^{(0)} \\ \Delta Z^{(0)} \end{pmatrix} = \begin{pmatrix} -\partial\psi_p/\partial Z \\ \partial\psi_p/\partial R \end{pmatrix}\xi. \tag{A.3}$$

This choice ensures that equation (A.2) is satisfied to first order. To second order, we find

$$\begin{aligned}&\frac{\partial\psi_p}{\partial R}\Delta R^{(1)} + \frac{\partial\psi_p}{\partial Z}\Delta Z^{(1)}\\ &+ \frac{1}{2}\left(\frac{\partial^2\psi_p}{\partial R^2}\left(\Delta R^{(0)}\right)^2 + 2\frac{\partial^2\psi_p}{\partial R\partial Z}\Delta R^{(0)}\Delta Z^{(0)} + \frac{\partial^2\psi_p}{\partial Z^2}\left(\Delta Z^{(0)}\right)^2\right) = 0.\end{aligned} \tag{A.4}$$

The next order corrections are thus

$$\begin{pmatrix} \Delta R^{(1)} \\ \Delta Z^{(1)} \end{pmatrix} = \begin{pmatrix} -\partial\psi_p/\partial Z \\ \partial\psi_p/\partial R \end{pmatrix}\xi^{(1)} + \eta\begin{pmatrix} \partial\psi_p/\partial R \\ \partial\psi_p/\partial Z \end{pmatrix}, \tag{A.5}$$

where η is given by

$$\begin{aligned}\eta = -\frac{1}{2}&\left[\frac{\partial^2\psi_p}{\partial R^2}\left(\frac{\partial\psi_p}{\partial Z}\right)^2 + 2\frac{\partial^2\psi_p}{\partial R\partial Z}\frac{\partial\psi_p}{\partial R}\frac{\partial\psi_p}{\partial Z} + \frac{\partial^2\psi_p}{\partial Z^2}\left(\frac{\partial\psi_p}{\partial R}\right)^2\right]\\ &\times\left[\left(\frac{\partial\psi_p}{\partial R}\right)^2 + \left(\frac{\partial\psi_p}{\partial Z}\right)^2\right]^{-1}\xi^2.\end{aligned} \tag{A.6}$$

We redefine ξ such that it incorporates the $\xi^{(1)}$ term, getting

$$\begin{pmatrix} \Delta R^{(1)} \\ \Delta Z^{(1)} \end{pmatrix} = \eta\begin{pmatrix} -\partial\psi_p/\partial R \\ \partial\psi_p/\partial Z \end{pmatrix}. \tag{A.7}$$

Imposing continuity across the plasma-vacuum boundary, we find the formula

$$\begin{aligned}&s^{vp} + K_R^{vp}\Delta R + K_Z^{vp}\Delta Z + K_\zeta^{vp}\Delta\zeta + \frac{1}{2}\left(\Psi_{RR}^v(\Delta R)^2 + \Psi_{ZZ}^v(\Delta Z)^2 + \Psi_{\zeta\zeta}^v(\Delta\zeta)^2\right)\\ &+ \Psi_{RZ}^v\Delta R\Delta Z + \Psi_{R\zeta}^v\Delta R\Delta\zeta + \Psi_{\zeta Z}^v\Delta\zeta\Delta Z\\ =&s^{vp} + K_R^{vp}\Delta R + K_Z^{vp}\Delta Z + K_\zeta^{vp}\Delta\zeta + \frac{1}{2}\left(\Psi_{RR}^p(\Delta R)^2 + \Psi_{ZZ}^p(\Delta Z)^2 + \Psi_{\zeta\zeta}^p(\Delta\zeta)^2\right)\\ &+ \Psi_{RZ}^p\Delta R\Delta Z + \Psi_{R\zeta}^p\Delta R\Delta\zeta + \Psi_{\zeta Z}^p\Delta\zeta\Delta Z.\end{aligned} \tag{A.8}$$

We now consider displacement in the toroidal direction only, $\xi = 0$,

$$K_\zeta^{vp} + \frac{1}{2}\Psi_{\zeta\zeta}^{v}\left(\Delta\zeta\right)^2 = K_\zeta^{vp} + \frac{1}{2}\Psi_{\zeta\zeta}^{p}\left(\Delta\zeta\right)^2, \tag{A.9}$$

hence

$$\Psi_{\zeta\zeta}^{v} = \Psi_{\zeta\zeta}^{p}. \tag{A.10}$$

It may seem surprising that the curvature of the flux surface in the toroidal direction does not seem to appear in this equation. However, this curvature is already accounted for in our definition of $\Psi_{\zeta\zeta}$ that gives rise to the $K_R R$ term in equation (2.126). Moving forward, we consider purely poloidal displacement, that is $\Delta\zeta = 0$,

$$\begin{aligned} &K_R^{vp}\Delta R + K_Z^{vp}\Delta Z + \frac{1}{2}\left(\Psi_{RR}^{v}\left(\Delta R\right)^2 + 2\Psi_{RZ}^{v}\Delta R\Delta Z + \Psi_{ZZ}^{v}\left(\Delta Z\right)^2\right) \\ &\quad = K_R^{vp}\Delta R + K_Z^{vp}\Delta Z + \frac{1}{2}\left(\Psi_{RR}^{p}\left(\Delta R\right)^2 + 2\Psi_{RZ}^{p}\Delta R\Delta Z + \Psi_{ZZ}^{p}\left(\Delta Z\right)^2\right). \end{aligned} \tag{A.11}$$

Hence, to leading order, we use equations (A.3) and (A.7) to get

$$\begin{aligned} &\Psi_{RR}^{v}\left(\frac{\partial\psi_p}{\partial Z}\right)^2 - 2\Psi_{RZ}^{v}\frac{\partial\psi_p}{\partial R}\frac{\partial\psi_p}{\partial Z} + \Psi_{ZZ}^{v}\left(\frac{\partial\psi_p}{\partial R}\right)^2 \\ &\quad = \Psi_{RR}^{p}\left(\frac{\partial\psi_p}{\partial Z}\right)^2 - 2\Psi_{RZ}^{p}\frac{\partial\psi_p}{\partial R}\frac{\partial\psi_p}{\partial Z} + \Psi_{ZZ}^{p}\left(\frac{\partial\psi_p}{\partial R}\right)^2. \end{aligned} \tag{A.12}$$

Note that $\Delta R^{(2)}$ and $\Delta Z^{(2)}$ do not contribute because of the continuity of $\mathbf{K}$ across the boundary [49]. Finally, we consider a displacement that is simultaneously in the toroidal and poloidal directions. Following similar steps as earlier, and using the results we already have, we find that

$$\Psi_{R\zeta}^{v}\Delta R\Delta\zeta + \Psi_{\zeta Z}^{v}\Delta\zeta\Delta Z = \Psi_{R\zeta}^{p}\Delta R\Delta\zeta + \Psi_{\zeta Z}^{p}\Delta\zeta\Delta Z. \tag{A.13}$$

Hence,

$$-\Psi_{R\zeta}^{v}\frac{\partial\psi_p}{\partial Z} + \Psi_{\zeta Z}^{v}\frac{\partial\psi_p}{\partial R} = -\Psi_{R\zeta}^{p}\frac{\partial\psi_p}{\partial Z} + \Psi_{\zeta Z}^{p}\frac{\partial\psi_p}{\partial R}. \tag{A.14}$$

Equations (A.10), (A.12), and (A.14) give us 3 conditions for the transition, but we have 6 variables we want to find (either $\boldsymbol{\Psi}^p$ or $\boldsymbol{\Psi}^v$). The other 3 conditions can be found from equation (2.57), giving us

$$\boldsymbol{\Psi}^p \cdot \nabla_K H + \nabla H = 0. \tag{A.15}$$

We solve these six linear equations numerically in Scotty.

If the equilibrium density were also discontinuous, then we would have to solve three more equations. Two are linear equations, which state that the components of $\mathbf{K}$ parallel to the flux surface have to be continuous. The third component of the wavevector can be determined from the dispersion relation, $H = 0$, which is nonlinear. A discontinuous $\mathbf{K}$ also means that the six equations for $\boldsymbol{\Psi}$ are changed slightly, because $\mathbf{K}^c \neq \hat{\mathbf{K}}^p$. This is not currently implemented in Scotty.

Appendix B

Complex Gaussian integration

B.1 1D complex Gaussian integration

Unsurprisingly, working with a Gaussian beam means that we have to solve a large number of Gaussian integrals. Since $\boldsymbol{\Psi}_w$ is complex, we are looking to solve Gaussian integrals of the form

$$\int_{-\infty}^{\infty} \exp(-ax^2)\ \mathrm{d}x, \tag{B.1}$$

where x is real and a is a complex constant with a positive real part. Note that the notation in this part of the appendix is separate from the rest of the paper. In order to evaluate this integral, we consider the contour integration in Figure (B.1). We define $\alpha = \arg\left(\sqrt{a^*}\right)$, with $-\pi/4 < \alpha \leq \pi/4$. Since there are no poles within the contour of integration, we have

$$\int_{\gamma_{OA}} \exp(-az^2)\ \mathrm{d}z + \int_{\gamma_{AB}} \exp(-az^2)\ \mathrm{d}z + \int_{\gamma_{BO}} \exp(-az^2)\ \mathrm{d}z = 0. \tag{B.2}$$

We evaluate each of the three integrals in turn. Since γ_{OA} lies entirely on the real axis, we have

$$\int_{\gamma_{OA}} \exp(-az^2)\ \mathrm{d}z = \int_0^R \exp(-ax^2)\ \mathrm{d}x, \tag{B.3}$$

which is what we are trying to find. To evaluate the integral over γ_{BO}, we use the substitution

$$z = \frac{\sqrt{a^*}}{|a|}u, \tag{B.4}$$

Hence, we have

$$\int_{\gamma_{BO}} \exp(-az^2)\ \mathrm{d}z = -\frac{\sqrt{a^*}}{|a|}\int_0^{R\sqrt{|a|}} \exp(-u^2)\ \mathrm{d}u. \tag{B.5}$$

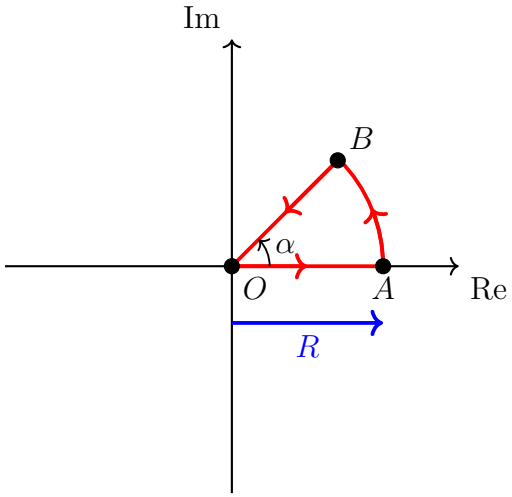

Figure B.1: The contour for evaluating complex Gaussian integrals, of the form $\int_{-\infty}^{\infty} \exp(-ax^2)\ \mathrm{d}x$, in the complex plane. Note the direction of R, which is away from the origin. Here x is real, a is a complex constant with a positive real part, and $\alpha = \arg\left(\sqrt{a^*}\right)$, with $-\pi/4 < \alpha \leq \pi/4$.

The final integral over γ_{AB} can be calculated using $z = R\exp(\mathrm{i}\phi)$

$$\int_{\gamma_{AB}} \exp(-az^2)\ \mathrm{d}z = \int_0^{\alpha} \exp\left[-aR^2\exp(2\mathrm{i}\phi)\right] \mathrm{i}R\exp(\mathrm{i}\phi)\ \mathrm{d}\phi. \tag{B.6}$$

We use the triangle inequality to show that

$$\left|\int_{\gamma_{AB}} \phi\exp\left[-az^2\right]\ \mathrm{d}z\right| \leq \int_0^{\alpha} R\exp\left[-|a|R^2\cos\left(2\phi - 2\alpha\right)\right]\ \mathrm{d}\phi. \tag{B.7}$$

As $R \to \infty$, we find that $\int_0^{\alpha} R\exp\left[-|a|R^2\cos\left(2\phi - 2\alpha\right)\right]\ \mathrm{d}z \to 0$ as long as $\cos(2\phi - 2\alpha) > 0$. Since $-\pi/4 < \alpha \leq \pi/4$ and $0 \leq \phi \leq |\alpha|$, this holds. Thus, when numerically solving equations in this paper, it is important to make sure that the solver is indeed using the correct phase for $\sqrt{a^*}$. We can choose the appropriate root at the last step. In the limit $R \to \infty$, we get

$$\int_0^{\infty} \exp(-ax^2)\ \mathrm{d}x = \frac{\sqrt{a^*}}{|a|}\int_0^{\infty} \exp(-u^2)\ \mathrm{d}u. \tag{B.8}$$

Hence, we have

$$\int_{-\infty}^{\infty} \exp(-ax^2)\ \mathrm{d}x = \frac{\sqrt{\pi a^*}}{|a|} = \sqrt{\frac{\pi}{a}}. \tag{B.9}$$

We need to choose the root that satisfies

$$\mathrm{Re}\left[\sqrt{\frac{\pi}{a}}\right] > 0. \tag{B.10}$$

B.2 2D complex Gaussian integration

We now seek to solve integrals of the form

$$\int_{-\infty}^{\infty}\int_{-\infty}^{\infty} \exp(-\mathbf{r}\cdot\boldsymbol{C}\cdot\mathbf{r})\ \mathrm{d}x\ \mathrm{d}y, \tag{B.11}$$

where $\boldsymbol{C}$ is a symmetric complex matrix

$$\boldsymbol{C} = C_{xx}\hat{\mathbf{x}}\hat{\mathbf{x}} + C_{xy}\left(\hat{\mathbf{x}}\hat{\mathbf{y}} + \hat{\mathbf{y}}\hat{\mathbf{x}}\right) + C_{yy}\hat{\mathbf{y}}\hat{\mathbf{y}}, \tag{B.12}$$

and $\mathbf{r}$ is a real vector

$$\mathbf{r} = r_x\hat{\mathbf{x}} + r_y\hat{\mathbf{y}}. \tag{B.13}$$

Hence, we have

$$\begin{aligned}&\int_{-\infty}^{\infty}\int_{-\infty}^{\infty} \exp(-\mathbf{r}\cdot\boldsymbol{C}\cdot\mathbf{r})\ \mathrm{d}x\ \mathrm{d}y \\ &= \int_{-\infty}^{\infty}\int_{-\infty}^{\infty} \exp\left(-C_{xx}r_x^2 - 2C_{xy}r_xr_y - C_{yy}r_y^2\right)\ \mathrm{d}x\ \mathrm{d}y.\end{aligned} \tag{B.14}$$

For $\exp(-\mathbf{r}\cdot\boldsymbol{C}\cdot\mathbf{r})$ to be integrable, the matrix $\mathrm{Re}(\boldsymbol{C})$ must be positive definite, and hence $\det\left[\mathrm{Re}(C)\right] > 0$ and $\mathrm{Re}(C_{xx}) > 0$.

To calculate the integral, we complete the square for r_x,

$$-C_{xx}r_x^2 - 2C_{xy}r_xr_y - C_{yy}r_y^2 = -C_{xx}\left(r_x + \frac{C_{xy}r_y}{C_{xx}}\right)^2 + \frac{C_{xy}^2r_y^2}{C_{xx}} - C_{yy}r_y^2, \tag{B.15}$$

and evaluate the Gaussian integral in r_x, getting

$$\begin{aligned}&\int_{-\infty}^{\infty}\int_{-\infty}^{\infty} \exp\left(-C_{xx}r_x^2 - 2C_{xy}r_xr_y - C_{yy}r_y^2\right)\ \mathrm{d}x\ \mathrm{d}y \\ &\qquad = \sqrt{\frac{\pi}{C_{xx}}}\int_{-\infty}^{\infty} \exp\left(\frac{C_{xy}^2r_y^2}{C_{xx}} - C_{yy}r_y^2,\right)\ \mathrm{d}x\ \mathrm{d}y,\end{aligned} \tag{B.16}$$

where we choose the root as argued in equation (B.10), which is

$$\mathrm{Re}\left[\sqrt{\frac{\pi}{C_{xx}}}\right] > 0. \tag{B.17}$$

Moving forward, we note that

$$\frac{C_{xy}^2r_y^2}{C_{xx}} - C_{yy}r_y^2 = -\frac{\det(\boldsymbol{C})}{C_{xx}}r_y^2, \tag{B.18}$$

and evaluate the second Gaussian integral, getting

$$\sqrt{\frac{\pi}{C_{xx}}}\int_{-\infty}^{\infty}\exp\left(\frac{C_{xy}^2 r_y^2}{C_{xx}} - C_{yy}r_y^2,\right)\,\mathrm{d}x\,\mathrm{d}y$$
$$= \sqrt{\frac{\pi}{C_{xx}}}\sqrt{\frac{\pi C_{xx}}{\det(\boldsymbol{C})}}, \tag{B.19}$$

where we choose the root such that $\mathrm{Re}[\sqrt{\pi C_{xx}/\det(\boldsymbol{C})}] > 0$. To simplify this expression, we write

$$\sqrt{\det(\boldsymbol{C})} = \sqrt{C_{xx}}\sqrt{\frac{\det(\boldsymbol{C})}{C_{xx}}}, \tag{B.20}$$

where we must be careful to make sure that each square root is chosen such that its real part is positive, which in turn determines the phase of $\det(\boldsymbol{C})$. We now have

$$\int_{-\infty}^{\infty}\int_{-\infty}^{\infty}\exp(-\mathbf{r}\cdot\boldsymbol{C}\cdot\mathbf{r})\,\mathrm{d}x\,\mathrm{d}y, = \pi\left[\det(\boldsymbol{C})\right]^{-\frac{1}{2}}, \tag{B.21}$$

if we choose the phases as prescribed, which we do for this paper.

Appendix C

Derivation of u_1 and u_2

We seek to find two coordinates whose gradients are perpendicular to $\hat{\mathbf{b}}$ as well as to each other. Unfortunately, due to magnetic shear, it is in general not possible to find a such a set of coordinates throughout the whole volume of a plasma, but it is possible to do it along a line. Hence, we first seek to find u_1 and u_2 such that ∇u_1 and ∇u_2 are perpendicular to $\hat{\mathbf{b}}$ and to each other along $\mathbf{w} = 0$, that is, along the central ray. We then find the higher order corrections to u_1 and u_2 at finite $\mathbf{w}$ by imposing that ∇u_1 and ∇u_2 be perpendicular to $\hat{\mathbf{b}}$ everywhere.

We know that u_i must satisfy

$$\hat{\mathbf{b}}(\mathbf{q}(\tau) + \mathbf{w}) \cdot \nabla u_i \simeq \left[\hat{\mathbf{b}}(\mathbf{q}(\tau)) + \mathbf{w} \cdot \nabla \hat{\mathbf{b}}(\mathbf{q}(\tau))\right] \cdot \nabla u_i = 0. \tag{C.1}$$

Using the chain rule, we get

$$\underbrace{\left(\hat{\mathbf{b}} + \mathbf{w} \cdot \nabla \hat{\mathbf{b}}\right) \cdot \nabla \tau \frac{\partial u_i}{\partial \tau}}_{\sim \frac{1}{L} u_i} + \underbrace{\left(\hat{\mathbf{b}} + \mathbf{w} \cdot \nabla \hat{\mathbf{b}}\right) \cdot \nabla w_x \frac{\partial u_i}{\partial w_x}}_{\sim \frac{1}{W} u_i} + \underbrace{\left(\hat{\mathbf{b}} + \mathbf{w} \cdot \nabla \hat{\mathbf{b}}\right) \cdot \nabla w_y \frac{\partial u_i}{\partial w_y}}_{\sim \frac{1}{W} \frac{W}{L} \sim \frac{1}{L} u_i} = 0. \tag{C.2}$$

The size of the term proportional to $\partial u_i / \partial w_y$ is determined by the fact that ∇w_y points mostly along $\hat{\mathbf{y}}$ in Figure 4.1, and this direction is perpendicular to $\hat{\mathbf{b}}$. Using reciprocal vectors, we follow the same procedure used to derive equation (2.22) and get

$$\nabla w_x = \hat{\mathbf{x}} + \frac{w_y \hat{\mathbf{g}}}{g(1 - \boldsymbol{\kappa} \cdot \mathbf{w})} \left(\frac{\mathrm{d}\hat{\mathbf{x}}}{\mathrm{d}\tau} \cdot \hat{\mathbf{y}}\right), \tag{C.3}$$

and

$$\nabla w_y = \hat{\mathbf{y}} - \frac{w_x \hat{\mathbf{g}}}{g(1 - \boldsymbol{\kappa} \cdot \mathbf{w})} \left(\frac{\mathrm{d}\hat{\mathbf{x}}}{\mathrm{d}\tau} \cdot \hat{\mathbf{y}}\right). \tag{C.4}$$

Having obtained these results, we then expand u_i in W/L to obtain

$$u_i = u_i^{(0)} + u_i^{(1)} + u_i^{(2)} + \ldots, \tag{C.5}$$

where $u_i^{(n)} \sim (W/L)^n \; u_i^{(0)}$. Since the term with $\partial u_i/\partial w_x$ is much larger than the other two terms, $\partial u_i^{(0)}/\partial w_x = 0$. Hence, $u_i^{(0)} = u_i^{(0)}(\tau, w_y)$. Since we want $\nabla u_1(\mathbf{w} = 0) = \hat{\mathbf{u}}_1$ and $\nabla u_2(\mathbf{w} = 0) = \hat{\mathbf{u}}_2$, where these directions are shown in Figure 4.1, we choose

$$u_1^{(0)} = u_1^{(0)}(\tau) = \int_0^\tau g(\tau') \cos\theta(\tau') \mathrm{d}\tau, \tag{C.6}$$

and

$$u_2^{(0)} = u_2^{(0)}(w_y) = w_y. \tag{C.7}$$

This turns out to be convenient because one direction is only a function of τ, while the other is only a function of w_y.

We now find the higher order corrections. The first order (W/L) equation for u_1 is

$$-\sin\theta\cos\theta - \frac{\partial u_1^{(1)}}{\partial w_x}\cos\theta = 0, \tag{C.8}$$

which gives us

$$u_1^{(1)} = -w_x \sin\theta. \tag{C.9}$$

The first order (W/L) equation for u_2 is

$$-\frac{\partial u_2^{(1)}}{\partial w_x}\cos\theta + \left(w_x \frac{\sin\theta}{g}\frac{\mathrm{d}\hat{\mathbf{x}}}{\mathrm{d}\tau}\cdot\hat{\mathbf{y}} + \mathbf{w}\cdot\nabla\hat{\mathbf{b}}\cdot\hat{\mathbf{y}} \right)\frac{\partial u_2^{(0)}}{\partial w_y} = 0, \tag{C.10}$$

which gives us

$$u_2^{(1)} = \frac{w_x^2}{2\cos\theta}\left(\frac{\sin\theta}{g}\frac{\mathrm{d}\hat{\mathbf{x}}}{\mathrm{d}\tau}\cdot\hat{\mathbf{y}} + \hat{\mathbf{x}}\cdot\nabla\hat{\mathbf{b}}\cdot\hat{\mathbf{y}} \right) + \frac{w_x w_y}{\cos\theta}\hat{\mathbf{y}}\cdot\nabla\hat{\mathbf{b}}\cdot\hat{\mathbf{y}}. \tag{C.11}$$

Here we have used equations (2.22), (C.3), and (C.4). Since $k_{\perp,1}u_1^{(1)} \sim W/\lambda \gg 1$, we need to find the next order correction $u_1^{(2)}$, whereas $k_{\perp,2}u_2^{(1)} \sim (1/\lambda)(W^2/L) \sim 1$ indicates that expanding u_2 to this order is already sufficient. To get the second order contribution $u_1^{(2)}$, we use

$$\begin{aligned} &-\frac{\sin\theta}{g}\frac{\partial u_1^{(1)}}{\partial\tau} + \left(-\frac{\sin\theta}{g}\boldsymbol{\kappa}\cdot\mathbf{w} + \frac{\mathbf{w}\cdot\nabla\hat{\mathbf{b}}\cdot\hat{\mathbf{g}}}{g} \right)\frac{\partial u_1^{(0)}}{\partial\tau} \\ &\quad -\cos\theta\frac{\partial u_1^{(2)}}{\partial w_x} + \left(-\frac{\sin\theta}{g}\frac{\mathrm{d}\hat{\mathbf{x}}}{\mathrm{d}\tau}\cdot\hat{\mathbf{y}}w_y + \mathbf{w}\cdot\nabla\hat{\mathbf{b}}\cdot\hat{\mathbf{x}} \right)\frac{\partial u_1^{(1)}}{\partial w_x} = 0, \end{aligned} \tag{C.12}$$

and find that

$$u_1^{(2)} = \frac{w_x^2}{2}\left(\frac{\sin\theta}{g}\frac{\mathrm{d}\theta}{\mathrm{d}\tau} - \boldsymbol{\kappa}\cdot\hat{\mathbf{x}}\sin\theta + \hat{\mathbf{x}}\cdot\nabla\hat{\mathbf{b}}\cdot\hat{\mathbf{g}} - \hat{\mathbf{x}}\cdot\nabla\hat{\mathbf{b}}\cdot\hat{\mathbf{x}}\tan\theta\right)$$
$$+ w_x w_y\left(-\boldsymbol{\kappa}\cdot\hat{\mathbf{y}}\sin\theta + \hat{\mathbf{y}}\cdot\nabla\hat{\mathbf{b}}\cdot\hat{\mathbf{g}} + \frac{\sin\theta\tan\theta}{g}\frac{\mathrm{d}\hat{\mathbf{x}}}{\mathrm{d}\tau}\cdot\hat{\mathbf{y}} - \hat{\mathbf{y}}\cdot\nabla\hat{\mathbf{b}}\cdot\hat{\mathbf{x}}\tan\theta\right). \quad \text{(C.13)}$$

Appendix D

Relationship between θ and θ_m

To shed light on how θ and θ_m relate to each other (when they are small), we seek to make explicit the piece

$$\frac{\partial H}{\partial(\mathbf{K}\cdot\hat{\mathbf{b}})^2}\left(\frac{\partial H}{\partial K^2}\right)^{-1}, \tag{D.1}$$

in equation (4.39). This algebra-heavy process is detailed in Sectopm D.1, while the results and their significance are discussed in Section D.2.

D.1 Derivation of θ/θ_m

The derivation is somewhat onerous because we cannot neglect θ_m from the onset; we need to keep $K_\parallel$ for part of the derivation to be able to calculate $\partial H/\partial K_\parallel^2$. Fortunately, since we are finding the ratio of two derivatives of H, we are free to choose a $\bar{H}$ that satisfies equation (2.156) because

$$\frac{\partial H}{\partial K_\parallel^2}\left(\frac{\partial H}{\partial K^2}\right)^{-1} = \frac{\partial \bar{H}}{\partial K_\parallel^2}\left(\frac{\partial \bar{H}}{\partial K^2}\right)^{-1}. \tag{D.2}$$

For this calculation, we choose a convenient $\bar{H}$ to minimise the unpleasantness of the resulting algebra: $\bar{H} = \det(\boldsymbol{D})$,

$$\begin{aligned}\det(\boldsymbol{D}) = &\left(\epsilon_{11} - N_\parallel^2\right)\left(\epsilon_{11} - N^2\right)\left(\epsilon_{bb} - N^2 + N_\parallel^2\right)\\ &- N_\parallel^2\left(N^2 - N_\parallel^2\right)\left(\epsilon_{11} - N^2\right) - \epsilon_{12}^2\left(\epsilon_{bb} - N^2 + N_\parallel^2\right).\end{aligned} \tag{D.3}$$

Here we have used equation (2.141), as well as the notation $N = Kc/\Omega$ and $N_\parallel = K_\parallel c/\Omega$. The derivatives that we need can then be calculated for $N_\parallel^2 = N^2\theta_m^2 \ll N^2$.

We find

$$\frac{\partial \det(\boldsymbol{D})}{\partial K^2} = \frac{c^2}{\Omega^2}\left[\epsilon_{11}\left(N^2-\epsilon_{bb}\right)+\epsilon_{11}\left(N^2-\epsilon_{11}\right)+\epsilon_{12}^2\right], \tag{D.4}$$

and

$$\frac{\partial \det(\boldsymbol{D})}{\partial K_\parallel^2} = \frac{c^2}{\Omega^2}\Big[\epsilon_{11}\left(\epsilon_{11}-N^2\right)-\left(\epsilon_{11}-N^2\right)\left(\epsilon_{bb}-N^2\right) - N^2\left(\epsilon_{11}-N^2\right)-\epsilon_{12}^2\Big], \tag{D.5}$$

Now that we have evaluated the derivatives of $\bar{H}$, we find the piece that we care about

$$\frac{\partial H}{\partial K_\parallel^2}\left(\frac{\partial H}{\partial K^2}\right)^{-1} = \frac{\epsilon_{11}^2-\epsilon_{12}^2-\epsilon_{11}\epsilon_{bb}+N^2\left(\epsilon_{bb}-\epsilon_{11}\right)}{-\epsilon_{11}^2+\epsilon_{12}^2-\epsilon_{11}\epsilon_{bb}+2N^2\epsilon_{11}}. \tag{D.6}$$

For the O mode, $N^2=\epsilon_{bb}$, we have

$$\begin{aligned}\frac{\partial H}{\partial K_\parallel^2}\left(\frac{\partial H}{\partial K^2}\right)^{-1} &= -\frac{\left(\epsilon_{11}-\epsilon_{bb}\right)^2-\epsilon_{12}^2}{\epsilon_{11}\left(\epsilon_{11}-\epsilon_{bb}\right)-\epsilon_{12}^2}\\ &= -\frac{\Omega_{pe}^2}{\Omega^2}.\end{aligned} \tag{D.7}$$

Similarly, for the X mode, $\epsilon_{11}(\epsilon_{11}-N^2)=\epsilon_{12}^2$, we have

$$\frac{\partial H}{\partial K_\parallel^2}\left(\frac{\partial H}{\partial K^2}\right)^{-1} = -\frac{\epsilon_{12}^2\epsilon_{bb}}{\epsilon_{11}\left[\epsilon_{11}\left(\epsilon_{11}-\epsilon_{bb}\right)-\epsilon_{12}^2\right]} \tag{D.8}$$

$$= \frac{\Omega_{pe}^2\left(\Omega^2-\Omega_{pe}^2\right)}{\Omega^2\left(\Omega^2-\Omega_{ce}^2-\Omega_{pe}^2\right)}. \tag{D.9}$$

D.2 Properties of θ/θ_m

Now that we have the ratio between θ_m and θ, we discuss what it means for the O and X modes. We have

$$\frac{\theta}{\theta_m} = -1+\frac{\Omega_{pe}^2}{\Omega^2}, \tag{D.10}$$

for the O-mode and

$$\frac{\theta}{\theta_m} = -1-\frac{\Omega_{pe}^2\left(\Omega^2-\Omega_{pe}^2\right)}{\Omega^2\left(\Omega^2-\Omega_{ce}^2-\Omega_{pe}^2\right)}, \tag{D.11}$$

for the X-mode, Figure D.1. For the O-mode, since we launch a beam into the plasma from vacuum, $\Omega > \Omega_{pe}$ always, thus $\theta/\theta_m \leq 0$ and $|\theta/\theta_m| \leq 1$. However, for the X-mode, the cut-off frequency is $\Omega_R = (\Omega_{ce}^2/4+\Omega_{pe}^2)^{1/2}+\Omega_{ce}/2$, which is above the

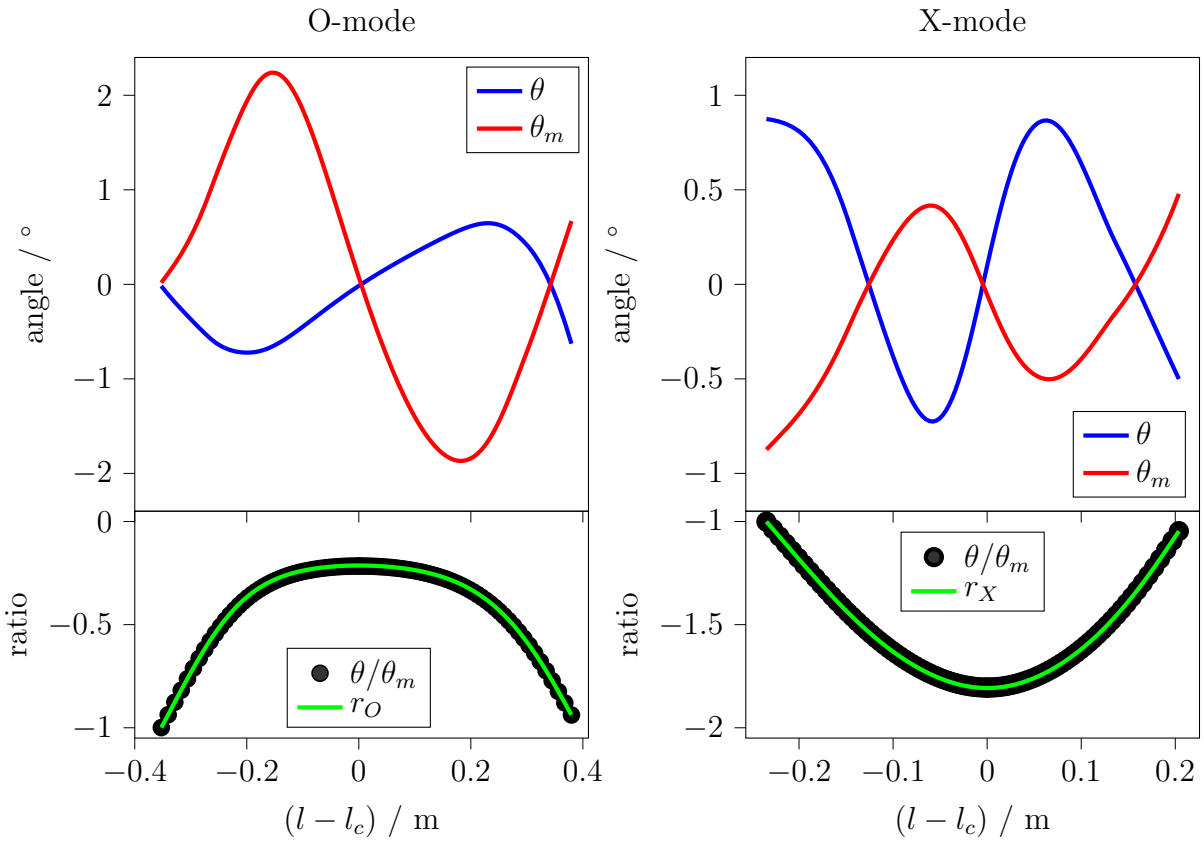

Figure D.1: The variation of θ and θ_m along the ray (top), and how they relate to each other (bottom). Here $l - l_c$ is the distance along the ray from the cut-off. The standard MAST test case for our paper was used for the O-mode. For the X-mode, the toroidal launch angle was changed to $-7°$ such that $\theta_m = 0$ at the cut-off.

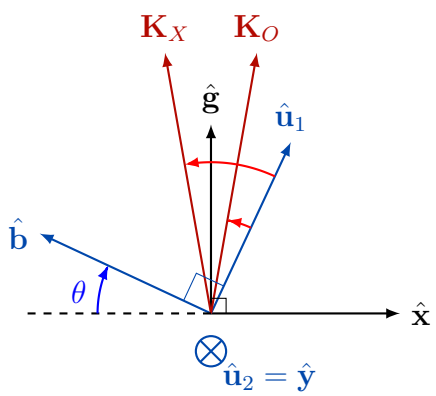

(a) K_X and K_O when $\theta < 0$.

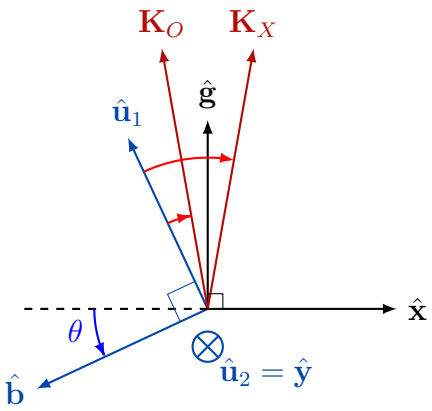

(b) K_X and K_O when $\theta > 0$.

Figure D.2: The wavevectors of the X-mode and O-mode are denoted by K_X and K_O respectively. This notation is only used in this section. We have shown that for the X-mode, $|\theta| > |\theta_m|$, and the O-mode, $|\theta| < |\theta_m|$. The unlabelled bright red arrows show θ_m. Note that θ and θ_m always have different signs, for reasons explained in this section. The angles used in this figure were chosen for illustration purposes: the real values of θ and θ_m for which our expansion is valid are too small for legible schematics.

upper hybrid frequency $\Omega_{UH}^2 = \Omega_{ce}^2 + \Omega_{pe}^2$. Consequently, we still have $\theta/\theta_m \leq 0$, but now $|\theta/\theta_m| > 1$.

Since θ/θ_m is always negative, θ and θ_m have different signs no matter the mode. For the O-mode, the magnitude of this ratio is always less than one, so $|\theta| < |\theta_m|$, and for the X-mode, the magnitude of the same ratio is always more than one, so $|\theta| > |\theta_m|$. This is illustrated in Figure D.2 for both positive and negative θ.

Appendix E

Beam parameters

We present the methods and data used to determine the MAST DBS initial conditions required by our beam-tracing code, Scotty. At the point of writing, the MAST DBS had long since lost its original configuration. Hence, a straightforward measurement of beam properties is not possible. As such, we have seek to figure out what the launch beam widths and curvatures are, given what we know of the horn-lens system.

For both bands, aspherical hyperbolic-planar lenses were used. As the name implies, one side of the lens is planar, and the other is hyperbolic. The lenses were designed such that rays originating from the focal point would leave the lens parallel to the optic axis (Figure E.1). For the purposes of this thesis, we have approximated these lenses to be thin spherical lenses with the corresponding focal lengths: 27cm for the Q band lens and 12.5cm for the V band lens.

The Q-band antenna was a standard smooth brass conical horn (Figure E.2). We take the beam width at the curvature to be 0.76 of the aperture radius and the associated radius of curvature to be the slant length of the horn (aperture radius divided by the sine of the horn-opening half-angle) [66].

The V-band antenna was a custom-made narrow-beam corrugated scalar horn, model: Quinstar QSH-V2500. Its frequency band followed the WR-15 standard (50–75GHz), the far-field beam divergence full-angle was 25° in the mid-band (62.5GHz), and it was fed with a circular waveguide with a diameter of 0.165 inches. Quinstar's catalogue claims that the emission pattern is highly symmetric, and thus the far-field beam properties do not depend on the plane of measurement. Further details regarding the horn are not available; Quinstar's manual is sparse because the exact properties are

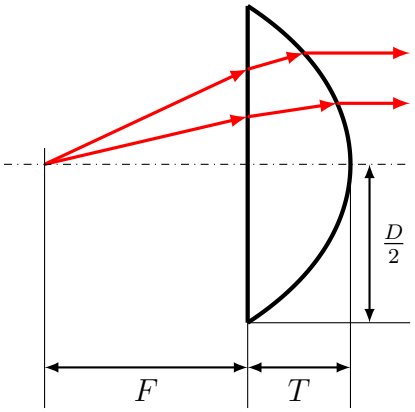

Figure E.1: Both lenses are made of high-density polyethylene which has a refractive index of $N = 1.53$. The Q band lens has focal length $F = 27$cm and diameter $D = 20$cm, while the V band lens $F = 12.5$cm and diameter $D = 19.5$cm. The flat side of the Q band lens was 27cm away from the aperture of the corresponding horn, while this distance was 13.9cm for the V band horn.

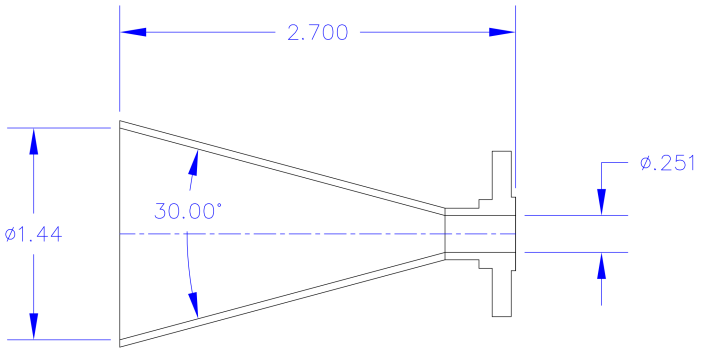

Figure E.2: Lengths given in inches. Schematic provided by UCLA collaborators.

customised for every order, and what we know of the specifics of the UCLA purchase have been gleaned from a handful of old emails. Based on the model number, this horn is an aperture-limited horn, so we take the beam waist to be at the horn's aperture. The width of the waist is then calculated from the far-field beam width.

References

[1] Jason Parisi and Justin Ball. *The future of fusion energy*. World Scientific, 2019.

[2] X Garbet, P Mantica, C Angioni, E Asp, Y Baranov, C Bourdelle, R Budny, F Crisanti, G Cordey, L Garzotti, et al. Physics of transport in tokamaks. *Plasma Physics and Controlled Fusion*, 46(12B):B557, 2004.

[3] M. Hirsch, E. Holzhauer, J. Baldzuhn, B. Kurzan, and B. Scott. Doppler reflectometry for the investigation of propagating density perturbations. *Plasma Physics and Controlled Fusion*, 43(12):1641–1660, 2001. ISSN 07413335. doi: 10.1088/0741-3335/43/12/302.

[4] J C Hillesheim, W A Peebles, T L Rhodes, L Schmitz, T A Carter, P A Gourdain, and G Wang. A multichannel, frequency-modulated, tunable Doppler backscattering and reflectometry system. *Review of Scientific Instruments*, 80(8), 2009. ISSN 00346748. doi: 10.1063/1.3205449.

[5] J C Hillesheim, F I Parra, M Barnes, N A Crocker, H Meyer, W A Peebles, R Scannell, and A Thornton. Dependence of intrinsic rotation reversals on collisionality in MAST. *Nuclear Fusion*, 55(3):032003, 2015. ISSN 0029-5515. doi: 10.1088/0029-5515/55/3/032003.

[6] G D Conway, B Scott, J Schirmer, M Reich, A Kendl, and the Asdex Upgrade Team. Direct measurement of zonal flows and geodesic acoustic mode oscillations in ASDEX Upgrade using Doppler reflectometry. *Plasma Physics and Controlled Fusion*, 47(8):1165–1185, 2005. ISSN 0741-3335. doi: 10.1088/0741-3335/47/8/003.

[7] Garrard D Conway, Emanuele Poli, Tim Happel, et al. Interaction of mean and oscillating plasma flows across confinement mode transitions. *Plasma and Fusion Research*, 5:S2005–S2005, 2010.

[8] L Schmitz. The role of turbulence–flow interactions in l-to h-mode transition dynamics: recent progress. *Nuclear Fusion*, 57(2):025003, 2017.

[9] G R Tynan, A Fujisawa, and G McKee. A review of experimental drift turbulence studies. *Plasma Physics and Controlled Fusion*, 51(11):113001, 2009.

[10] P Hennequin, C Honoré, A Truc, A Quéméneur, N Lemoine, J-M Chareau, and R Sabot. Doppler backscattering system for measuring fluctuations and their perpendicular velocity on tore supra. *Review of Scientific Instruments*, 75(10): 3881–3883, 2004.

[11] T Happel, T Estrada, E Blanco, V Tribaldos, A Cappa, and A Bustos. Doppler reflectometer system in the stellarator tj-ii. *Review of Scientific Instruments*, 80 (7):073502, 2009.

[12] Chu Zhou, A D Liu, X H Zhang, J Q Hu, M Y Wang, H Li, T Lan, J L Xie, X Sun, W X Ding, et al. Microwave doppler reflectometer system in the experimental advanced superconducting tokamak. *Review of Scientific Instruments*, 84(10): 103511, 2013.

[13] T Happel, T Görler, P Hennequin, C Lechte, M Bernert, G D Conway, S J Freethy, C Honoré, JR Pinzón, U Stroth, et al. Comparison of detailed experimental wavenumber spectra with gyrokinetic simulation aided by two-dimensional full-wave simulations. *Plasma Physics and Controlled Fusion*, 59(5):054009, 2017.

[14] Zhongbing Shi, Wulu Zhong, Min Jiang, Zengchen Yang, Boyu Zhang, Peiwan Shi, Wei Chen, Jie Wen, Chengyuan Chen, Bingzhong Fu, et al. A novel multi-channel quadrature doppler backward scattering reflectometer on the hl-2a tokamak. *Review of Scientific Instruments*, 87(11):113501, 2016.

[15] T L Rhodes, K Barada, W A Peebles, and N A Crocker. Simultaneous measurement of magnetic and density fluctuations via cross-polarization scattering and doppler backscattering on the diii-d tokamak. *Review of Scientific Instruments*, 87(11):11E726, 2016.

[16] JQ Hu, C Zhou, AD Liu, MY Wang, EJ Doyle, WA Peebles, G Wang, XH Zhang, J Zhang, X Feng, et al. An eight-channel doppler backscattering system in the experimental advanced superconducting tokamak. *Review of Scientific Instruments*, 88(7):073504, 2017.

[17] T Tokuzawa, H Tsuchiya, T Tsujimura, M Emoto, H Nakanishi, S Inagaki, K Ida, H Yamada, A Ejiri, K Y Watanabe, et al. Microwave frequency comb doppler reflectometer applying fast digital data acquisition system in lhd. *Review of Scientific Instruments*, 89(10):10H118, 2018.

[18] P Molina Cabrera, S Coda, L Porte, A Smolders, and TCV Team. V-band nanosecond-scale pulse reflectometer diagnostic in the tcv tokamak. *Review of Scientific Instruments*, 90(12):123501, 2019.

[19] J Wen, ZB Shi, W L Zhong, Z C Yang, Z J Yang, B Wang, B Jiang, PW Shi, J C Hillesheim, S Freethy, P Shi, A S Liang, R H Tong, K R Fang, W C Deng, Y Liu, X T Ding, and M Xu. A remote controlled and polarization angle tunable doppler backward scattering reflectometer. *Review of Scientific Instruments*, ?(?):?, 2021 (in press).

[20] D Carralero, T Happel, T Estrada, T Tokuzawa, J Martínez, E de la Luna, A Cappa, and J García. A feasibility study for a doppler reflectometer system in the jt-60sa tokamak. *Fusion Engineering and Design*, 173:112803, 2021.

[21] Francesco A Volpe. Prospects for a dominantly microwave-diagnosed magnetically confined fusion reactor. *Journal of Instrumentation*, 12(01):C01094, 2017.

[22] Alan E Costley. Towards diagnostics for a fusion reactor. *IEEE Transactions on Plasma Science*, 38(10):2934–2943, 2010.

[23] A D Piliya and A Yu Popov. On application of the reciprocity theorem to calculation of a microwave radiation signal in inhomogeneous hot magnetized plasmas. *Plasma Physics and Controlled Fusion*, 44(5):467, 2002.

[24] E Z Gusakov and A V Surkov. Spatial and wavenumber resolution of doppler reflectometry. *Plasma Physics and Controlled Fusion*, 46(7):1143, 2004.

[25] V V Bulanin and M V Yafanov. Spatial and spectral resolution of the plasma doppler reflectometry. *Plasma Physics Reports*, 32(1):47–55, 2006.

[26] E Z Gusakov and N V Kosolapova. Fluctuation reflectometry theory and the possibility of turbulence wave number spectrum reconstruction using the radial correlation reflectometry data. *Plasma Physics and Controlled Fusion*, 53(4):045012, mar 2011. doi: 10.1088/0741-3335/53/4/045012. URL `https://doi.org/10.1088/0741-3335/53/4/045012`.

[27] Oleg Krutkin, Alexey B Altukhov, Alexey Dmitrievich Gurchenko, Evgeniy Z Gusakov, Michael A Irzak, Lev A Esipov, Anton Sidorov, Laurent Chôné, Timo P Kiviniemi, Susan Leerink, et al. Validation of full-f global gyrokinetic modeling results against the ft-2 tokamak doppler reflectometry data using synthetic diagnostics. *Nuclear Fusion*, 2019.

[28] Peter J Catto. Linearized gyro-kinetics. *Plasma Physics*, 20(7):719, 1978.

[29] EA Frieman and Liu Chen. Nonlinear gyrokinetic equations for low-frequency electromagnetic waves in general plasma equilibria. *The Physics of Fluids*, 25(3): 502–508, 1982.

[30] J C Hillesheim, N A Crocker, W A Peebles, H Meyer, A Meakins, A R Field, D Dunai, M Carr, N Hawkes, MAST Team, et al. Doppler backscattering for spherical tokamaks and measurement of high-k density fluctuation wavenumber spectrum in mast. *Nuclear Fusion*, 55(7):073024, 2015.

[31] M Hirsch, E Holzhauer, J Baldzuhn, B Kurzan, and B Scott. Doppler reflectometry for the investigation of propagating density perturbations. *Plasma Physics and Controlled Fusion*, 43(12):1641, 2001.

[32] F da Silva, S Heuraux, N Lemoine, C Honoré, P Hennequin, M Manso, and R Sabot. Global full-wave simulation of the tore-supra doppler reflectometer. *Review of Scientific Instruments*, 75(10):3816–3818, 2004.

[33] JC Hillesheim, C Holland, L Schmitz, S Kubota, TL Rhodes, and TA Carter. 2d full wave modeling for a synthetic doppler backscattering diagnostic. *Review of Scientific Instruments*, 83(10):10E331, 2012.

[34] TRN Williams, A Köhn, MR O'Brien, and RGL Vann. Propagation in 3d of microwaves through density perturbations. *Plasma Physics and Controlled Fusion*, 56(7):075010, 2014.

[35] Y Peysson, Joan Decker, and Lorenzo Morini. A versatile ray-tracing code for studying rf wave propagation in toroidal magnetized plasmas. *Plasma Physics and Controlled Fusion*, 54(4):045003, 2012.

[36] Nikolai B Marushchenko, Volker Erckmann, Hans J Hartfuss, Mattias Hirsch, Heinrich P Laqua, Henning Maassberg, and Yuri Turkin. Ray tracing simulations of ecr heating and ece diagnostic at w7-x stellarator. *Plasma and Fusion Research*, 2:S1129, 2007.

[37] R Prater, D Farina, Yu Gribov, R W Harvey, AK Ram, Y-R Lin-Liu, E Poli, A P Smirnov, F Volpe, E Westerhof, et al. Benchmarking of codes for electron cyclotron heating and electron cyclotron current drive under iter conditions. *Nuclear Fusion*, 48(3):035006, 2008.

[38] Daniela Farina. A quasi-optical beam-tracing code for electron cyclotron absorption and current drive: Gray. *Fusion Science and Technology*, 52(2):154–160, 2007.

[39] C Honoré, P Hennequin, A Truc, and A Quéméneur. Quasi-optical gaussian beam tracing to evaluate doppler backscattering conditions. *Nuclear fusion*, 46(9):S809, 2006.

[40] Eugene Raymond Tracy, Alain Jean Brizard, AS Richardson, and AN Kaufman. *Ray Tracing and Beyond: Phase Space Methods in Plasma Wave Theory*. Cambridge University Press, 2014.

[41] NA Lopez and IY Dodin. Restoring geometrical optics near caustics using sequenced metaplectic transforms. *New Journal of Physics*, 22(8):083078, 2020.

[42] NA Lopez and IY Dodin. Metaplectic geometrical optics for modeling caustics in uniform and non-uniform media. *Journal of Optics*, 23(2):025601, 2021.

[43] Lee W Casperson. Gaussian light beams in inhomogeneous media. *Applied optics*, 12(10):2434–2441, 1973.

[44] Vlastislav Červenỳ, Mikhail M Popov, and Ivan Pšenčík. Computation of wave fields in inhomogeneous media—gaussian beam approach. *Geophysical Journal International*, 70(1):109–128, 1982.

[45] Yu A Kravtsov and P Berczynski. Gaussian beams in inhomogeneous media: a review. *Studia Geophysica et Geodaetica*, 51(1):1–36, 2007.

[46] A G Peeters. Extension of the ray equations of geometric optics to include diffraction effects. *Physics of Plasmas*, 3(12):4386–4395, 1996.

[47] G V Pereverzev. Paraxial wkb solution of a scalar wave equation. In B B Kadomtsev, editor, *Reviews of Plasma Physics: Volume 19*, pages 1–48. Springer, 1996.

[48] G V Pereverzev. Beam tracing in inhomogeneous anisotropic plasmas. *Physics of Plasmas*, 5(10):3529–3541, 1998.

[49] E Poli, A G Peeters, and G V Pereverzev. Boundary conditions for a gaussian wave beam. *Physics of Plasmas*, 8(10):4325–4330, 2001.

[50] E Poli, G V Pereverzev, and A G Peeters. Paraxial gaussian wave beam propagation in an anisotropic inhomogeneous plasma. *Physics of Plasmas*, 6(1):5–11, 1999.

[51] E Poli, A G Peeters, and G V Pereverzev. Torbeam, a beam tracing code for electron-cyclotron waves in tokamak plasmas. *Computer Physics Communications*, 136(1-2):90–104, 2001.

[52] N Bertelli, AA Balakin, E Westerhof, and MN Buyanova. Eccd calculations in iter by means of the quasi-optical code. *Nuclear Fusion*, 50(11):115008, 2010.

[53] G Ramponi, D Farina, M A Henderson, E Poli, O Sauter, G Saibene, H Zohm, and C Zucca. Physics analysis of the iter ecw system for optimized performance. *Nuclear Fusion*, 48(5):054012, 2008.

[54] David A Thomas. *Phased array imaging of two dimensional Doppler microwave backscattering from spherical tokamak edge plasmas*. PhD thesis, University of York, 2016.

[55] A Stegmeir, G D Conway, E Poli, and E Strumberger. Analysis of the iter low field side reflectometer employing the beam tracing method. *Fusion Engineering and Design*, 86(12):2928–2942, 2011.

[56] J C Hillesheim, E Delabie, H Meyer, C F Maggi, L Meneses, E Poli, JET Contributors, EUROfusion Consortium, et al. Stationary zonal flows during the formation of the edge transport barrier in the jet tokamak. *Physical Review Letters*, 116(6): 065002, 2016.

[57] Omar Maj, Grigory V Pereverzev, and Emanuele Poli. Validation of the paraxial beam-tracing method in critical cases. *Physics of Plasmas*, 16(6):062105, 2009.

[58] Pauli Virtanen, Ralf Gommers, Travis E. Oliphant, Matt Haberland, Tyler Reddy, David Cournapeau, Evgeni Burovski, Pearu Peterson, Warren Weckesser, Jonathan Bright, Stéfan J. van der Walt, Matthew Brett, Joshua Wilson, K. Jarrod Millman, Nikolay Mayorov, Andrew R. J. Nelson, Eric Jones, Robert Kern,

Eric Larson, C J Carey, İlhan Polat, Yu Feng, Eric W. Moore, Jake VanderPlas, Denis Laxalde, Josef Perktold, Robert Cimrman, Ian Henriksen, E. A. Quintero, Charles R. Harris, Anne M. Archibald, Antônio H. Ribeiro, Fabian Pedregosa, Paul van Mulbregt, and SciPy 1.0 Contributors. SciPy 1.0: Fundamental Algorithms for Scientific Computing in Python. *Nature Methods*, 17:261–272, 2020. doi: 10.1038/s41592-019-0686-2.

[59] John R Dormand and Peter J Prince. A family of embedded runge-kutta formulae. *Journal of computational and applied mathematics*, 6(1):19–26, 1980.

[60] H G Booker. Oblique propagation of electromagnetic waves in a slowly-varying non-isotropic medium. *Proceedings of the Royal Society of London. Series A-Mathematical and Physical Sciences*, 155(885):235–257, 1936.

[61] Henry G Booker. Propagation of wave-packets incident obliquely upon a stratified doubly refracting ionosphere. *Philosophical Transactions of the Royal Society of London. Series A, Mathematical and Physical Sciences*, 237(781):411–451, 1938.

[62] R E Slusher and C Ml Surko. Study of density fluctuations in plasmas by small-angle co2 laser scattering. *The Physics of Fluids*, 23(3):472–490, 1980.

[63] Ian H Hutchinson. *Principles of Plasma Diagnostics*. IOP Publishing, 2002.

[64] Dustin Froula, Siegfried H Glenzer, Neville C Luhmann Jr, and John Sheffield. *Plasma scattering of electromagnetic radiation: theory and measurement techniques*. Academic press, 2011.

[65] GA Brooker and Geoffrey Brooker. *Modern classical optics*, volume 8. Oxford University Press, 2003.

[66] Paul F Goldsmith. *Quasioptical systems*. Chapman & Hall New York, 1998.

[67] E Z Gusakov and M A Tyntarev. The two-dimensional theory of reflectometry diagnostics of plasma fluctuations. *Fusion Engineering and Design*, pages 501–505, 1997.

[68] AA Schekochihin, SC Cowley, W Dorland, GW Hammett, Gregory G Howes, GG Plunk, E Quataert, and T Tatsuno. Gyrokinetic turbulence: a nonlinear route to dissipation through phase space. *Plasma Physics and Controlled Fusion*, 50(12):124024, 2008.

[69] AA Schekochihin, SC Cowley, W Dorland, GW Hammett, Gregory G Howes, E Quataert, and T Tatsuno. Astrophysical gyrokinetics: kinetic and fluid turbulent cascades in magnetized weakly collisional plasmas. *The Astrophysical Journal Supplement Series*, 182(1):310, 2009.

[70] M Barnes, FI Parra, and AA Schekochihin. Critically balanced ion temperature gradient turbulence in fusion plasmas. *Physical Review Letters*, 107(11):115003, 2011.

[71] LL Lao, H St John, RD Stambaugh, AG Kellman, and W Pfeiffer. Reconstruction of current profile parameters and plasma shapes in tokamaks. *Nuclear fusion*, 25 (11):1611, 1985.

[72] LC Appel, GTA Huysmans, LL Lao, PJ McCarthy, DG Muir, ER Solano, J Storrs, D Taylor, W Zwingmann, et al. A unified approach to equilibrium reconstruction. In *Proceedings-33rd EPS conference on Controlled Fusion and Plasma Physics, pp. P–2.160*, 2006.

[73] NJ Conway, MFM De Bock, CA Michael, MJ Walsh, PG Carolan, NC Hawkes, Elisabeth Rachlew, JFG McCone, S Shibaev, and G Wearing. The mast motional stark effect diagnostic. *Review of Scientific Instruments*, 81(10):10D738, 2010.

[74] R Scannell, MJ Walsh, MR Dunstan, J Figueiredo, G Naylor, T O'Gorman, S Shibaev, KJ Gibson, and H Wilson. A 130 point nd: Yag thomson scattering diagnostic on mast. *Review of Scientific Instruments*, 81(10):10D520, 2010.

[75] Peter Welch. The use of fast fourier transform for the estimation of power spectra: a method based on time averaging over short, modified periodograms. *IEEE Transactions on audio and electroacoustics*, 15(2):70–73, 1967.

[76] Fredric J Harris. On the use of windows for harmonic analysis with the discrete fourier transform. *Proceedings of the IEEE*, 66(1):51–83, 1978.

[77] Tim Happel. *Doppler Reflectometry in the TJ-II Stellarator: Design of an Optimized Doppler Reflectometer and its Application to Turbulence and Radial Electric Field Studies*. PhD thesis, University Carlos III of Madrid, 2010.